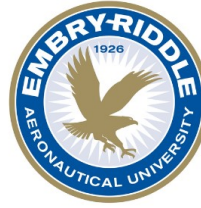




**Politecnico  
di Torino**



**EMBRY-RIDDLE**  
Aeronautical University.  
PRESCOTT, ARIZONA

# Politecnico di Torino

Department of Mechanical and  
Aerospace Engineering (DIMEAS)

Master's Degree in Aerospace Engineering

*Interplanetary Orbit Insertion Maneuvers into  
Saturn-Titan Three-Body Orbits Using  
Dynamical Systems Theory*

Supervisors:

**Prof. Lorenzo Casalino**  
**Dr. Davide Conte**

Candidate:

**Giuseppe Papalia**  
**290495**

Anno accademico 2022/2023



*A nonna Pina,  
con amore*

## Abstract

Space exploration within the Saturnian system has garnered immense scientific interest, particularly focused on Titan, Saturn's largest moon. This thesis presents a comprehensive methodology that harnesses the synergy between Dynamical Systems Theory (DST) and Particle Swarm Optimization (PSO) to optimize spacecraft trajectories for interplanetary orbit insertion into Saturn-Titan three-body orbits.

This study begins with an in-depth exploration of Titan, underscoring its pivotal role across past, present, and future space missions. This encompasses a detailed understanding of its orbital and physical characteristics, clarifying the reasons behind its significance as a subject of extensive exploration within our solar system.

The investigation navigates the complexities of the Circular Restricted Three-Body Problem (CR3BP), delving into Lagrange points and illustrating the different families of orbits shaped by the gravitational interplay of three celestial bodies. A pivotal trade-off analysis ensues to identify the optimal CR3BP orbits for comprehensive observations of Titan. Factors such as Titan's surface visibility, orbital stability, and Saturn's accessibility guide this analysis, ultimately spotlighting the stability and the comprehensive coverage of Distant Retrograde Orbits (DROs). Despite their advantages, limitations in accessing polar regions are noted, emphasizing the need to balance scientific exploration with orbital stability considerations.

The integration of Dynamical System Theory into trajectory planning establishes a robust scientific foundation. Concepts like differential corrections, Poincaré sections and invariant manifolds pave the way for the computation of viable trajectories towards CR3BP orbits, ensuring a meticulous approach to spacecraft trajectory planning.

A crucial innovation arises through the application of the Particle Swarm Optimization (PSO) algorithm. Inspired by natural behaviors like bird flocking, PSO has found applications in various fields, including trajectory design. The algorithm begins with a population of potential solutions, represented as particles within a multidimensional space. Each particle's position represents a possible solution, and their movement in the solution space is influenced by two critical components: their own best-known position (personal best) and the swarm's best-known position (global best).

By leveraging DST and PSO synergistically, the thesis optimizes the trajectory enabling the derivation of an optimal trajectory that minimizes the required  $\Delta V$  for insertion.

This integrated approach yields remarkable results. The optimized trajectory achieves a  $\Delta V = 2.6813$  km/s, marking a substantial 70.9% decrease compared to direct insertion onto Titan. This reduction demonstrates the efficiency of this novel approach, leading spacecraft trajectories across invariant manifolds and showcasing the efficacy of advanced computational techniques in interplanetary mission planning.

This achievement stands as a testament to the efficacy and significance of employing

advanced computational techniques in optimizing interplanetary trajectories within the Saturn-Titan system.

Essentially, this thesis presents an accurate interplanetary mission planning framework that optimizes spacecraft trajectories in the complex Saturn-Titan system. By combining optimization methods with Dynamical Systems Theory, this research aims to paving the way for accurate and efficient future explorations.

## Acknowledgements

As I contemplate the conclusion of this academic journey, I'm profoundly thankful for the unwavering support, guidance, and encouragement that have been crucial in navigating the completion of my academic journey.

Firstly, I would like to express my heartfelt gratitude to Dr. Davide Conte, my mentor at Embry-Riddle Aeronautical University. The four months spent under his guidance in Arizona were transformative, fostering not only academic growth but also significant personal development. His mentorship instilled resilience and confidence in facing challenges. His invaluable support in recent months has been instrumental in overcoming difficult obstacles. Dr. Conte embodies an outstanding mentor—one whom aspiring scholars deeply respect and admire. Learning from him has been a point of pride.

I also want to extend my gratitude to Professor Lorenzo Casalino, my internal supervisor at Politecnico di Torino. His mentorship, insightful feedback, and unwavering guidance have shaped the direction of my research and academic pursuits.

I am thankful to Politecnico di Torino, my academic home throughout my university journey. Reflecting on my path, I'm immensely pleased with my choice. In Torino, I discovered my second home, and within PoliTO, I found a stimulating environment fostering my growth.

Additionally, I hold deep gratitude towards Embry-Riddle Aeronautical University for nurturing an environment that fueled my growth. Their warm reception facilitated not only my learning but also unexpected personal and intellectual flourishing.

My deepest appreciation goes to my family, my parents, my sister, and my brother for their immense support, both morally and financially, throughout my journey. Your unwavering belief in me and the sacrifices you've made for me resonate deeply. I am delighted to say that finally, these sacrifices have been rewarded. Your continuous encouragement has been the cornerstone of my achievements, and I am indebted to you for believing in me every step of the way. I am immensely fortunate to have a family that champions my aspirations and stands by me, enabling me to reach this milestone.

Gratitude extends to all my friends. I'm genuinely thankful for brightening my days, bringing joy into my life, and lifting my spirit when I was down. Your companionship has been invaluable and essential. I'm certain that the friendships forged during this time will endure. I wish you all the best! Your friendship has been a gift, and I am grateful for the laughter, the shared moments, and the support we've given each other. Here's to the hope that our paths continue to cross and that our bonds remain strong in the years to come.

I'm immensely grateful for the friends I've made at Politecnico during these past

years. Through PoliTOrbital, I met determined teammates with whom I've collaborated closely, enriching our efforts. The synergy and shared commitment have been truly rewarding. Through SpaceLighthouse (or Night Vision, as you prefer), I connected with driven individuals, fostering essential growth experiences. The friendships forged within these circles have not only amplified my academic pursuits but have also significantly contributed to my personal development. I deeply appreciate the dedication, collaboration, and camaraderie that defined our collective endeavors. These connections are priceless, and I eagerly anticipate how our paths will continue to intertwine and inspire each other in the future.

To everyone, I extend heartfelt appreciation for your invaluable contributions, unwavering support, and belief in my endeavors. Your collective influence profoundly impacted my academic and personal growth, for which I'm immensely grateful.

While composing these acknowledgments, I retraced every step of my university journey. Amidst it all, I express profound thanks to the past version of myself. You navigated challenges, weathered uncertainty, and confronted daunting experiences. Yet, here I stand today as a testament to your resilience and determination.

Thanks to all who've been there and are here now. Your presence means the world to me. Love you.

## Acronyms

<b>2BP</b>	Two-Body Problem
<b>ASI</b>	Agenzia Spaziale Italiana
<b>AVIATR</b>	Aerial Vehicle for In-situ and Airborne Titan Reconnaissance
<b>CM</b>	Center of Mass
<b>CR3BP</b>	Circular Restricted Three-Body Problem
<b>DE</b>	Differential Evolution
<b>DSM</b>	Deep Space Maneuver
<b>DRO</b>	Distant Retrograde Orbit
<b>DST</b>	Dynamical Systems Theory
<b>EGA</b>	Earth Gravity Assist
<b>ESA</b>	European Space Agency
<b>EOMs</b>	Equations Of Motion
<b>GA</b>	Genetic Algorithms
<b>ICs</b>	Initial Conditions
<b>IRF</b>	Inertial Reference Frame
<b>JPL</b>	Jet Propulsion Laboratory
<b>JWST</b>	James Webb Space Telescope
<b>LU</b>	Length Unit
<b>MU</b>	Mass Unit
<b>NASA</b>	National Aeronautics and Space Administration
<b>ND</b>	Non-Dimensional
<b>NRHO</b>	Near-Rectilinear Halo Orbit
<b>ODE</b>	Ordinary Differential Equation
<b>PSO</b>	Particle Swarm Optimization
<b>RRF</b>	Rotational Reference Frame
<b>SOI</b>	Sphere Of Influence
<b>STM</b>	State-Transition Matrix
<b>TALISE</b>	Titan Lake In-situ Sampling Propelled Explorer
<b>TSSM</b>	Titan Saturn System Mission
<b>TiME</b>	Titan Mare Explorer
<b>TU</b>	Time Unit
<b>TOF</b>	Time Of Flight



# Contents

<b>List of Figures</b>	<b>VII</b>
<b>List of Tables</b>	<b>IX</b>
<b>List of Algorithms</b>	<b>IX</b>
<b>1 Titan</b>	<b>1</b>
1.1 Physical and Orbital Characteristics . . . . .	1
1.2 Previous Missions . . . . .	3
1.3 Future and Proposed Missions . . . . .	5
1.4 Summary . . . . .	7
<b>2 Circular Restricted Three-Body Problem (CR3BP)</b>	<b>9</b>
2.1 Mathematical Formulation of the CR3BP . . . . .	9
2.2 Lagrange Points . . . . .	12
2.3 Jacobi Integral . . . . .	16
2.4 Periodic Orbits in the CR3BP and Applications in Space Missions . . . . .	20
<b>3 Assessing CR3BP Orbits: A Trade-off Analysis</b>	<b>26</b>
3.1 Saturn’s Accessibility . . . . .	26
3.2 Titan’s Surface Visibility . . . . .	29
3.3 Stability . . . . .	32
3.4 Orbit Selection . . . . .	33
<b>4 Dynamical Systems Theory</b>	<b>35</b>
4.1 State-Transition Matrix . . . . .	35
4.2 Differential Correction . . . . .	38
4.3 Poincarè Section . . . . .	40
4.4 Invariant Manifolds . . . . .	41
4.5 Employing Invariant Manifolds for Lyapunov Orbits . . . . .	45
<b>5 Particle Swarm Optimization</b>	<b>49</b>
5.1 Description of the Method . . . . .	49
5.2 Application of PSO Algorithm for DRO’s Initial Conditions . . . . .	54
<b>6 Trajectory Optimization</b>	<b>57</b>
6.1 Interplanetary Arrival . . . . .	57
6.2 Direct Arrival to Titan . . . . .	59
6.3 Direct Arrival to the Lyapunov Orbit . . . . .	61
6.4 Hyperbolic Arrival in Invariant Manifolds . . . . .	63
6.5 Trajectory Overview and Final Results . . . . .	70
<b>7 Conclusions &amp; Future Work</b>	<b>74</b>

## List of Figures

1	Titan from Cassini spacecraft (Sept. 13, 2017) . . . . .	1
2	Titan’s first geological map (Nov. 18, 2019) . . . . .	3
3	Lakes on north polar region on Titan (Jul. 24, 2006) . . . . .	4
4	First color view of Titan’s surface . . . . .	5
5	Titan Mare Explorer (TiME) lake lander (artist’s concept) . . . . .	6
6	Geometry of the CR3BP . . . . .	9
7	Geometry of the CR3BP ( $\hat{i} - \hat{j}$ plane) . . . . .	11
8	Lagrange points . . . . .	15
9	Lagrange points. Focus on Titan . . . . .	16
10	Zero-velocity curves for the Saturn-Titan system for $J=J(L_1)=-1.50791$ . .	17
11	Zero-velocity curves for the Saturn-Titan system for $J=J(L_1)=-1.50791$ . Zoomed-in view . . . . .	18
12	Zero-velocity curves for the Saturn-Titan system for $J=J(L_2)=-1.50777$ . .	18
13	Zero-velocity curves for the Saturn-Titan system for $J=J(L_2)=-1.50777$ . Zoomed-in view . . . . .	19
14	Zero-velocity curves for the Saturn-Titan system for $J=J(L_3)=-1.50012$ . .	19
15	A planar Lyapunov orbit around $L_1$ with $J=-1.50417817$ . . . . .	20
16	An axial orbit around the $L_2$ point ( $J=-1.50181178$ ) and a vertical orbit around $L_1$ point ( $J=-1.48570466$ ) . . . . .	21
17	A butterfly (northern) orbit ( $J=-1.50456526$ ) and a dragonfly (southern) orbit ( $J=-1.50062838$ ) . . . . .	22
18	A halo orbit around $L_1$ ( $J=-1.50650741$ ), a halo orbit around $L_2$ ( $J=-$ $1.50631369$ ) and a northern near-rectilinear halo orbit ( $J=-1.50175791$ ) . .	23
19	A DRO ( $\approx 5$ days) with $J= -1.50054681$ and a DRO ( $\approx 9$ days) with $J=$ $-1.49801423$ . . . . .	24
20	Halo orbit around $L_1$ in the rotational reference frame . . . . .	26
21	Halo orbit around $L_1$ in the inertial reference frame . . . . .	27
22	DRO in the rotational reference frame . . . . .	28
23	DRO in the inertial reference frame . . . . .	28
24	Field of view from a specific position on a Butterfly orbit . . . . .	29
25	Titan’s surface visibility for a halo orbit around $L_2$ . . . . .	30
26	Titan’s surface visibility for a halo orbit around $L_2$ (zoom on Titan’s surface)	31
27	Dragonfly landing site . . . . .	33
28	Poincarè Map . . . . .	40
29	Stable and Unstable Manifolds of a halo orbit in the Saturn-Titan system ( $xy$ plane) . . . . .	41
30	Stable and Unstable Manifolds of a halo orbit in the Saturn-Titan system	42
31	Stable and Unstable Manifolds of a halo orbit in the Saturn-Titan system. Focus on Titan . . . . .	42
32	Poincarè Section on Saturn . . . . .	44
33	Poincarè Section on Titan . . . . .	44

34	Intersection between the Lyapunov orbit and the DRO . . . . .	45
35	Stable and Unstable Manifolds of the Lyapunov orbit ( $xy$ plane) . . . . .	46
36	Stable and Unstable Manifolds of the Lyapunov orbit . . . . .	47
37	Stable and Unstable Manifolds of the Lyapunov orbit. Focus on Titan . .	47
38	Structure of the PSO algorithm . . . . .	51
39	Particles variations and convergence . . . . .	55
40	DRO obtained using the PSO algorithm . . . . .	56
41	Hyperbolic Arrival . . . . .	58
42	Hyperbolic Arrival. Focus on Saturn-Titan system . . . . .	58
43	Direct Hyperbolic Arrival to Titan . . . . .	59
44	Direct Hyperbolic Arrival to Titan: Titan's SOI . . . . .	60
45	Direct Hyperbolic Arrival to Lyapunov Orbit . . . . .	62
46	Invariant Manifolds in the Saturn-Titan system on October 10th, 2043 . .	64
47	Variables of the PSO Algorithm . . . . .	66
48	PSO algorithm results . . . . .	67
49	Spacecraft's final trajectory (PSO results) . . . . .	68
50	Spacecraft's final trajectory (PSO results). Zoom-in on the first maneuver	69
51	Spacecraft's final trajectory (PSO results). Zoom-in on the second maneuver	69
52	Final trajectory overview . . . . .	70
53	Final trajectory overview. First maneuver ( $\Delta V_1$ ) . . . . .	71
54	Final trajectory overview. Second maneuver ( $\Delta V_2$ ) . . . . .	72
55	Final trajectory overview. Third maneuver ( $\Delta V_3$ ) . . . . .	73
56	Optimized trajectory to Titan . . . . .	75

## List of Tables

1	Titan's main features . . . . .	2
2	Titan's orbital characteristics . . . . .	2
3	Lagrange points coordinates of Saturn-Titan system . . . . .	15
4	Examples of CR3BP candidate orbits characteristics between Saturn and Titan . . . . .	25
5	CR3BP candidate orbits: Saturn visibility . . . . .	29
6	CR3BP candidate orbits: Titan visibility . . . . .	31
7	CR3BP candidate orbits: Stability index . . . . .	32

## List of Algorithms

1	Differential Correction for orbits in the $xz$ -plane . . . . .	39
2	Computation of Invariant Manifolds . . . . .	43
3	Particle Swarm Optimization (PSO) . . . . .	53



# 1 Titan

## 1.1 Physical and Orbital Characteristics

Titan is the biggest moon of Saturn and the second largest moon in the entire Solar System after Ganymede, the moon of Jupiter. Discovered in 1655 by the astronomer Christiaan Huygens, it was originally named *Saturni Luna* (lit. *Saturn's Moon*) and later it was renamed *Titan* by John Herschel, following the convention of naming Saturnian moons after mythological giants, in this case the Titans, primordial forces of the cosmos in Greek mythology.

Titan's dense atmosphere and the evidence of liquids on its surface make it the only known celestial body (aside from Earth) with such characteristics: the atmosphere is primarily composed of nitrogen, with trace of hydrocarbons such as methane ( $\text{CH}_4$ ) and ethane ( $\text{C}_2\text{H}_6$ ). Despite their lower concentrations, methane and ethane play crucial roles in the atmospheric processes of Titan. They can condense and form clouds, much like water vapor does on Earth. The climate is characterized by wind and rain, which create features on the surface resembling those found on Earth. Table 1 provides an overview of the main characteristics of Titan, shown in Figure 1.

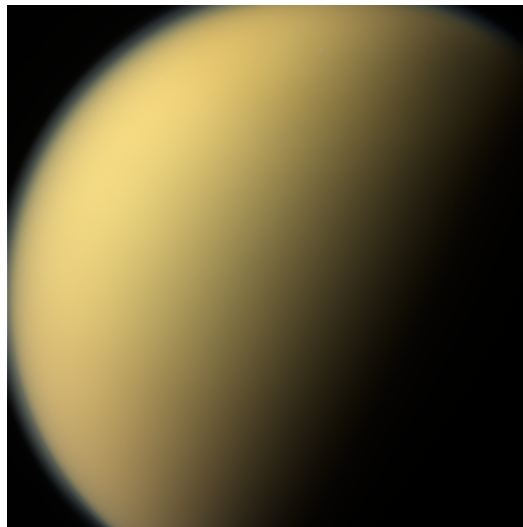


Figure 1: Titan from Cassini spacecraft (Sept. 13, 2017) [1]

Table 1: Titan’s main features [2]

Mean radius	$2574.73 \pm 0.09 \text{ km}$
Surface area	$8.3 \cdot 10^7 \text{ km}^2$
Volume	$7.16 \cdot 10^{10} \text{ km}^3$
Mass	$1.3452 \pm 0.0002 \cdot 10^{23} \text{ kg}$
Mean density	$1.8798 \pm 0.0044 \text{ g/cm}^3$
Surface gravity	$1.352 \text{ m/s}^2$
Albedo	0.22

Titan orbits around Saturn in 15 days and 22 hours and, as many other moons including Earth’s Moon, it is tidally locked in synchronous rotation with its planet. This means that it permanently shows the same face towards Saturn. Table 2 lists the main orbital characteristics of Titan.

Table 2: Titan’s orbital characteristics [2]

Periapsis	1186680 km
Apoapsis	1257060 km
Semi-major axis	1221870 km
Eccentricity	0.0288
Orbital period (sidereal)	15.945 d
Average orbital speed	5.57 km/s
Inclination	$0.34854^\circ$ (wrt Saturn’s equator)

Titan is the only moon that has an atmosphere: it is composed of 94.2% nitrogen, 5.65% methane and 0.099% hydrogen. The orange hue observed from space on Titan’s surface is attributed to the presence of other complex compounds in small amounts, which are responsible for its unique and characteristic color [3]. It is noteworthy that the composition and abundance of these compounds remain a subject of interest and ongoing research among planetary scientists.

The low surface gravity of Titan (about 0.138g) allows its atmosphere to extend up to 975 km from the surface: the Cassini spacecraft experienced aerodynamic drag due to the atmosphere of Titan and had to make several adjustments to maintain a stable orbit at this altitude [4].

Titan’s atmospheric structure is similar to Earth’s, as determined through data from Voyager, the Huygens lander, and radiative-convective models. Despite receiving only 1% of the sunlight that Earth receives, the presence of methane generates a greenhouse effect that increases surface temperatures. However, the presence of haze reflects sunlight and acts as an anti-greenhouse effect. The greenhouse effect raises the surface temperature by 21 K, while the anti-greenhouse effect lowers it by 9 K. The surface temperature (94 K) is ultimately 12 K warmer than the effective temperature (82 K). [5].

Southern summers are shorter but hotter than northern summers because Titan is 12% closer to the Sun during the southern hemisphere’s summer due to Saturn’s eccentric orbit. The hemispheres’ topographies differ as a result of this asymmetry.

The Cassini mission confirmed that Titan has hydrocarbon lakes, and the surface of Titan is distinguished by the presence of impact craters that have been filled up by methane rain. However Titan is substantially drier than Earth because lakes only cover a small portion of its surface, according to radar observations made by the Cassini mission [6]. Many long-lasting hydrocarbon lakes have also been found in the equatorial desert areas, including one close to the Huygens landing site in the Shangri-La region [7]. Most of the lakes are located around the poles, where the relative lack of sunlight inhibits evaporation.

In Figure 2, the first global geologic map of Titan is presented, which was created using radar, visible and infrared images obtained from NASA’s Cassini mission.

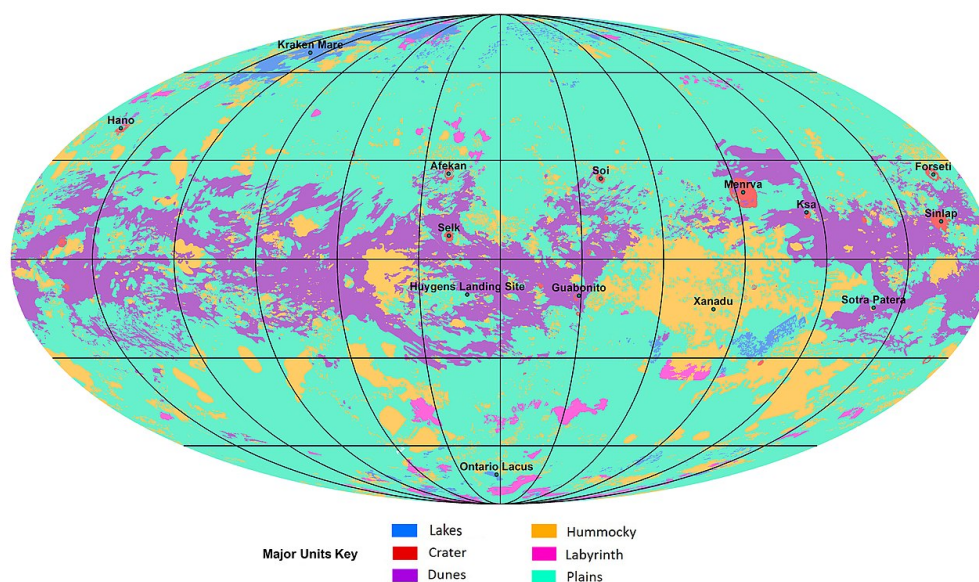


Figure 2: Titan’s first geological map (Nov. 18, 2019) [8]

## 1.2 Previous Missions

The first man-made object to visit Titan was *Pioneer 11*, launched in 1973 and passed close to Titan in the fall of 1979: the spacecraft took the first close-up images of the moon, revealing an opaque and hazy surface [9] that fueled scientists’ curiosity for decades, until the NASA/ESA Cassini-Huygens mission provided a more detailed overview of the surface of Titan.

In 1980, it was the *Voyager 1* spacecraft that provided new data and images of Saturn’s largest moon: the mission was in fact designed with the goal of conducting a flyby of Titan, which occurred on November 12, 1980, at a distance of about 4000 km.

This maneuver allowed the study of the atmosphere: for the first time, data suggested that there could be liquid on the surface [10].

The next year *Voyager 2* approached Saturn for a flyby and took photos of Titan: however, given the success of the previous mission, *Voyager 2* continued on its trajectory towards Uranus and Neptune[11]. The data and images provided by the *Voyager 1* and *2* missions confirmed some theories but opened the field to many new questions, especially following the confirmation of the presence of a thick atmosphere and liquid on the surface.

The concept for a mission to investigate Saturn and Titan emerged in 1982. Together with European Space Agency (ESA) and the Italian Space Agency (ASI), NASA launched the *Cassini-Huygens* mission in 1997, and it arrived at Saturn in 2004. Among its goals were analyzing Titan's surface on a regional level and researching the clouds and hazes' temporal variations.

In 2004, the *Cassini* spacecraft took the highest-resolution images ever taken of the surface of Titan. In the following years, *Cassini* performed a series of flybys of the moon (the closest of which was at 880 km in 2010 [4]), which allowed the discovery of abundant liquid on the surface in the north polar regions [12] . The discovery is shown in Figure 3.

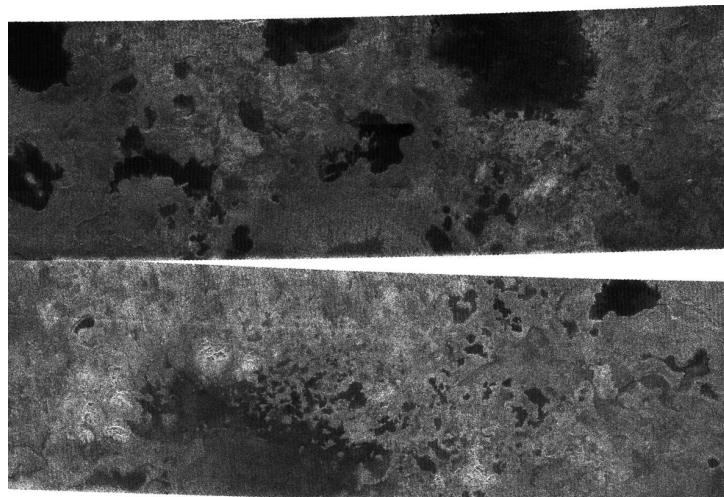


Figure 3: Lakes on north polar region on Titan (Jul. 24, 2006) [13]

The *Cassini-Huygens* mission carried ESA's *Huygens* probe. On January 14, 2005, the *Huygens* probe successfully landed on the surface of Titan, becoming the first spacecraft to land on a moon in the outer Solar System. The *Huygens* mission was designed to be able to land in various possible scenarios, such as plains, mountains, or lakes, as the topography of Titan was not well known. The probe was designed to withstand impact or a potential splashdown on a liquid surface and transmit data for at least a couple of minutes. During its descent, the probe collected data on the moon's atmosphere, temperature, and composition. It also captured the first images of Titan's surface, in Figure 4, revealing a landscape of hills, valleys, and channels that appeared to have been sculpted by liquid.

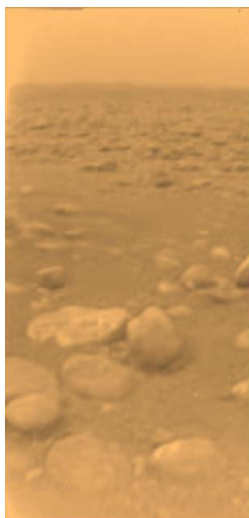


Figure 4: First color view of Titan’s surface (Jan. 15, 2005) [14]

This picture suggests that while there is evidence of liquids acting on the surface recently, hydrocarbon lakes and/or seas might not currently exist at the Huygens landing site. However, further data from the Cassini mission confirmed the existence of permanent liquid hydrocarbon lakes in the polar regions of Titan [7].

Huygens continued to broadcast from Titan’s surface for a further 72 minutes following the touchdown, at which point Cassini vanished over the horizon. Scientists are still mining the unique resource of in situ measurements that the stream of data returned from the surface offered [15].

### 1.3 Future and Proposed Missions

Titan is a top priority target for astrobiology and origin of life research because of its complex and diversified carbon-rich chemistry. The surface is dominated by water ice and has an ocean of liquid water within [16]. These qualities have facilitated the development of several conceptual missions incorporating drones, rovers, and submarines.

The new *Dragonfly* mission to Saturn’s major moon was suggested by NASA in April 2017. Based on the understanding of Titan’s atmosphere, the mission goal is to send a robotic rotorcraft to Titan’s surface to investigate primordial chemistry and extraterrestrial habitability. The rotorcraft will land in the dunes of the Selk impact structure and from there it will proceed to a series of flights to collect samples from various areas with diverse geography. The choice of this landing site is due to the presence of tholin organic compounds and evidence of past liquid water [17].

The rotorcraft’s design is unique, as it will be able to fly like a drone, making it easier to cover long distances and access difficult-to-reach locations. The *Dragonfly* mission is also expected to provide insight into the formation and evolution of Titan and help scientists understand the potential for habitable environments on other worlds. *Dragonfly*

is scheduled to launch in June 2027 and travel to Titan over the course of seven years, arriving in 2034 [17].

In 2008, the *Titan Saturn System Mission (TSSM)* was proposed as a joint NASA/ESA mission aimed at developing an orbiter, a lander, and a research balloon to study the Saturnian system, with a focus on the moon Titan.

The TSSM mission aims to conduct detailed investigations of Titan and explore its composition, history, and habitability. The orbiter would have provided high-resolution mapping of Titan's surface, while the lander would have analyzed the moon's geology and chemistry. The research balloon would have floated through Titan's dense atmosphere and analyzed its composition and circulation patterns [18]. However, due to budget constraints and the prioritization of other missions, the TSSM mission was postponed indefinitely.

The *Titan Mare Explorer (TiME)* mission (a concept is shown in Figure 5) was proposed in 2011 by Johns Hopkins University Applied Physics Laboratory as one of the three finalists to receive funding for developing a detailed concept study.

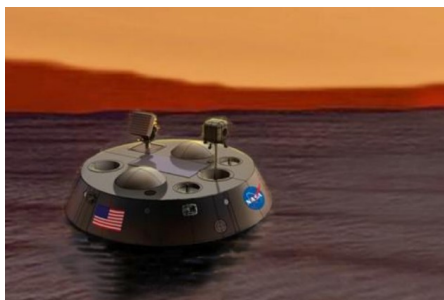


Figure 5: Titan Mare Explorer (TiME) lake lander (artist's concept) [19]

The TiME mission aimed to develop a lake lander capable of landing in the Ligeia Mare and floating in those waters for at least three months. The mission's scientific goals included the first active measurement of the water cycle on a celestial body other than Earth and the determination of the composition of the major constituents of the sea. The lander would have been equipped with instruments to measure the composition and physical properties of the lake and the atmosphere, as well as cameras for imaging the surrounding landscape [19]. Unfortunately, TiME was not selected for further development, as the mission InSight on Mars was chosen instead.

Among other proposed missions are the *Aerial Vehicle for In-situ and Airborne Titan Reconnaissance (AVIATR)*, a concept for an aircraft capable of acquiring data on Titan by flying in its atmosphere, and the *Titan Lake In-situ Sampling Propelled Explorer (TALISE)*, a lake lander capable of navigating thanks to a propulsion system.

AVIATR is a proposed mission that would use a quadcopter to explore Titan's atmosphere and surface, collecting data and samples for analysis [20]. TALISE, on the other hand, is a concept for a lake lander that would be able to navigate and explore Titan's liquid methane and ethane lakes [21]. However, neither mission has been selected for development as of yet.

## 1.4 Summary

After discussing Titan, Saturn's largest moon and the second-largest in our solar system, with its physical and orbital characteristics, the next chapters focus on the theoretical background and application of Dynamical Systems Theory and Particle Swarm Optimization. The aim is to optimize the trajectory for insertion into a Circular Restricted Three-Body Problem (CR3BP) orbit, which will be defined through a trade-off process.

Chapter 2 delves into the foundational theoretical framework crucial for the thesis development. It introduces the CR3BP and the methodologies used for analyzing this complex system. In this chapter, the equations of motion are derived in a rotating reference frame, emphasizing the assessment of stability at Lagrange points and the pivotal role of the Jacobi integral in identifying zero-velocity surfaces for spacecraft. This thorough analysis aims to solve the equations of motion, providing a deeper comprehension of the orbital families involving these three celestial bodies. Despite their stability intricacies, these periodic orbits hold substantial significance for extended space missions, carrying critical implications for missions targeting exploration of Titan and Saturn within the CR3BP framework.

Chapter 3 focuses on conducting a comparative analysis among different families of CR3BP orbits. It evaluates their applicability for investigating Titan, considering factors such as orbit stability, accessibility of Saturn, and coverage of Titan's surface. Among these orbits, the Distant Retrograde Orbits (DROs) emerge as the favored option due to their stability and extensive coverage of Titan's surface. However, they do come with limitations regarding accessibility to polar regions. This strategic selection aims to strike a balance between scientific exploration and orbit stability, complementing localized studies such as Dragonfly while enabling a more comprehensive, global-scale investigation.

Chapter 4 delves into the application of Dynamical Systems Theory (DST) within astrodynamics and trajectory design. It elaborates on various fundamental concepts, including the State-Transition Matrix (STM), Differential Correction, Poincaré Sections, and Invariant Manifolds. These concepts are presented in detail to underscore their significance in comprehending orbital dynamics and planning trajectories. Importantly, these principles play a crucial role in optimizing spacecraft trajectories for precise navigation within celestial systems. The chapter highlights how DST serves as a foundational framework for understanding and manipulating the complexities of orbital dynamics, facilitating the design and refinement of spacecraft trajectories for space missions.

Chapter 5 explores the Particle Swarm Optimization (PSO) as a problem-solving approach, specifically focusing on its application in designing interplanetary trajectories. Within the context of the CR3BP model, the PSO served as a valuable tool for computing initial conditions essential for DROs within the Saturn-Titan systems. The chapter elucidates the structural framework of the PSO algorithm, detailing its efficacy in navigating and exploring solution spaces required for optimizing trajectories.

Chapter 6 focuses on the actual optimization of trajectories. Initially, it introduces scenarios crucial for defining comparison terms and benchmarks. Subsequently, the PSO algorithm is applied to optimize the trajectory and insertion, starting from hyperbolic arrival to a trajectory defined by invariant manifolds, aiming to reduce  $\Delta V$ . This chapter delineates the application of PSO to minimize  $\Delta V$  requirements for specific maneuvers during the approach to Titan. By assessing diverse combinations of maneuvers throughout the trajectory, PSO identifies the most efficient solutions that minimize the overall propulsion demands for the mission. Ultimately, the method described in this thesis facilitates a reduction in  $\Delta V$  of over 70%, leading to significant fuel savings.

The thesis culminates in presenting the achieved optimal trajectory obtained through the application of PSO and DST. This trajectory represents the result of rigorous optimization efforts aiming to enhance spacecraft insertion into the Saturn-Titan system. Furthermore, the thesis proposes potential avenues for future developments. These include exploring advanced optimization techniques beyond PSO, incorporating real-time adjustments based on evolving celestial conditions, and refining the application of DST principles for more intricate trajectory designs. Additionally, suggestions for extending this research to other celestial bodies or complex multi-body systems within the realm of astrodynamics are put forward as potential areas for future study and advancement.

## 2 Circular Restricted Three-Body Problem (CR3BP)

### 2.1 Mathematical Formulation of the CR3BP

The Circular Restricted Three-Body Problem (CR3BP) is a mathematical model used to study the motion of three celestial bodies, where two are much more massive than the third. This concept is based on three hypotheses:

1. the CR3BP considers three bodies  $m_1$ ,  $m_2$  and  $m_3$  such that the third mass is much smaller than the two main ones, termed primaries:

$$m_1 > m_2 \gg m_3 \quad (1)$$

2. the third body  $m_3$  has no gravitational influence on the motion of  $m_1$  and  $m_2$ ;
3. the two primaries  $m_1$  and  $m_2$  orbit in circular orbits relative to their center of mass (CM);

Figure 6 shows the three masses in an inertial reference frame IRF  $(\hat{I}, \hat{J}, \hat{K})$  centered at the barycenter of the masses  $m_1$  and  $m_2$ .

One can also consider a rotational reference frame RFF  $(\hat{i}, \hat{j}, \hat{k})$  with the versor  $\hat{i}$  connecting the barycenters and pointing toward the largest mass, the versor  $\hat{j}$  perpendicular to the plane of motion and the versor  $\hat{k}$  accordingly (right hand rule).

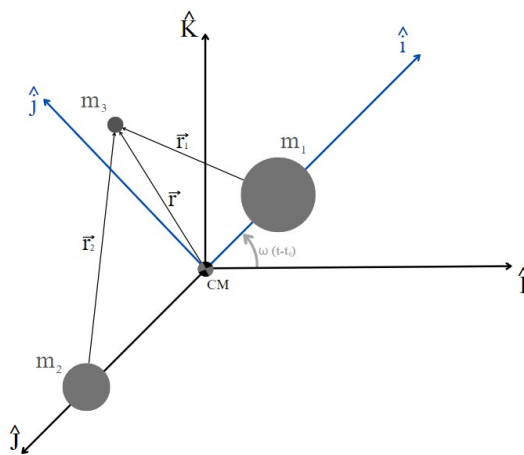


Figure 6: Geometry of the CR3BP

Here, we derive the equations of motion in the rotating frame, which rotates with  $\vec{\omega} = \omega \hat{k}$ .

The position of  $m_3$  (with respect to barycenter) is

$$\vec{r} = x\hat{i} + y\hat{j} + z\hat{k} \quad (2)$$

while the velocity and the acceleration are:

$$\vec{v} = \frac{d\vec{r}}{dt} + \vec{\omega} \times \vec{r} \quad (3)$$

$$\vec{a} = \frac{d^2\vec{r}}{dt^2} + 2\vec{\omega} \times \frac{d\vec{r}}{dt} + \frac{d\vec{\omega}}{dt} \times \vec{r} + \vec{\omega} \times (\vec{\omega} \times \vec{r}) \quad (4)$$

Knowing that

$$2\vec{\omega} \times \frac{d\vec{r}}{dt} = 2\omega \frac{dx}{dt} \hat{j} - 2\omega \frac{dy}{dt} \hat{i} \quad (5)$$

is the Coriolis acceleration (with opposite sign),

$$\frac{d\vec{\omega}}{dt} \times \vec{r} = x \frac{d\omega}{dt} \hat{j} - y \frac{d\omega}{dt} \hat{i} \quad (6)$$

is the Euler acceleration (with opposite sign) and

$$\vec{\omega} \times (\vec{\omega} \times \vec{r}) = -\omega^2(x\hat{i} + y\hat{j}) \quad (7)$$

is the centripetal acceleration, we get:

$$\vec{a} = \frac{d^2\vec{r}}{dt^2} = \left( \frac{d^2x}{dt^2} - 2\frac{dy}{dt} - y\frac{d\omega}{dt} - \omega^2x \right) \hat{i} + \left( \frac{d^2y}{dt^2} + 2\frac{dx}{dt} - x\frac{d\omega}{dt} - \omega^2y \right) \hat{j} + \left( \frac{d^2\omega}{dt^2} \right) \hat{k} \quad (8)$$

The problem can be non-dimensionalized by defining the length unit LU, the mass unit MU and the time unit TU.

- 1 LU :=  $a_1 + a_2$
- 1 MU :=  $m_1 + m_2$
- 1 TU :=  $\frac{T}{2\pi} \Rightarrow \omega = 1$

where  $a_1$  and  $a_2$  represent the distance, respectively, from Saturn and Titan to the system's barycenter, while T is the orbital period of Titan relative to Saturn.

We can also define the *mass ratio*  $\mu$  as:

$$\mu = \frac{m_2}{m_1 + m_2} \quad (9)$$

Having  $m_1 > m_2$  (from assumption 1) we get that  $\mu \in (0, 0.5]$ , even though within the Solar System,  $\mu = 0.5$  is never reached.

Having  $\mu = 0$  means that  $m_2 = 0$ : there are only two bodies involved, indicating a two-body problem (2BP); viceversa having  $\mu = 0.5$  means that  $m_2 = m_1$ : a system in which the two main bodies have equal mass, which is similar to many binary systems.

Using the definition of barycenter (refer to Figure 7):

$$m_1 a_1 = m_2 a_2 \Rightarrow \frac{a_1}{a_2} = \frac{\mu}{1 - \mu} \quad (10)$$

and knowing that:

$$a_1 + a_2 = 1 \quad (11)$$

results in:

$$a_1 = \mu \quad a_2 = 1 - \mu \quad (12)$$

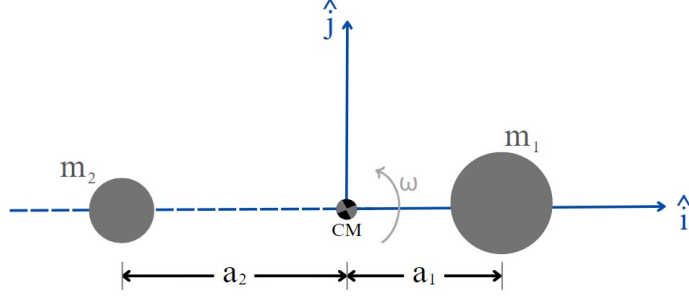


Figure 7: Geometry of the CR3BP ( $\hat{i} - \hat{j}$  plane)

We can compute the position of  $m_3$  with respect to  $m_1$  and  $m_2$ ,  $\vec{r}_1$  and  $\vec{r}_2$  respectively, as:

$$\vec{r}_1 = \vec{r} - \mu \hat{i} = (x - \mu) \hat{i} + y \hat{j} + z \hat{k} \quad (13)$$

and

$$\vec{r}_2 = (x + 1 - \mu) \hat{i} + y \hat{j} + z \hat{k} \quad (14)$$

with magnitude respectively:

$$|\vec{r}_1| = \sqrt{(x - \mu)^2 + y^2 + z^2} \quad (15)$$

$$|\vec{r}_2| = \sqrt{(x + 1 - \mu)^2 + y^2 + z^2} \quad (16)$$

Assuming that  $m_1 + m_2 \gg m_3$  (Eq.(1)),  $m_3$  “feels”  $m_1$ ’s and  $m_2$ ’s gravity but doesn’t affect their motion.

$$\vec{a}_g = -\frac{(1 - \mu)}{r_1^3} \vec{r}_1 - \frac{\mu}{r_2^3} \vec{r}_2 \quad (17)$$

Equating Eq.(8) to Eq. (17) and using the dot notation to denote time derivatives, the equations of motion (EOMs) of the CR3BP are obtained:

$$\begin{cases} \hat{i} : \ddot{x} - 2\dot{y} - x = -\frac{(1-\mu)(x-\mu)}{r_1^3} - \frac{\mu(x+1-\mu)}{r_2^3} \\ \hat{j} : \ddot{y} - 2\dot{x} - y = -\frac{(1-\mu)y}{r_1^3} - \frac{\mu y}{r_2^3} \\ \hat{k} : \ddot{z} = -\frac{(1-\mu)z}{r_1^3} - \frac{\mu z}{r_2^3} \end{cases} \quad (18)$$

We can use the definition of a pseudo-potential function  $U$ :

$$U = \frac{1}{2}(x^2 + y^2) + \frac{1-\mu}{r_1} + \frac{\mu}{r_2} \quad (19)$$

where  $\frac{1}{2}(x^2 + y^2)$  is the pseudo gravitational potential which is referred to the rotating reference frame and the other terms are the gravitational potential of  $m_1$  and  $m_2$  on  $m_3$ . The EOMS (Eq.(18)) can be rewritten as:

$$\begin{cases} \hat{i} : \ddot{x} - 2\dot{y} = \frac{\partial U}{\partial x} \\ \hat{j} : \ddot{y} + 2\dot{x} = \frac{\partial U}{\partial y} \\ \hat{k} : \ddot{z} = \frac{\partial U}{\partial z} \end{cases} \quad (20)$$

The EOMS of the CR3BP are  $2^{nd}$  order non-linear coupled ordinary differential equations. The non-linearity of these equations is due to the presence of  $r_1$  and  $r_2$  in the denominator.

In 1836, Jacobi calculated one integral of motion (known as Jacobi integral [22], discussed in detail in Section 2.3) while Poincarè, in 1892, proved that there are no other independent integrals of motion besides the Jacobi integral [23]. This means that Eqs.(20) generally have no analytical solution.

## 2.2 Lagrange Points

Starting from Eq.(18), we can identify the equilibrium points of the CR3BP, which are characterized by  $\ddot{x} = \ddot{y} = \ddot{z} = \dot{x} = \dot{y} = \dot{z} = 0$ . In other words, if an object were placed at one of these points, it would experience no acceleration and have zero velocity, thus remaining there indefinitely. Nullifying accelerations involves considering the equilibrium between gravitational and centrifugal forces.

Thus, Eq.(18) become a set of coupled algebraic equations in  $x$ ,  $y$  and  $z$ :

$$\begin{cases} x = \frac{(1-\mu)(x-\mu)}{r_1^3} + \frac{\mu(x+1-\mu)}{r_2^3} \\ y = \frac{(1-\mu)y}{r_1^3} + \frac{\mu y}{r_2^3} \\ 0 = -\frac{(1-\mu)z}{r_1^3} - \frac{\mu z}{r_2^3} \end{cases} \quad (21)$$

It can be seen that the  $x$ - and  $y$ -equations are coupled while the  $z$ -equation is completely decoupled from the other two. In particular, the only solution for  $z$  is  $z = 0$  and consequently all equilibrium points must lie in the  $xy$  plane, the plane of motion of the primaries. These equilibrium points are known as *Lagrange points*, which are positions in space where the gravitational forces of the two large bodies (the primaries) produce enhanced regions of attraction and repulsion, allowing for the stable placement of smaller objects, such as satellites or spacecraft.

**Equilateral points.** Setting  $r_1 = r_2$  (equating Eq.(13) and Eq.(14)) we can find two of the five solutions of Eq. (21):

$$\sqrt{(x - \mu)^2 + y^2 + z^2} = \sqrt{(x + 1 - \mu)^2 + y^2 + z^2} \quad (22)$$

Solving for  $x$  and using the non-dimensionalized equation  $r_1 = r_2 = a_1 + a_2 = 1$  to substitute in  $y$ , the equilateral points can be found:

$$(x, y) = \left( \mu - \frac{1}{2}, \pm \frac{\sqrt{3}}{2} \right) \quad (23)$$

These two points are called  $L_4$  and  $L_5$ .

**Collinear points.** Noting that  $y = 0$  is a solution of the second equation of Eq.(18), one can compute the  $x$ -values from the first equation. In particular, one can use the fact that  $r_1 = x - \mu$  and  $r_2 = x + 1 - \mu$ , both of which must be positive quantities since they represent physical distances, and substitutes them into the  $x$ -equation. This yields to:

$$x = \frac{(1 - \mu)(x - \mu)}{|x - \mu|^3} + \frac{\mu(x + 1 - \mu)}{|x + 1 - \mu|^3} \quad (24)$$

This algebraic equation has three real roots for  $x$  that correspond to the  $x$ -coordinates of the collinear points  $L_1$ ,  $L_2$ , and  $L_3$ .

**Stability of the Lagrange points.** In order to examine the local behavior of Lagrange points, which are denoted by the coordinates  $(x_e, y_e, z_e)$ , we aim to investigate the effects of perturbing the initial conditions (ICs).

$$\text{ICs: } \begin{cases} x = x_e + \delta_x \\ y = y_e + \delta_y \\ z = z_e + \delta_z \end{cases} \quad (25)$$

So  $r_1$  and  $r_2$  become:

$$\begin{aligned} r_1^{-3} &= [(x_e + \delta_x - \mu)^2 + (y_e + \delta_y)^2 + \delta_z^2]^{-3/2} \\ r_2^{-3} &= [(x_e + \delta_x + 1 - \mu)^2 + (y_e + \delta_y)^2 + \delta_z^2]^{-3/2} \end{aligned} \quad (26)$$

We can also define:

$$r_{ie} = \begin{cases} x_e & \text{for } L_1, L_2, \text{ and } L_5 \\ 1 & \text{for } L_4 \text{ and } L_5 \end{cases} \quad (27)$$

When we are in proximity to the Lagrange points, we can consider the linearized 2D EOMs described as follows:

$$\begin{cases} \ddot{\delta}_x - 2\dot{\delta}_y - (1 - A)\delta_x - B\delta_y = 0 \\ \ddot{\delta}_y - 2\dot{\delta}_x - B\delta_x + (1 - C)\delta_y = 0 \end{cases} \quad (28)$$

where A, B and C are constants defined as:

$$\begin{aligned}
A &= (1 - \mu) \left[ \frac{1}{r_{1e}^3} - 3 \frac{(x_e - \mu)^2}{r_{1e}^5} \right] + \mu \left[ \frac{1}{r_{2e}^3} - 3 \frac{(x_e + 1 - \mu)^2}{r_{2e}^5} \right] \\
B &= 3(1 - \mu) \left[ \frac{(x_e - \mu)y_e}{r_{1e}^3} + \frac{(x_e + 1 - \mu)y_e}{r_{2e}^5} \right] \\
C &= (1 - \mu) \left[ \frac{1}{r_{1e}^3} - 3 \frac{y_e^2}{r_{1e}^5} \right] + \mu \left[ \frac{1}{r_{2e}^3} - 3 \frac{y_e^2}{r_{2e}^5} \right]
\end{aligned} \tag{29}$$

We assume a solution of the form:

$$\begin{cases} \delta_x = C_1 e^{\lambda t} \\ \delta_y = C_2 e^{\lambda t} \end{cases} \tag{30}$$

We can compute  $d/dt$  and  $d^2/dt^2$  and plug them into the linearized EOMs. We will use the matrix form to obtain an eigenvalue problem.

$$\begin{bmatrix} \lambda^2 - (1 - A) & -B - 2\lambda \\ -B - 2\lambda & \lambda^2 - (1 - C) \end{bmatrix} \begin{Bmatrix} \delta_x \\ \delta_y \end{Bmatrix} = \begin{Bmatrix} 0 \\ 0 \end{Bmatrix} \tag{31}$$

Setting the determinant of the matrix to zero results in the characteristic equation:

$$\lambda^4 + \lambda^2(2 + C + A) + (1 - C - A - AC - B^2) = 0 \tag{32}$$

and its roots are:

$$\lambda = \pm \sqrt{-2 - C - A \pm \sqrt{2C + 2A + 1/4C^2 - 1/2AC + 1/4A^2 + B^2}} \tag{33}$$

For  $L_4$  and  $L_5$ , knowing that  $r_{1e} = 1$  (Eq. (27)), we obtain:

$$\lambda^2 = \frac{1}{2} \left( -1 \pm \sqrt{1 - 27\mu(1 - \mu)} \right) \tag{34}$$

To ensure stability, it is necessary for the real part of the eigenvalue to be equal to zero. Consequently, this requirement leads to the condition that the eigenvalue should be purely imaginary.

$$1 - 27\mu(1 - \mu) < 0 \tag{35}$$

Solving for  $\mu$ :

$$\mu < \frac{1}{18} \left( 9 - \sqrt{69} \right) \approx 0.0385209 := \mu^* \tag{36}$$

where  $\mu^*$  it's the critical mass ratio.

We can ignore the second root ( $\mu \approx 0.961479$ ) since  $\mu \leq 0.5$ .

So  $L_4$  and  $L_5$  are stable for all Sun-planet and planet-moon combos, except for Pluto-Charon system ( $\mu = 0.1085112 > \mu^*$ ). On the other hand,  $L_1$ ,  $L_2$  and  $L_3$  are all unstable for any value of  $\mu$ .

For the Saturn-Titan system, the mass ratio is  $\mu = 2.3663931583 \cdot 10^{-4}$ , which is the second largest mass ratio between a planet and a moon in the Solar System – for reference, the only larger value is the Earth-Moon’s mass ratio  $\mu = 1.2150585609 \cdot 10^{-2}$ . Lagrange points are represented in Figures 8 and 9. The non-dimensionalized and dimensional coordinates of these points for the Saturn-Titan system are summarized in Table 3.

Table 3: Lagrange points coordinates of Saturn-Titan system

Lagrange point	(x, y) [ND]	(x, y) [km]
$L_1$	(0.9574961733, 0)	(1144856.15, 0)
$L_2$	(1.0432564213, 0)	(1247397.71, 0)
$L_3$	(-1.0000985997, 0)	(-1195794.89, 0)
$L_4$	(0.4997633607, 0.8660254038)	(597555.56, 1035486.66)
$L_5$	(0.4997633607, -0.8660254038)	(597555.56, -1035486.66)

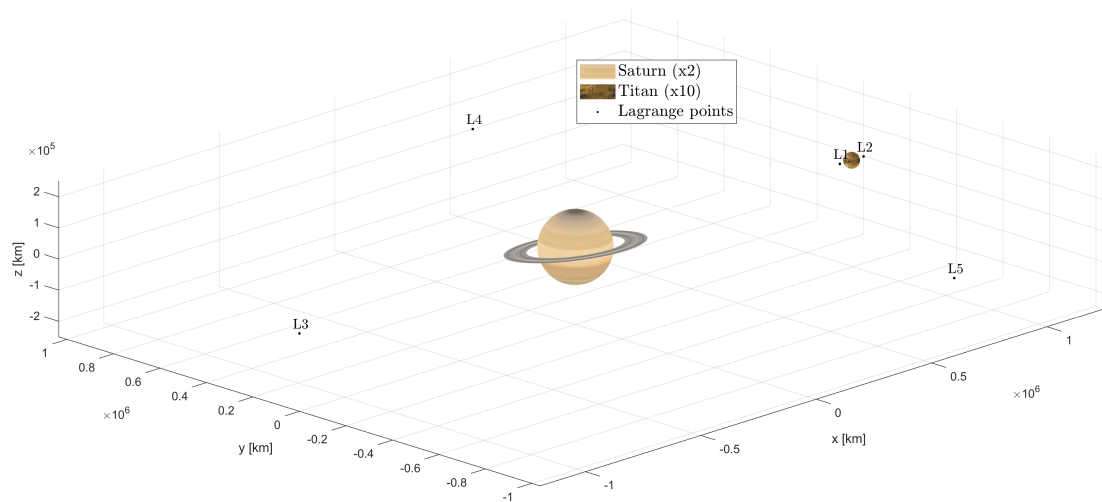


Figure 8: Lagrange points

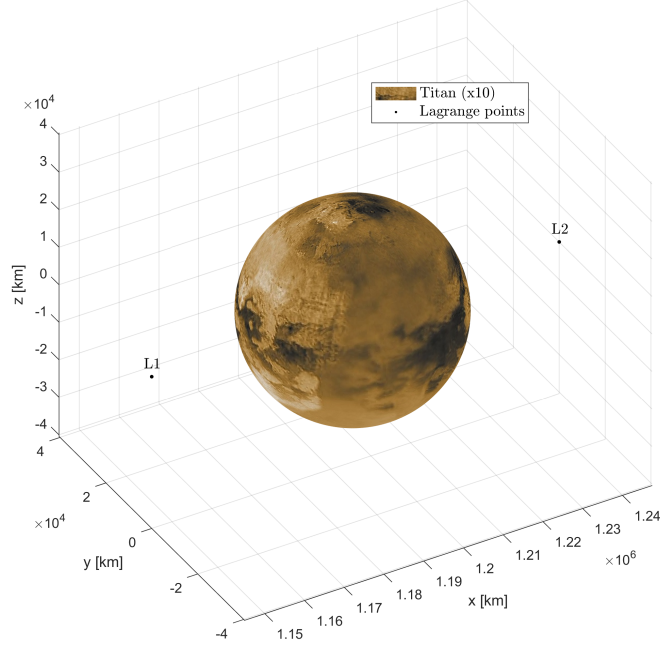


Figure 9: Lagrange points. Focus on Titan

### 2.3 Jacobi Integral

As mentioned in Section 2.1, in the CR3BP there is only one conserved quantity known as Jacobi integral, or Jacobi constant. The system's energy and momentum are not conserved individually, as opposed to the two-body problem (2BP). As a result, a general analytical solution for the CR3BP is impossible to find.

Starting from EOMs (Eq.(18)), we multiply each equation by  $\dot{x}$ ,  $\dot{y}$  and  $\dot{z}$  respectively, then sum up all the equations together:

$$\begin{aligned}
 & \dot{x}(\ddot{x} - 2\dot{y} - x) + \dot{y}(\ddot{y} + 2\dot{x} - y) + \dot{z}\ddot{z} = \\
 & = \dot{x} \left[ -\frac{(1-\mu)(x-\mu)}{r_1^3} - \frac{\mu(x+1-\mu)}{r_2^3} \right] + \\
 & + \dot{y} \left[ -\frac{(1-\mu)y}{r_1^3} - \frac{\mu y}{r_2^3} \right] + \dot{z} \left[ -\frac{(1-\mu)z}{r_1^3} - \frac{\mu z}{r_2^3} \right]
 \end{aligned} \tag{37}$$

Noting that known quantities such as kinetic energy, centrifugal force and potential energy appear in Eq.(37), we can combine all the terms:

$$0 = \frac{d}{dt} \left[ \frac{1}{2} V^2 - \frac{1}{2} (x^2 + y^2) - \frac{(1-\mu)}{r_1} - \frac{\mu}{r_2} \right] \tag{38}$$

where  $V = \sqrt{\dot{x}^2 + \dot{y}^2 + \dot{z}^2}$  represents the velocity of  $m_3$ . In order for the derivative to be zero, the quantity in the square brackets must be constant. This quantity is called the Jacobi integral (or Jacobi constant):

$$J = \frac{1}{2}(\dot{x}^2 + \dot{y}^2 + \dot{z}^2) - \frac{1}{2}(x^2 + y^2) - \frac{(1-\mu)}{r_1} - \frac{\mu}{r_2} \quad (39)$$

where the first term represents the system's kinetic energy while the second term corresponds to the centrifugal force. The final two terms are associated with the system's potential energy.

If we consider the case of  $V = 0 \Rightarrow \dot{x} = \dot{y} = \dot{z} = 0$ , we obtain what are commonly referred to as zero-velocity surfaces or Hill surfaces. The zero-velocity surfaces (some examples are shown in Figure 10, 11, 12, 13 and 14), in essence, denote boundaries that an object can't cross due to a lack of energy.

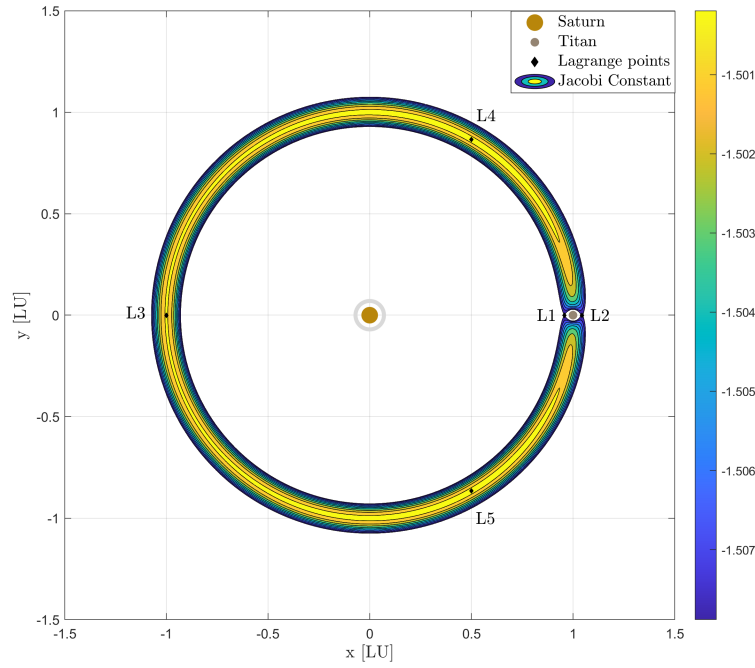


Figure 10: Zero-velocity curves for the Saturn-Titan system for  $J=J(L_1)=-1.50791$

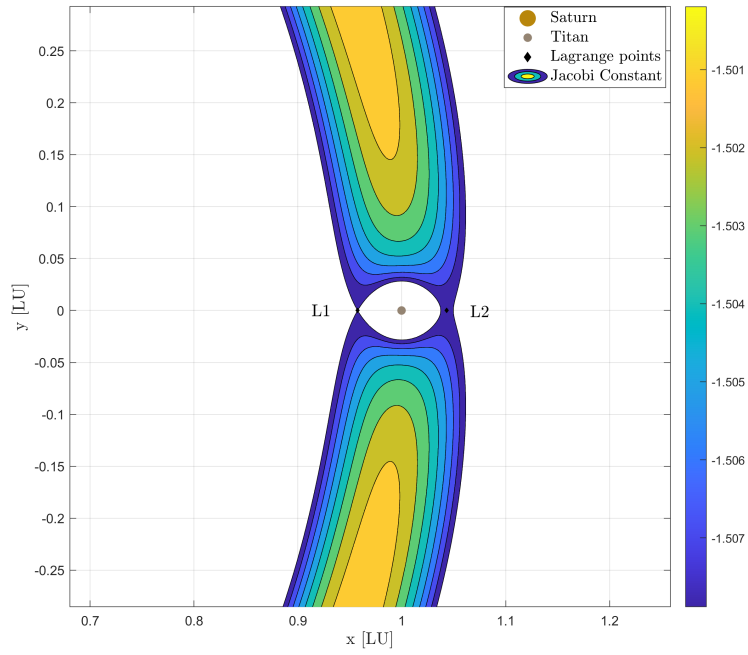


Figure 11: Zero-velocity curves for the Saturn-Titan system for  $J=J(L_1)=-1.50791$ .  
Zoomed-in view

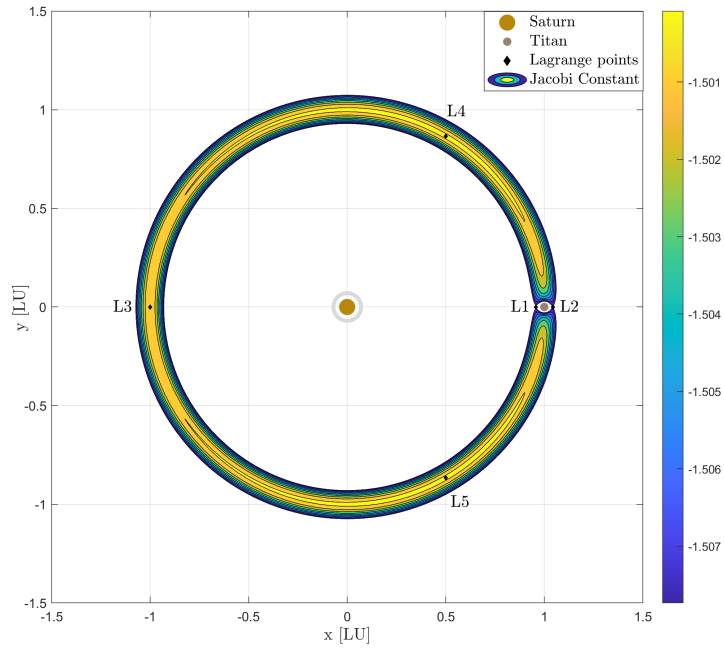


Figure 12: Zero-velocity curves for the Saturn-Titan system for  $J=J(L_2)=-1.50777$

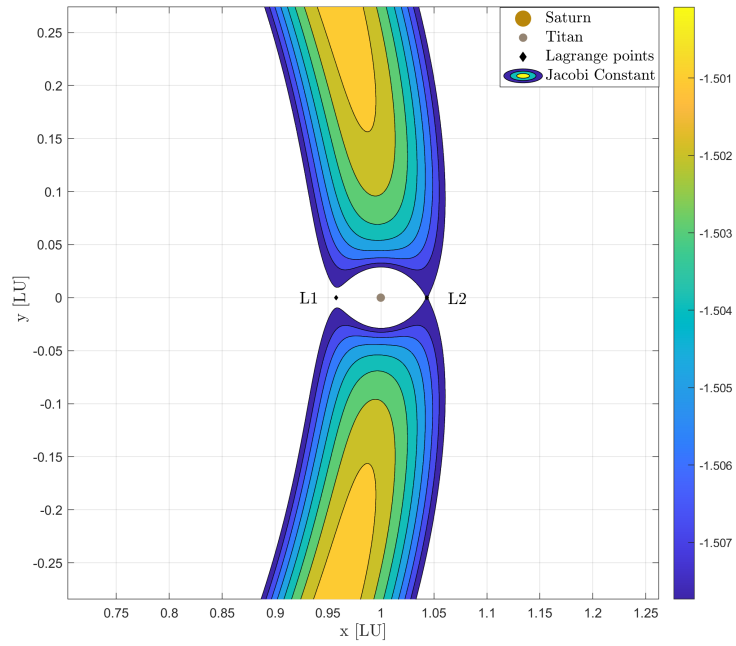


Figure 13: Zero-velocity curves for the Saturn-Titan system for  $J=J(L_2)=-1.50777$ .  
Zoomed-in view

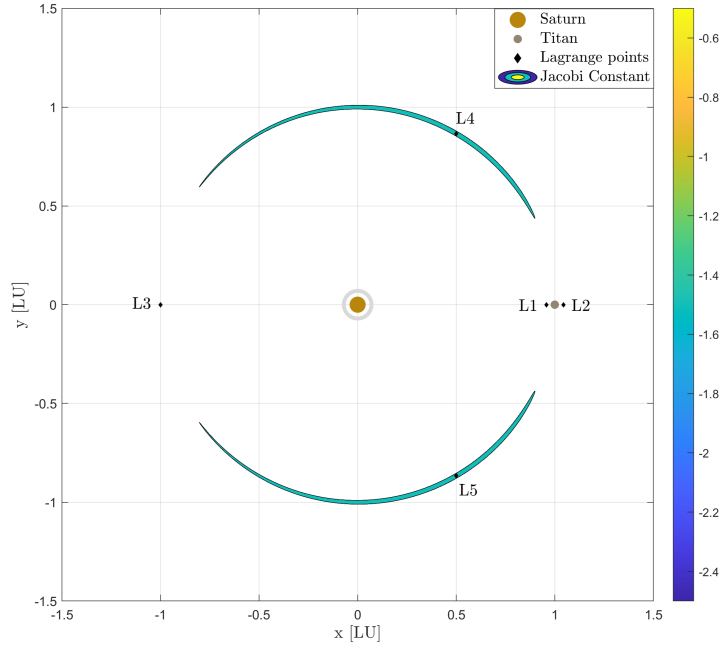


Figure 14: Zero-velocity curves for the Saturn-Titan system for  $J=J(L_3)=-1.50012$

## 2.4 Periodic Orbits in the CR3BP and Applications in Space Missions

Since the gravitational interaction between the three bodies in the CR3BP can't be easily addressed analytically, mathematical analysis techniques and numerical modeling are generally required to study the problem.

An important set of solutions of the CR3BP is periodic orbits, in which the third body repeats a certain trajectory after a given period of time. These orbits are trajectories that retrace their path in the synodic reference frame over time while quasi-periodic orbits trace a nearby path that is confined to a particular region in the synodic frame [24]. There are several types of periodic orbits and the choice of orbit depends on the specific needs of the mission.

The key features of several types of orbits will be discussed in the following section, along with an analysis of potential applications for a mission to Titan.

- **Lyapunov orbits**

Lyapunov orbits, also known as Lagrange point orbits, are a class of orbits named after Aleksandr Lyapunov, a Russian mathematician known for his contributions to the study of stability in dynamical systems.

Lyapunov orbits exhibit intricate shapes and sizes, tracing a curved trajectory around the Lagrange point. These types of orbits tend to be rather unstable, thus requiring the expenditure of fuel for station-keeping maneuvers.

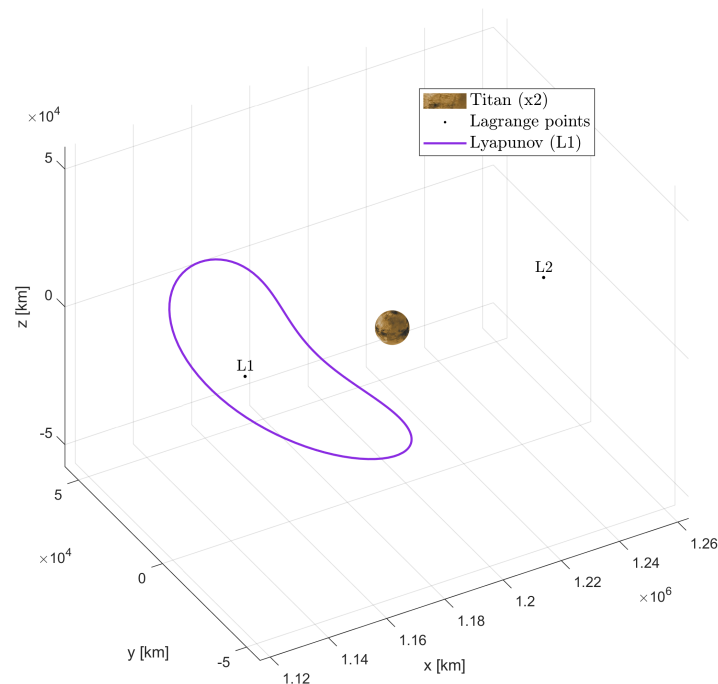


Figure 15: A planar Lyapunov orbit around  $L_1$  with  $J=-1.50417817$

These orbits have several practical applications. Space observatories stationed in Lyapunov orbits near the  $L_1$  point on Titan offer the advantage of conducting extended observations of Titan and its surroundings, eliminating the need for frequent orbital adjustments. They can serve as reliable communication relays for transmitting data between spacecraft exploring Titan’s surface or studying Saturn and its other moons. Launching and navigating spacecraft to and from a Lyapunov orbit can be very energy-efficient. These orbits also present opportunities for gravitational research and the testing of gravitational theories in the Saturn-Titan environment.

- **Axial and vertical orbits**

Axial orbits derive their name from their apparent rotation around the x-axis, originating from bifurcation of Lyapunov orbits, while vertical orbits are characterized by small amplitude motion in the z-direction [25].

Axial orbits offer significant utility in the study of celestial bodies as they enable prolonged observation of specific locations on the surface. This extended observation period allows for the examination of various properties and changes over time. On the other hand, vertical orbits prove valuable in mapping and studying the surface of a celestial body. By traversing both the north and south poles of the celestial body, vertical orbits enable observations of the both poles within a single mission.

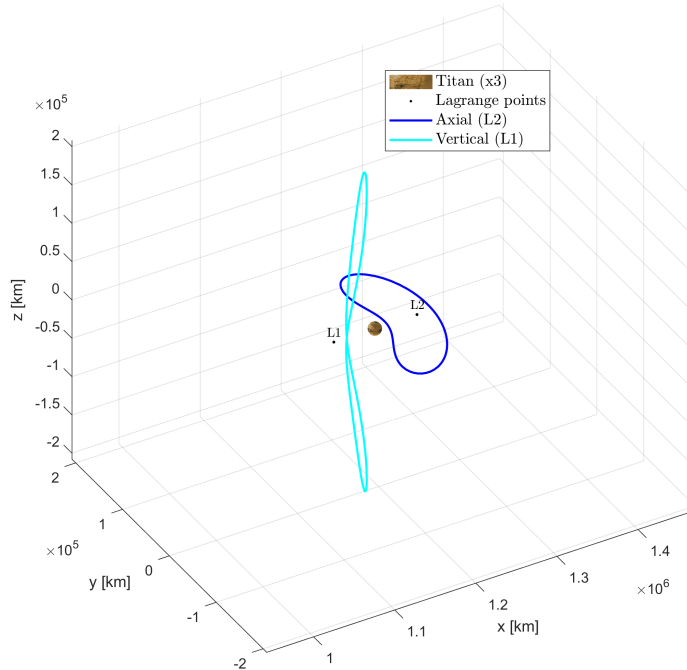


Figure 16: An axial orbit around the  $L_2$  point ( $J=-1.50181178$ ) and a vertical orbit around  $L_1$  point ( $J=-1.48570466$ )

In the case of Titan, both axial and vertical orbits could be useful for studying its atmosphere and surface features. A vertical orbit could allow for long-term observation of specific regions of interest, such as the polar regions, including the possibility of observing features such as the methane lakes and seas at the poles. An axial orbit could facilitate the mapping of the surface, allowing for the study of craters and dunes in the equatorial region of Titan.

Various aspects, such as the composition and seasonal variations of Titan's clouds, the significance of exchanges between the surface and atmosphere, transportation within the surface and subsurface, and the importance of ethane, constitute some of the many aspects of Titan's hydrological system that remain unexplored.

- **Butterfly and dragonfly orbits**

Butterfly and dragonfly orbits are special types of orbits that have been proposed for space missions. Butterfly orbits are three-dimensional orbits that resemble the shape of a butterfly, while dragonfly orbits consist of a series of figure-eight loops around two Lagrange points.

Both the butterfly and dragonfly orbits have potential applications in various space missions, including planet observation, remote sensing, and scientific missions. These orbits offer unique advantages over traditional orbit types, such as increased coverage and observation time.

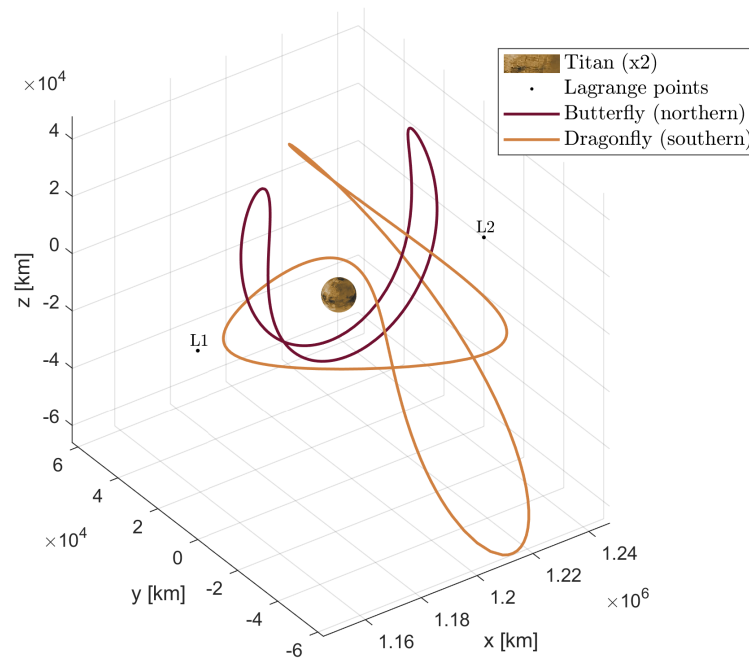


Figure 17: A butterfly (northern) orbit ( $J=-1.50456526$ ) and a dragonfly (southern) orbit ( $J=-1.50062838$ )

However, they also present significant challenges in terms of mission planning and spacecraft design, as the complex nature of these orbits requires careful consideration of the gravitational forces acting on the spacecraft, the precision of navigation systems and the required propulsion systems.

These types of orbits are particularly interesting when considering orbital transfer from one Lagrange point to another.

- **Halo orbits**

These orbits were named *halo* for the first time by Farquhar in 1968 [26] because of their distinctive shape, which resembles a halo around one of the primary bodies when observed from the other primary.

Halo orbits can be used for a variety of applications, including scientific missions and telecommunications: halo orbit allows a spacecraft to make repeated passes over the same region of Titan, which allows for more detailed observations but these orbits tend to be unstable, so station-keeping using thrusters may be required to keep a satellite on the orbit.

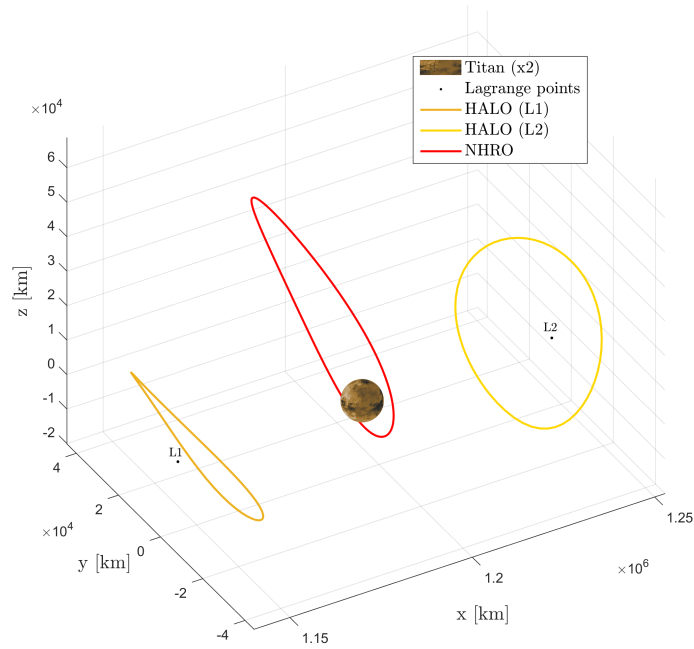


Figure 18: A halo orbit around  $L_1$  ( $J=-1.50650741$ ), a halo orbit around  $L_2$  ( $J=-1.50631369$ ) and a northern near-rectilinear halo orbit ( $J=-1.50175791$ )

In the case of Titan a halo orbit can be used to study its surface features, such as its methane lakes and rivers. A halo orbit can also serve as an invaluable tool for atmospheric studies. This special orbit configuration enables a spacecraft to maintain a continuous line of sight with a consistent hemisphere of Titan. This advantageous feature simplifies the process of conducting extended observations

and measurements of the moon's atmosphere. By remaining fixed with respect to a specific area of Titan's surface, scientists can gather comprehensive data over prolonged durations, fostering a deeper understanding of its atmospheric dynamics and composition.

Near-rectilinear halo orbits (NRHOs) are short-period halo orbits with large amplitudes over either the north or south pole that pass closely to the opposite pole. While they appear to look like large elliptical orbits about the smaller primary, they are CR3BP orbits that remain relatively fixed in the Saturn-Titan plane, rotating at the same rate as Titan around Saturn and Titan around its own axis [27].

An NRHO would be useful for studying Titan's poles, which are highly intriguing and have unique features as we saw in Chapter 1. The Cassini-Huygens mission discovered liquid methane and ethane lakes and seas at the north and south poles. Stable liquids on the surface of a celestial planet, like methane lakes, are a rare occurrence in our Solar System, and their dynamics and genesis are of significant interest [16].

- **Distant retrograde orbits**

Distant retrograde orbits (DROs) are a family of periodic CR3BP orbits, where the motion of a spacecraft is in the opposite direction to that of the second gravitational body. The interaction with two Lagrange points ( $L_1$  and  $L_2$ ) of the planet-moon system makes them marginally stable orbits.

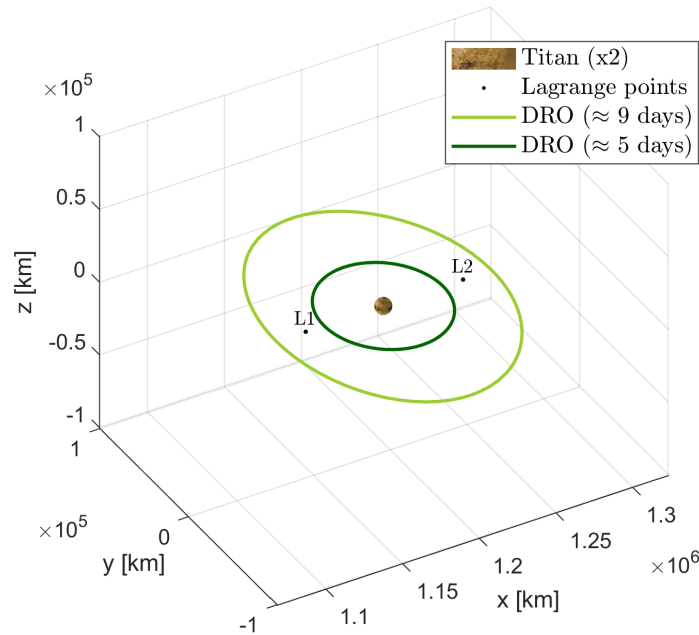


Figure 19: A DRO ( $\approx 5$  days) with  $J = -1.50054681$  and a DRO ( $\approx 9$  days) with  $J = -1.49801423$

If a spacecraft were in a DRO around a moon, it would orbit the moon in the opposite direction from that in which it orbits the planet.

DROs have been studied for several decades and are particularly relevant for space exploration missions. This type of orbit has the potential to be useful for a variety of applications, such as long-term observation and exploration of celestial bodies [28] [29] [30].

Titan’s methane-ethane lakes and seas, complex organic chemistry, and weather were all revealed by Cassini flybys, although these phenomena could not be fully investigated because of equipment and flyby coverage restrictions. A Titan orbiter may examine how Titan’s organic chemical factory functions both above and below the surface, giving Dragonfly (see Section 1.3) data and other global measurements crucial context.

A table summarizing the main characteristics of the periodic CR3BP orbits described in this section is shown in Table 4.

Table 4: Examples of CR3BP candidate orbits characteristics between Saturn and Titan

<b>Orbit</b>	<b>Period [days]</b>	<b>Jacobi constant</b>
Lyapunov ( $L_1$ )	8.37735059	-1.50417817
Axial ( $L_2$ )	10.25913124	-1.50181178
Vertical ( $L_1$ )	14.55564489	-1.48570466
Halo ( $L_1$ -northern)	7.33084198	-1.50650741
Halo ( $L_2$ -southern)	7.73671425	-1.50631369
NRHO ( $L_1$ -northern)	4.63208591	-1.50175791
Butterfly (northern)	9.48828164	-1.50456526
Dragonfly (southern)	15.31352828	-1.50062838
DRO ( $\approx 9$ days)	9.24733419	-1.49801423
DRO ( $\approx 5$ days)	4.67679262	-1.50054681

### 3 Assessing CR3BP Orbits: A Trade-off Analysis

As we have seen in Section 2.4, there are several families of orbits for the CR3BP, which can be obtained by considering different initial conditions and integrating the equations of motion (Eq. 18). In this chapter, we delve into a thorough analysis of the different orbit families, taking into account their specific characteristics and advantages. By conducting a comprehensive assessment of these orbit families, we can ultimately determine which one aligns best with our mission objectives and scientific goals in studying Titan's surface. This thorough evaluation will serve as the foundation for making an informed choice and optimizing the success of the mission.

#### 3.1 Saturn's Accessibility

It is important to note that the CR3BP orbits were defined in a reference system centered on Titan. As a result, these orbits are graphically represented using a rotational reference frame (RRF). In reality Titan orbits Saturn, giving the orbital "shape" seen from an inertial reference frame (IRF) centered on Saturn a variable appearance. This alternative representation proves valuable for determining the time during which the probe will be out of Saturn's sight.

Figure 20 shows a plot of a halo orbit around  $L_1$  in the rotational reference frame. The spacecraft keeps a fixed line of sight with Titan while it travels along this orbit. This happens as a result of Titan's orbital period being the same as its rotational period.

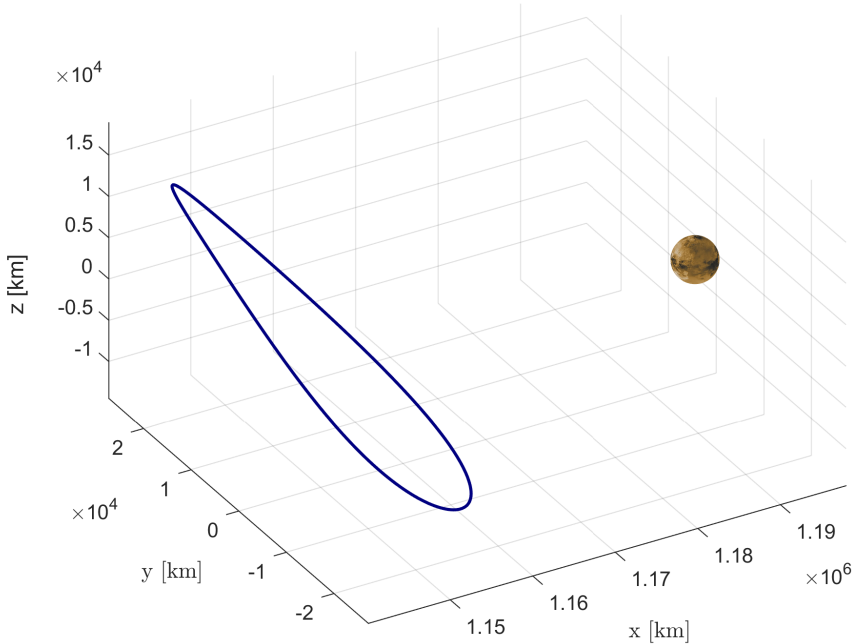


Figure 20: Halo orbit around  $L_1$  in the rotational reference frame

As Titan orbits around Saturn, the halo orbit around the  $L_1$  Lagrange point will consistently maintain a specific orientation relative to both Titan and Saturn. The reason for this occurrence is that the entire Saturn-Titan system effectively revolves around its combined center of mass, which is found within Saturn due to its significantly greater mass compared to Titan. The Lagrange points, including  $L_1$ , rotate continuously as a result of the system's overall rotation. This means that the  $L_1$  Lagrange point will always stay in a configuration where it remains in line with both Titan and Saturn as they move in their respective orbits. By ensuring that Titan and Saturn's gravitational fields balance, objects in the halo orbit at  $L_1$  are kept comparatively stable with respect to both celestial bodies.

A halo orbit around  $L_1$  is shown in Figure 21 when viewed in the inertial reference frame, which has origin at the barycenter of the system. As previously explained, it becomes clear that the halo orbit around  $L_1$  will always remain entirely encircled by the red dashed trajectory, which represents Titan's trajectory around Saturn. A video depicting the trajectory of the Halo orbit around  $L_1$  in the inertial reference frame can be found at [this link](#)<sup>1</sup>.

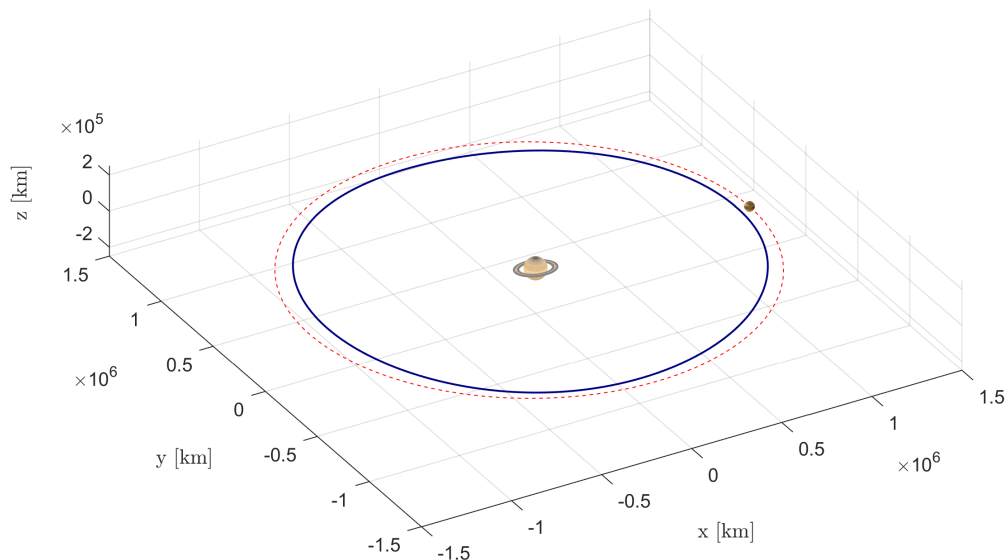


Figure 21: Halo orbit around  $L_1$  in the inertial reference frame. Video available [here](#)<sup>1</sup>

Another example can be illustrated by the depiction of DROs in both reference frames. By being able to complete an entire orbit around the secondary celestial body, in this case Titan, DRO orbits are distinguished from other types of orbits. A DRO orbit around Titan in the rotational reference frame is shown in Figure 22.

<sup>1</sup><https://youtu.be/IGqLMqMeJS4>

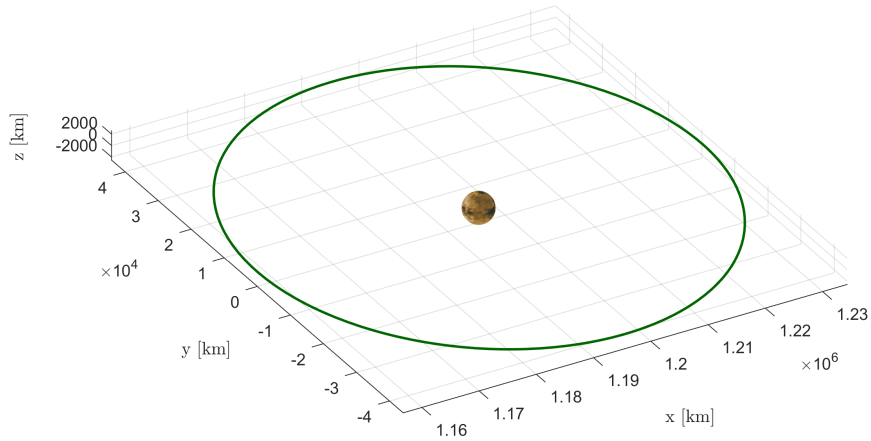


Figure 22: DRO in the rotational reference frame

If we switch from a rotational reference frame to a inertial reference frame, the resulting plot in Figure 23 reveals an interesting observation: at certain points along the DRO, which shares the same plane as Titan’s trajectory, the spacecraft lags behind Titan. This results in scenarios where a spacecraft in a DRO would be positioned behind Titan, consequently obstructing the spacecraft’s view of Saturn.

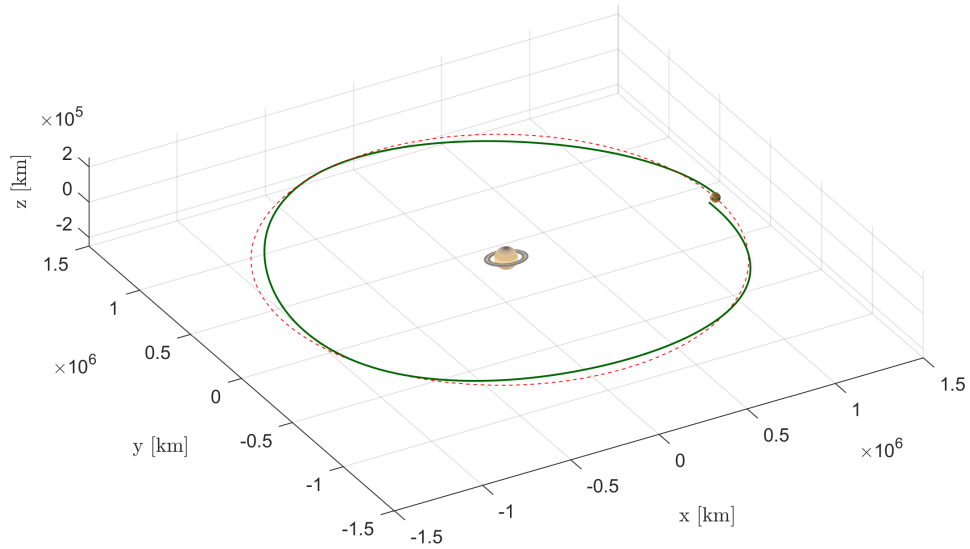


Figure 23: DRO in the inertial reference frame

Taking into account the CR3BP orbits discussed in Section 2.4, we have obtained Table 5, in which we have analyzed the duration (in % of the period and in days) of Saturn’s occultation due to Titan:

Table 5: CR3BP candidate orbits: Saturn visibility

Orbit	Period [days]	Saturn occultated [%]	Saturn occultated [days]
Lyapunov ( $L_1$ )	8.377	0	0
Axial ( $L_2$ )	10.259	9.417	0.9661
Vertical ( $L_1$ )	14.556	8.651	1.2591
Halo ( $L_1$ -northern)	7.3308	0	0
Halo ( $L_2$ -southern)	7.7367	0	0
NRHO ( $L_1$ -northern)	4.6321	0	0
Butterfly (northern)	9.4883	0	0
Dragonfly (southern)	15.314	0	0
DRO ( $\approx 9$ days)	9.2473	10.072	0.9314
DRO ( $\approx 5$ days)	4.6768	13.889	0.6496

### 3.2 Titan's Surface Visibility

Another crucial parameter to take into account is the percentage of Titan's surface visible from the orbit. While increasing the distance from the surface leads to reduced resolution, our main concern is to calculate the portion of Titan's surface that remains within the observable field of view.

In our analysis, we initiated the process by choosing a specific point along the CR3BP orbit and regarded it as the apex of a cone aimed toward Titan. The area where this cone intersects with Titan's surface defines the visible section of Titan for that specific point on the orbit.

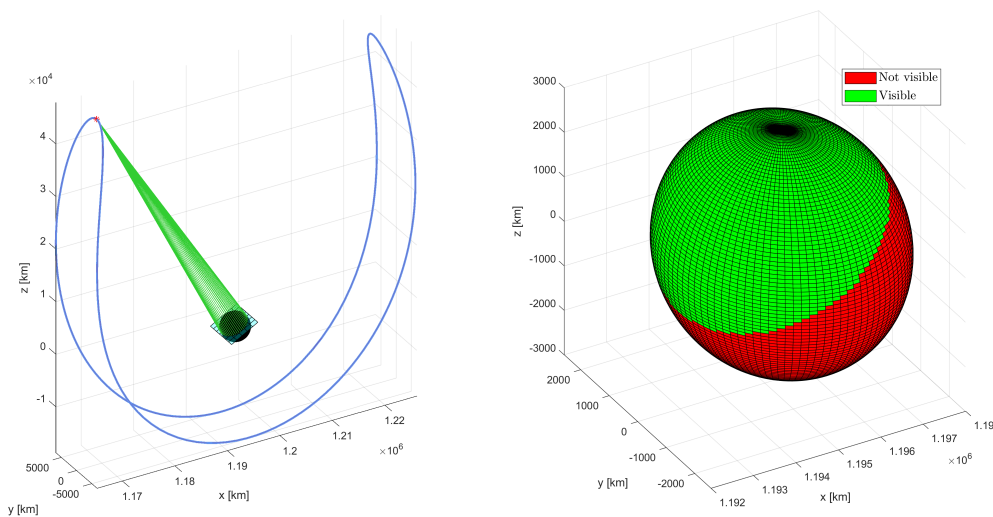


Figure 24: Field of view from a specific position on a Butterfly orbit

In Figure 24, it can be seen the plane formed by the cross-section of the spherical sector resulting from the intersection of the cone and Titan, here modeled as a perfect sphere. Within the same figure, the portion of Titan’s surface that becomes observable from that particular position along the orbital path can also be seen. In this figure, we have considered a Butterfly orbit as an example.

In the configuration depicted in Figure 24, we can assert that we are able to observe 43.72% of Titan’s surface.

By extending this idea to all the points along the orbit, we can determine the percentage of Titan’s surface visible from a given orbit during one full orbital period. In the case of the Butterfly orbit, due to its unique shape, it is possible to observe the entirety of Titan’s surface, albeit with lower resolution in portions where the orbit is significantly distant from the surface.

An interesting scenario to analyze is when we consider a halo orbit, specifically referring to a halo orbit around  $L_2$ . It is obvious that it is impossible to see Titan’s whole surface, even while taking into account every point along the halo orbit (as illustrated in Figure 25). This restriction results from the orbit’s constant alignment with Titan’s same side.

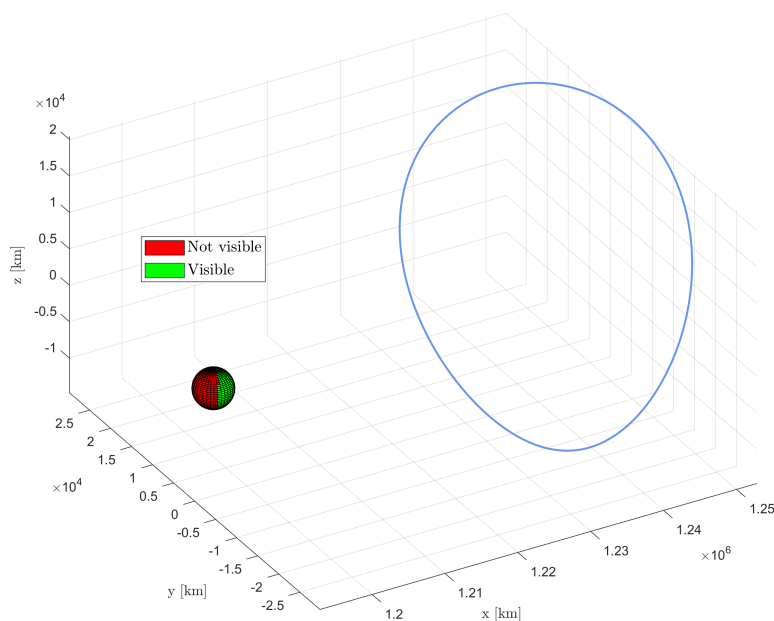


Figure 25: Titan’s surface visibility for a halo orbit around  $L_2$

We may evaluate the portion of the Saturnian moon’s surface that is visible from the halo orbit around  $L_2$  by looking more closely at its representation (Figure 26). The portion of Titan’s surface that can be seen from this particular halo orbit is about 64.35%.

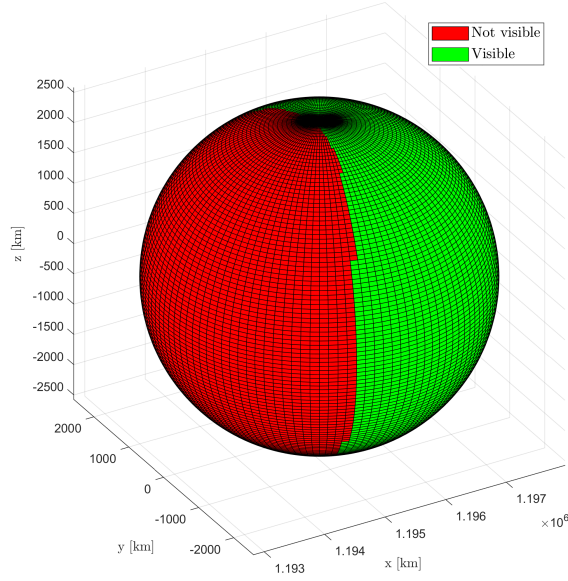


Figure 26: Titan’s surface visibility for a halo orbit around  $L_2$  (zoom on Titan’s surface)

At this point, we can update Table 5 presented earlier, taking into account Titan’s surface visibility as well. Table 6 summarizes the characteristics described thus far.

Table 6: CR3BP candidate orbits: Titan visibility

Orbit	Period [d]	Saturn occultated [%]	Saturn occultated [d]	Titan’s surface visibility [%]
Lyapunov ( $L_1$ )	8.377	0	0	76.20
Axial ( $L_2$ )	10.259	9.417	0.9661	91.90
Vertical ( $L_1$ )	14.556	8.651	1.2591	88.27
Halo ( $L_1$ )	7.3308	0	0	64.79
Halo ( $L_2$ )	7.7367	0	0	64.35
NRHO ( $L_1$ )	4.6321	0	0	99.68
Butterfly	9.4883	0	0	100.00
Dragonfly	15.314	0	0	99.87
DRO ( $\approx 9$ days)	9.2473	10.072	0.9314	87.10
DRO ( $\approx 5$ days)	4.6768	13.889	0.6496	80.65

The results are significantly impacted by the choice of orbit, even when considering orbits within the same family. In our specific case, the NHRO orbit is situated in close proximity to Titan’s surface, allowing for an almost complete view of its surface.

In the case of DROs, we observe that the surface coverage is quite extensive. The shape of the orbit enables a  $360^\circ$  view of Titan, with the exception of the poles that remain out of sight. Notably, as we move farther away (and consequently increase the orbit’s period), the portion of visible surface also increases, albeit at the cost of resolution.

### 3.3 Stability

To conclude, we must also consider the stability of these orbits. We have derived them by considering the CR3BP, incorporating the gravitational influences of Titan and Saturn while excluding any external perturbations. In reality, these orbits are indeed perturbed by the presence of other celestial bodies in space, such as the massive influence of the Sun or Jupiter, or the presence of all the other Saturnian moons.

This is why the concept of orbit stability is important to assess an orbit’s ability to resist being influenced by perturbations. It’s impossible to expect that a spacecraft orbiting according to a CR3BP orbit will maintain the same path for an extended period. Over time, external perturbations will gradually cause variations, necessitating spacecraft maneuvers and thus, fuel consumption.

To evaluate the orbital stability, we introduce the Stability Index [31], given in Table 7. This index ranges from 1 (indicating a completely stable orbit) to much higher values, signifying an unstable orbit that requires constant corrections.

In essence, while these orbits provide valuable insights into visibility and coverage, their long-term practicality hinges on their stability in the face of external perturbations, a crucial consideration for spacecraft mission planning.

Table 7: CR3BP candidate orbits: Stability index

Orbit	Stability index
Lyapunov ( $L_1$ )	3.89469275627888E+2
Axial ( $L_2$ )	1.58028851350330E+2
Vertical ( $L_1$ )	2.61939577137195E+2
Halo ( $L_1$ -northern)	6.39280628625028E+2
Halo ( $L_2$ -southern)	5.39208380823829E+2
NRHO ( $L_1$ -northern)	1.93244112461674E+0
Butterfly (northern)	5.28330760821393E+0
Dragonfly (southern)	3.70087836653840E+2
DRO ( $\approx$ 9 days)	1.00000000071544E+0
DRO ( $\approx$ 5 days)	1.0000000000414E+0

DROs are generally considered more stable compared to other orbits: this stability arises from unique dynamical features, such as the presence of resonance ratios (e.g. 2:1 or 3:1) with Titan’s orbital period. These resonance ratios create gravitational interactions that contribute to stabilizing the orbit over time. Additionally, DROs are located at a significant distance from Titan, reducing its influence. This combination of resonance behavior and distant position contributes to their long-term stability.

The stability of NHROs is significantly influenced by the specific orbit under consideration. Typically, their stability is attributed to their proximity to the  $L_1$  or  $L_2$  Lagrange points within the Saturn-Titan system. These Lagrange points offer a degree of gravitational stability, minimizing perturbations. NRHOs are also situated in regions with relatively low gravitational influence from other celestial bodies, contributing to their long-term stability.

### 3.4 Orbit Selection

The Dragonfly mission, scheduled for mid-2030s to study Titan’s equatorial region (as discussed in Section 1.3), aims to provide a comprehensive understanding of Saturn’s moon’s surface composition. However, it is essential to acknowledge that, despite its great potential, this mission comes with certain limitations due to its localized nature. The primary goal of Dragonfly is to collect and analyze samples from multiple sites on Titan’s surface using the rotorcraft lander to gain detailed information about surface composition. Still, it cannot provide global coverage. Regions like the polar areas or high-altitude locations may exhibit distinct geological formations or compositional variations that Dragonfly will not directly study.

The mission’s localized nature and inherent limitations in mobility, sampling, and available resources may impose constraints on achieving a comprehensive global understanding of Titan. Nevertheless, the data and insights gathered from this mission will undoubtedly represent a significant advancement in our knowledge of this moon.

Currently, Dragonfly mission team has designated the Selk crater as its landing site (Figure 27), located in Titan’s equatorial region [32]. While this choice aligns with specific scientific objectives, it signifies that there is much more of this enigmatic moon left to explore.

Given the progress of the Dragonfly mission and its potential for significant discoveries, it’s worth considering the need for future missions to further expand our comprehension of Titan by exploring other regions and terrains. The Selk crater may be a promising starting point, but the diverse and complex nature of Titan calls for ongoing exploration and missions that encompass a broader geographical range.

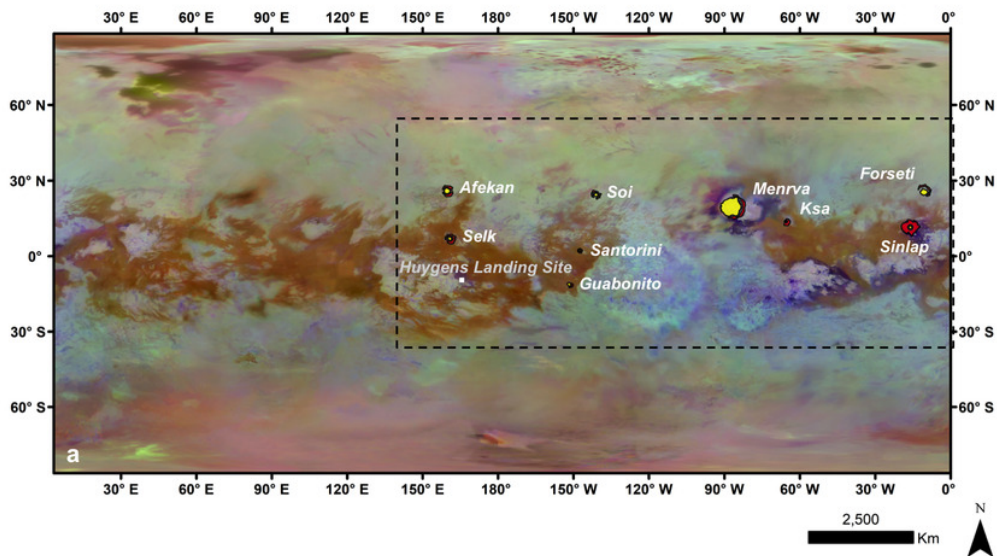


Figure 27: Dragonfly landing site [32]

Considering the various parameters analyzed in this chapter, it's clear that DRO emerges as the preferred orbital choice due to its exceptional stability and broad coverage of Titan's surface. However, this preference involves a trade-off, as it requires accepting limitations on the exploration of Titan's polar regions in exchange for the benefits of enhanced orbit stability and reduced fuel consumption during station-keeping maneuvers.

Elaborating on this strategic decision in mission planning, opting for DROs represents a carefully considered compromise. While it may restrict access to polar regions that hold scientific interest, the advantages in terms of orbit stability and fuel efficiency are pivotal for the mission's overall success and duration. DROs facilitate sustained and consistent observations, reducing the need for frequent orbital adjustments and conserving resources for other mission objectives. This equilibrium between polar exploration and orbit stability optimizes mission performance.

A mission conducted in a DRO around Titan would extend and complement Dragonfly's regional exploration, providing a global-scale perspective. Additionally, it presents a unique opportunity to investigate intriguing phenomena such as cryovolcanoes, which erupt icy materials and have been observed in specific equatorial regions[33]. This broader scope of exploration would significantly enhance our understanding of ongoing geological processes on Titan and their impact on the moon's evolution.

In conclusion, a mission in a DRO around Titan offers a strategic complement to Dragonfly's regional exploration, facilitating comprehensive global-scale investigation. By incorporating the study of cryovolcanoes and other geologic features beyond Dragonfly's reach, this mission would provide essential context for comprehending Titan's surface composition, ongoing geological dynamics, and the evolution of this intriguing moon.

## 4 Dynamical Systems Theory

Dynamical Systems Theory (DST), also known as ‘chaos theory’, is a mathematical framework employed to examine complex, time-evolving systems by analyzing their responses to specific initial conditions and external forces. In astrodynamics, the complexity and sensitivity of the N-body problem to initial conditions is a typical characteristic of such a chaotic system. When we discuss the N-body problem, we refer to a situation where multiple celestial bodies interact gravitationally. This intricate web of gravitational forces produces a chaotic behavior, where small changes in initial conditions can lead to dramatically different orbital paths. For instance, when examining a planetary system with multiple bodies interacting, altering the initial positions or velocities of these celestial objects by the slightest change can lead to orbits that diverge significantly over time. This phenomenon emphasizes the crucial importance of DST in comprehending and simulating such phenomena within interplanetary trajectories by demonstrating the inherent unpredictability and complexity associated with chaotic systems.

Notable achievements in trajectory design for libration point missions have been realized through the application of DST [34]. Prominent examples include the Genesis mission, which collected and analyzed solar particles in a halo orbit around the L1 point of the Sun-Earth system [35], and the James Webb Space Telescope mission, positioned at the L2 point of the Sun-Earth system, enabling groundbreaking astronomical discoveries across various wavelengths [36].

In the next section, we will explore how the State-Transition Matrix (STM) is used to represent the states of celestial bodies and how this mathematical representation is essential to understanding and predicting orbital evolution in a gravitational environment strongly influenced by DST principles.

### 4.1 State-Transition Matrix

In orbital mechanics, the state-space representation of a dynamical system provides a powerful framework for describing the dynamics of celestial bodies. The state vector, denoted as  $\mathbf{X}$ , includes positions and velocities along the three coordinate axes. These parameters can be conveniently organized into a vector, and the behavior of an object in motion can be described by a set of six first-order differential equations.

The state-transition matrix is a 6x6 square matrix that characterizes how the state of a spacecraft evolves from one time  $t$  to a future time  $t + \Delta t$ . To express this mathematically, if  $\mathbf{X}(t)$  represents the state vector at time  $t$  and  $\mathbf{X}(t + \Delta t)$  represents the state vector at time  $t + \Delta t$ , the relationship can be articulated as follows:

$$\mathbf{X}(t + \Delta t) = A(t) \cdot \mathbf{X}(t) \tag{40}$$

In this context,  $A(t)$  encapsulates the dynamics of the object’s orbit and is crucial for predicting its future positions and velocities. It allows us to map the state of an object at a given time to its state at a future time.

It's important to note that there is a distinction between  $A(t)$  and the State-Transition Matrix (STM). While  $A(t)$  characterizes the instantaneous rate of change of state variables, the STM provides a comprehensive mapping to the initial conditions of how the state variables evolve over a finite time interval. In many cases, the STM must be calculated numerically due to the intricate and nonlinear nature of celestial dynamics, especially in scenarios involving multiple gravitational interactions and complex trajectories.

In the two-body problem, obtaining the STM typically requires numerical computation unless simplifications are applied, like the Hill-Clohessy-Wiltshire EOMs for the relative motion. These simplifications aim to streamline the calculations by assuming specific conditions or constraints, allowing for a more tractable analytical approach.

For the CR3BP we can recall the pseudo-potential, represented as:

$$U = \frac{1}{2}(x^2 + y^2) + \frac{1 - \mu}{r_1} + \frac{\mu}{r_2} \quad (41)$$

This pseudo-potential can be expanded using a Taylor series. Let's consider an expansion with respect to the variable  $x$ :

$$\begin{aligned} \frac{\partial U}{\partial x} &= \frac{\partial}{\partial x} \left( \frac{\partial U}{\partial x} \right) x + \frac{\partial}{\partial y} \left( \frac{\partial U}{\partial x} \right) y + \frac{\partial}{\partial z} \left( \frac{\partial U}{\partial x} \right) z + \\ &+ \frac{\partial}{\partial \dot{x}} \left( \frac{\partial U}{\partial x} \right) \left( \frac{dx}{dt} \right) + \frac{\partial}{\partial \dot{y}} \left( \frac{\partial U}{\partial x} \right) \left( \frac{dy}{dt} \right) + \frac{\partial}{\partial \dot{z}} \left( \frac{\partial U}{\partial x} \right) \left( \frac{dz}{dt} \right) \end{aligned} \quad (42)$$

Considering that  $U$  does not depend on velocities ( $\dot{x}$ ,  $\dot{y}$ ,  $\dot{z}$ ) and applying a similar method to find the derivatives with respect to  $y$  and  $z$ , we obtain:

$$\frac{\partial U}{\partial x} = \left( \frac{\partial^2 U}{\partial x^2} \right) x + \left( \frac{\partial^2 U}{\partial x \partial y} \right) y + \left( \frac{\partial^2 U}{\partial x \partial z} \right) z \quad (43)$$

$$\frac{\partial U}{\partial y} = \left( \frac{\partial^2 U}{\partial x \partial y} \right) x + \left( \frac{\partial^2 U}{\partial y^2} \right) y + \left( \frac{\partial^2 U}{\partial y \partial z} \right) z \quad (44)$$

$$\frac{\partial U}{\partial z} = \left( \frac{\partial^2 U}{\partial x \partial z} \right) x + \left( \frac{\partial^2 U}{\partial y \partial z} \right) y + \left( \frac{\partial^2 U}{\partial z^2} \right) z \quad (45)$$

The differential equations of motions (Eq.(18)) can be written as:

$$\begin{cases} \frac{d^2 x}{dt^2} - 2 \frac{dy}{dt} = \left( \frac{\partial^2 U}{\partial x^2} \right) x + \left( \frac{\partial^2 U}{\partial x \partial y} \right) y + \left( \frac{\partial^2 U}{\partial x \partial z} \right) z \\ \frac{d^2 y}{dt^2} + 2 \frac{dx}{dt} = \left( \frac{\partial^2 U}{\partial x \partial y} \right) x + \left( \frac{\partial^2 U}{\partial y^2} \right) y + \left( \frac{\partial^2 U}{\partial y \partial z} \right) z \\ \frac{d^2 z}{dt^2} = \left( \frac{\partial^2 U}{\partial x \partial z} \right) x + \left( \frac{\partial^2 U}{\partial y \partial z} \right) y + \left( \frac{\partial^2 U}{\partial z^2} \right) z \end{cases} \quad (46)$$

Here, the derivatives of the pseudo-potential components are given as:

$$\begin{aligned}
\frac{\partial^2 U}{\partial x^2} &= 1 - \frac{(1-\mu)}{r_1^3} - \frac{\mu}{r_2^3} + \frac{3(1-\mu)(x-\mu)^2}{r_1^5} + \frac{3\mu(x+1-\mu)^2}{r_2^5} \\
\frac{\partial^2 U}{\partial x \partial y} &= \frac{3(1-\mu)(x-\mu)y}{r_1^5} + \frac{3\mu(x+1-\mu)y}{r_2^5} \\
\frac{\partial^2 U}{\partial x \partial z} &= \frac{3(1-\mu)(x-\mu)z}{r_1^5} + \frac{3\mu(x+1-\mu)z}{r_2^5} \\
\frac{\partial^2 U}{\partial y^2} &= 1 - \frac{(1-\mu)}{r_1^3} - \frac{\mu}{r_2^3} + \frac{3(1-\mu)y^2}{r_1^5} + \frac{3\mu y^2}{r_2^5} \\
\frac{\partial^2 U}{\partial y \partial z} &= \frac{3(1-\mu)yz}{r_1^5} + \frac{3\mu yz}{r_2^5} \\
\frac{\partial^2 U}{\partial z^2} &= -\frac{(1-\mu)}{r_1^3} - \frac{\mu}{r_2^3} + \frac{3(1-\mu)z^2}{r_1^5} + \frac{3\mu z^2}{r_2^5}
\end{aligned}$$

This system of differential equations, as described in Eq.(46), can be represented in matrix form as:

$$\frac{d\mathbf{X}}{dt} = \frac{d}{dt} \begin{Bmatrix} x \\ y \\ z \\ \dot{x} \\ \dot{y} \\ \dot{z} \end{Bmatrix} = \begin{bmatrix} 0 & 0 & 0 & 1 & 0 & 0 \\ 0 & 0 & 0 & 0 & 1 & 0 \\ 0 & 0 & 0 & 0 & 0 & 1 \\ \left(\frac{\partial^2 U}{\partial x^2}\right) & \left(\frac{\partial^2 U}{\partial x \partial y}\right) & \left(\frac{\partial^2 U}{\partial x \partial z}\right) & 0 & 2 & 0 \\ \left(\frac{\partial^2 U}{\partial x \partial y}\right) & \left(\frac{\partial^2 U}{\partial y^2}\right) & \left(\frac{\partial^2 U}{\partial y \partial z}\right) & -2 & 0 & 0 \\ \left(\frac{\partial^2 U}{\partial x \partial z}\right) & \left(\frac{\partial^2 U}{\partial y \partial z}\right) & \left(\frac{\partial^2 U}{\partial z^2}\right) & 0 & 0 & 0 \end{bmatrix} \begin{Bmatrix} x \\ y \\ z \\ \dot{x} \\ \dot{y} \\ \dot{z} \end{Bmatrix} \quad (47)$$

In a more compact form:

$$\frac{d\mathbf{X}}{dt} = A(t)\mathbf{X} \quad (48)$$

The system in Eq. (48) represents a set of 36 coupled simultaneous differential equations. In order to solve them, we need initial conditions represented by the state vector  $\mathbf{X}_0$ . This way, the differential equations for the state-transition matrix become:

$$\frac{d\Phi(t, 0)}{dt} = A(t)\Phi(t, 0) \quad (49)$$

Solving Eq. (49) results in a set of 42 coupled simultaneous differential equations.

The state transition matrix is defined by a 6x6 ordinary differential equations (ODEs) matrix: this leads to a system of 36 ODEs. However, it's important to note that the ODE matrix is non-autonomous, meaning it depends on a specific solution or trajectory of the CR3BP. This trajectory is itself a solution of a separate system consisting of 6 ODEs. The two systems, the 6x6 ODE matrix and the trajectory ODEs, are solved concurrently, resulting in an autonomous system comprising 42 ODEs.

When the state-transition matrix is computed over one orbital period, it yields a specific STM referred to as the *monodromy matrix*. This matrix exhibits distinct characteristics, which are derived from Floquet Theory [37]. These characteristics are as follows:

- The monodromy matrix of a periodic orbit in the Circular Restricted Three-Body Problem must possess at least two eigenvalues equal to one.
- The monodromy matrix of an autonomous Hamiltonian system is symplectic. This means that it preserves the symplectic structure, which is a fundamental property of Hamiltonian systems.
- If  $\lambda$  is an eigenvalue of the monodromy matrix, then  $\lambda^{-1}$ ,  $\bar{\lambda}$  (complex conjugate) and  $\bar{\lambda}^{-1}$  are also eigenvalues of the matrix, and they have the same multiplicity. This property is a consequence of the symplectic nature of the monodromy matrix and is essential in understanding the stability and behavior of periodic orbits.

## 4.2 Differential Correction

As we have seen, there are various families of periodic CR3BP orbits, each representing a periodic solution to the EOMs (Eq.(18)) with distinct properties. For instance, we can consider the DROs, which lie in the xy-plane, or the Halo orbits, which exhibit symmetry with respect to the yz-plane.

In general, every orbit is characterized by a set of initial conditions, represented by the state vector  $\mathbf{X}$ , and a period T. Given that the types of orbits we've considered are periodic, the following condition holds:

$$\mathbf{X}_f = \mathbf{X}(T) = \mathbf{X}_0 \quad (50)$$

In Eq.(50), the subscript "f" denotes the state vector at the end of one period T, and the subscript "0" represents the state vector at the beginning. This equation embodies the concept of periodic orbits: with an initial state vector (initial conditions)  $\mathbf{X}_0$ , after a period T, the state vector  $\mathbf{X}_f$  will be identical to the initial one.

Expanding the EOMs of the CR3BP to the first order about  $(X_0, T)$  we get:

$$\delta\mathbf{X}_f = \Phi(0, T)\delta\mathbf{X}_0 + \frac{\partial\mathbf{X}_f}{\partial t}\delta T \quad (51)$$

where  $\Phi(0, T)$  is the state-transition matrix,  $\partial\mathbf{X}_f$  represents the incremental change that must be applied in each iteration and the initial state vector is of the form:

$$\mathbf{X}_0 = [x_0 \ y_0 \ z_0 \ \dot{x}_0 \ \dot{y}_0 \ \dot{z}_0] \quad (52)$$

If we consider a halo orbit, which is symmetric about the xz-plane, the initial conditions are:

$$\mathbf{X}_0 = [x_0 \ 0 \ z_0 \ 0 \ \dot{y}_0 \ 0] \quad (53)$$

In order to achieve a periodic orbit with a given z-amplitude, we need to determine the appropriate values for  $x_0$ , and  $\dot{y}_0$  through an iterative process. However, one challenge is that we do not initially know the period of the orbit,  $T$ .

To address this, we can utilize the principle of symmetry, which implies that we must have  $y_0 = 0$  and consequently,  $\delta y_0 = 0$ .

We can expand the third component of Equation (51) as follows:

$$\delta y = 0 = \Phi_{21}\delta x_0 + \Phi_{23}\delta z_0 + \Phi_{25}\delta \dot{y}_0 + \dot{y}_f\delta T \quad (54)$$

To find  $\delta T$ , we can rearrange this equation:

$$\delta T = -\frac{1}{\dot{y}_f}(\Phi_{21}\delta x_0 + \Phi_{23}\delta z_0 + \Phi_{25}\delta \dot{y}_0) \quad (55)$$

Given that  $z_0$  is fixed, we can calculate the incremental changes needed for  $x_0$  and  $\dot{y}_0$ :

$$\begin{Bmatrix} \delta x_0 \\ \delta \dot{y}_0 \end{Bmatrix} = \left[ \begin{bmatrix} \Phi_{41} & \Phi_{45} \\ \Phi_{61} & \Phi_{65} \end{bmatrix} - \frac{1}{\dot{y}_f} \begin{Bmatrix} \ddot{x}_f \\ \ddot{z}_f \end{Bmatrix} \begin{bmatrix} \Phi_{21} & \Phi_{25} \end{bmatrix} \right]^{-1} \begin{Bmatrix} \delta \dot{x}_f \\ \delta \dot{z}_f \end{Bmatrix} \quad (56)$$

Maintaining  $z_0$  fixed, the integration of the EOMs can be carried out while varying the period using Equation (55). Simultaneously, the values of  $x_0$  and  $\dot{y}_0$  can be updated using Equation (56). The objective is to continue this iterative process until the initial and final states differ by no more than a specified tolerance, typically around  $10^{-10}$ .

Algorithm 1 encompasses the essential steps for calculating the initial conditions (ICs) for orbits that exhibit symmetry in the  $xz$ -plane.

---

**Algorithm 1** Differential Correction for orbits in the  $xz$ -plane

---

```

Define initial guesses for ICs [ $x_0$  0  $z_0$  0  $\dot{y}_0$  0]
Set tolerance ( $tol$ )                                ▷ Define tolerance for convergence
while  $\dot{x} > tol$  and  $\dot{z} > tol$  do                    ▷ Iterate until desired accuracy is reached
  Integrate to  $n^{th}$  x-axis crossing                    ▷ Use Eq.(18)
  if at x-axis crossing  $\dot{x} < tol$  and  $\dot{z} < tol$  then ▷ Check if a periodic orbit is found
    Periodic Orbit found
  else if at x-axis crossing  $\dot{x} > tol$  or  $\dot{z} > tol$  then ▷ Non-periodic crossing
    Compute changes to ICs                            ▷ Use Eq.(56)
  end if
end while

```

---

For a DRO, using the fact that it is located in the  $xy$ -plane, we can set the  $z$ -component of both location and velocity to zero. In this case, by fixing the  $x$ -amplitude ( $x_0$ ), we have the opportunity to change the orthogonal velocity ( $\dot{y}_0$ ) and the period ( $T$ ) to compute the initial conditions that define this orbit family.

### 4.3 Poincaré Section

To consider an orbit as periodic, Eq.(51) must be satisfied. Each orbit can be assessed through a stability index, which gauges its ability to withstand external perturbations. One effective method for evaluating this stability is by employing Poincaré Maps, which are invaluable tools in celestial mechanics and dynamical systems theory because they provide insight into the long-term behavior of an orbit by examining a point that periodically crosses a reference plane or surface within the orbit.

The concept of periodicity is fundamental in this context. A truly periodic orbit, represented by  $\mathbf{X}^*$  in Figure 28, will cross the chosen plane  $P$  at the same point after each period  $T$ , demonstrating predictability and stability. In contrast, a generic orbit  $\mathbf{X}$  won't intersect the plane at the same point after a period  $T$ , leading to a distinctive final position, indicative of instability.

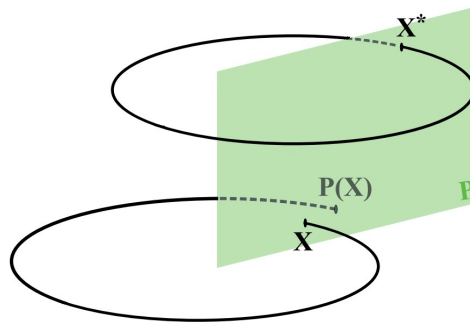


Figure 28: Poincaré Map

It's essential to note that the final point  $P(\mathbf{X})$  doesn't coincide with the initial point  $\mathbf{X}$ , underscoring the non-coincidence between these two points after a period  $T$ . This discrepancy in position between the initial and final points is a key characteristic used to determine whether an orbit is genuinely periodic or not.

By observing how the intersection point on the plane evolves over time, we can quantitatively assess the orbit's stability. If this point remains relatively close to the original intersection point, the orbit is considered stable. However, if the point's trajectory becomes erratic or deviates significantly from its initial position, the orbit is likely unstable.

Considering the plane  $P$ , this represents the Poincaré Map: a periodic orbit will be represented by a single point, while a non-periodic orbit will be represented by multiple intersection points in the plane. If we look at the state vector  $\mathbf{X}$ , it is repeated at intervals of time  $T$ . This process involves mapping the state vector onto itself. To achieve this, the monodromy matrix  $\Pi$  is used, which represents the state-transition matrix evaluated over a time interval of  $T$ .

The monodromy matrix (as presented in Sect. 4.1) is a  $6 \times 6$  matrix, containing six eigenvalues that determine the stability of the orbit:

- If at least one eigenvalue is greater than one, the orbit is considered unstable;

- If the largest eigenvalue is equal to 1, the orbit is considered neutrally stable.
- If all eigenvalues have a magnitude less than one, the orbit is considered stable.

This analysis is fundamental for understanding the long-term dynamics of the orbit in a given system [38].

#### 4.4 Invariant Manifolds

Using the eigenvalues ( $\lambda_i$ ) and eigenvectors ( $\mathbf{w}_i$ ) obtained from the monodromy matrix, it is possible to perturb an initial state vector  $\mathbf{X}_0$  of a periodic orbit by a small amount  $\epsilon$  in the direction of the stable (or unstable) eigenvectors.

$$\mathbf{X}_{perturbed} = \mathbf{X}_0 \pm \epsilon \mathbf{w} \quad (57)$$

Integrating the new state vector  $\mathbf{X}_{perturbed}$  forward or backward in time yields in trajectories that leave from or arrive at the periodic orbit whose initial condition  $\mathbf{X}_0$  was used [38].

By repeating this process for various values of  $\mathbf{X}_0$  within the orbit, a family of approximated asymptotic solution trajectories is obtained, that form a so-called invariant manifold tube in the phase space.

Algorithm 2 presents a pseudocode for calculating the invariant manifolds while some examples of stable and unstable invariant manifolds can be observed in Figures 29, 30, and 31.

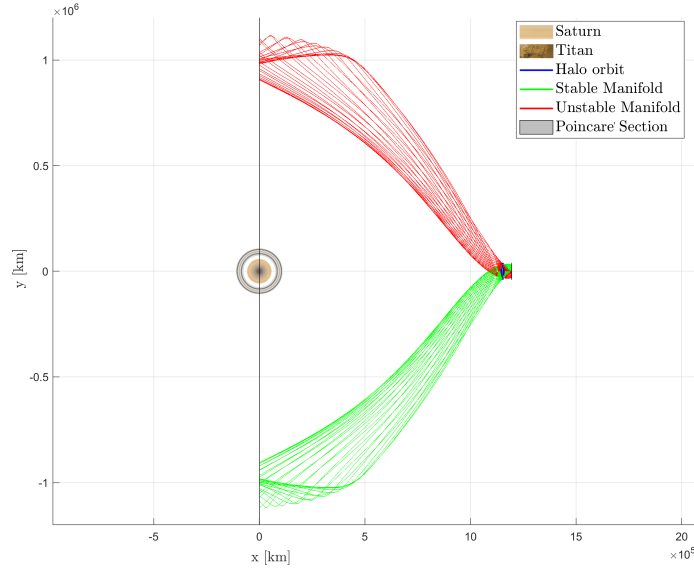


Figure 29: Stable and Unstable Manifolds of a halo orbit in the Saturn-Titan system ( $xy$  plane)

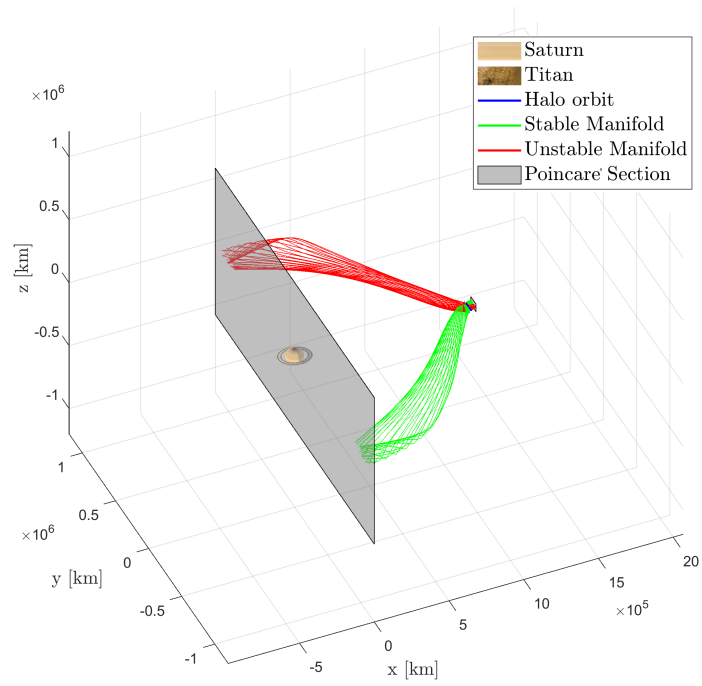


Figure 30: Stable and Unstable Manifolds of a halo orbit in the Saturn-Titan system

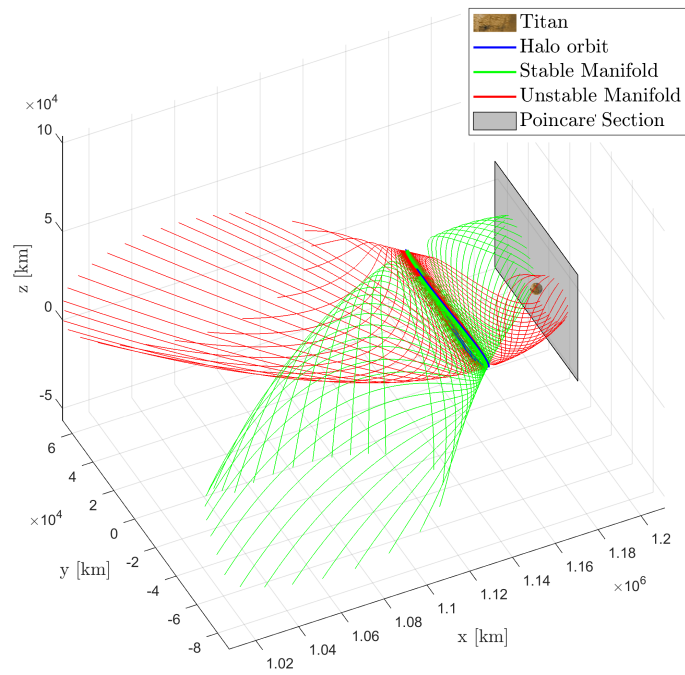


Figure 31: Stable and Unstable Manifolds of a halo orbit in the Saturn-Titan system. Focus on Titan

---

**Algorithm 2** Computation of Invariant Manifolds

---

Choose a periodic orbit in the CR3BP ▷ Define Initial Conditions  $\mathbf{X}_0$   
Compute the monodromy matrix ▷ Provides info about orbit stability  
Calculate the eigenvalues  $\lambda_i$  for  $i = 1, \dots, 6$   
**if** Real part of  $\lambda_i < 1$  **then**  
    Compute the stable invariant manifolds:  
    **for** Selected points along the orbit **do**  
        Define the eigenvector  $\mathbf{w}_i$  corresponding to the eigenvalue  $\lambda_i$   
        Define  $\epsilon = \textit{small}$   
        Perturb the initial conditions by the quantity  $\epsilon \mathbf{w}_i$  ▷  $\mathbf{X}_{pert} = \mathbf{X}_0 + \epsilon \mathbf{w}_i$   
        Solve the CR3BP Equations of Motion ▷ Equations (18)  
        **if** Integrate backward in time **then**  
            Obtain the stable invariant manifolds in the direction of Saturn  
        **else if** Integrate forward in time **then**  
            Obtain the stable invariant manifolds in the direction of Titan  
        **end if**  
    **end for**  
**end if**  
**if** Real part of  $\lambda_i > 1$  **then**  
    Compute the unstable invariant manifolds:  
    **for** Selected points along the orbit **do**  
        Define the eigenvector  $\mathbf{w}_i$  corresponding to the eigenvalue  $\lambda_i$   
        Define  $\epsilon = \textit{small}$   
        Perturb the initial conditions by the quantity  $\epsilon \mathbf{w}_i$  ▷  $\mathbf{X}_{pert} = \mathbf{X}_0 + \epsilon \mathbf{w}_i$   
        Solve the CR3BP Equations of Motion ▷ Equations (18)  
        **if** Integrate backward in time **then**  
            Obtain the unstable invariant manifolds in the direction of Titan  
        **else if** Integrate forward in time **then**  
            Obtain the unstable invariant manifolds in the direction of Saturn  
        **end if**  
    **end for**  
**end if**

---

Even distant from a periodic orbit, a spacecraft approaching a stable manifold will be drawn closer to the orbit and can be inserted into it with minimum  $\Delta V$ . Any spacecraft with arbitrary initial conditions cannot cross the surface of manifold tubes without executing an additional propulsive maneuver. In practical computations, numerical integrations are halted when the spacecraft reaches a predetermined Poincaré section. These computations also provide information about the time of flight.

In Figures 32 and 33, the Poincaré sections of Saturn and Titan can be observed, respectively. The invariant manifolds have been computed until they intersect the  $xy$  plane, which intersects both celestial bodies at their centers. By representing this surface, it becomes possible to assess where the invariant manifolds intersect it. In particular,

for the Poincaré Section of Titan, all trajectories that intersect the moon or are not at a distance greater than two times the radius of Titan have been excluded.

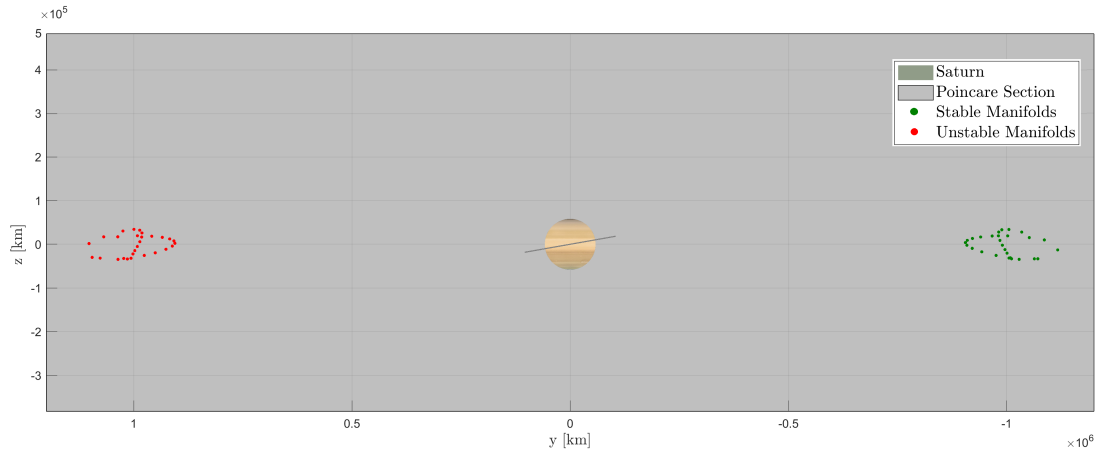


Figure 32: Poincaré Section on Saturn

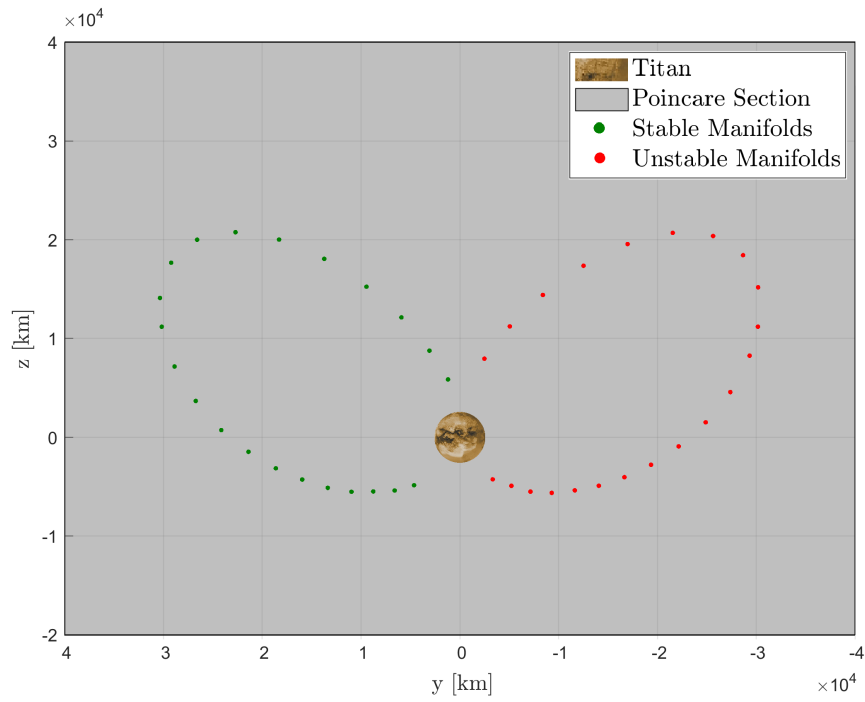


Figure 33: Poincaré Section on Titan

## 4.5 Employing Invariant Manifolds for Lyapunov Orbits

In Section 3.4, we delved into a thorough discussion and assessment of the orbit selection process, specifically focusing on orbits within the DRO family. The central challenge in this evaluation was to strike a balance between the orbit's stability and its scientific significance in terms of providing visibility of Titan's surface. DROs are distinctive for their quality of neutral stability. This implies that even if we introduce perturbations to the initial conditions, following the procedure outlined for assessing the invariant manifolds (in Section 4.4), it remains unfeasible to achieve these orbits.

The key approach to address this challenge involves using a Lyapunov orbit that intersects with the chosen DRO. This approach allows us to harness the invariant manifolds of the Lyapunov orbit, and subsequently, after reaching the Lyapunov orbit, perform a trajectory transition to the desired DRO using a  $\Delta V$  maneuver.

A Lyapunov orbit intersecting the chosen DRO has been defined. The intersection point serves as the location where a  $\Delta V$  maneuver is executed to transition from one orbit to the other. In Figure 34, you can observe both orbits and the maneuver point. The required  $\Delta V$  is equal to  $\Delta V = 0.169689802 km/s$

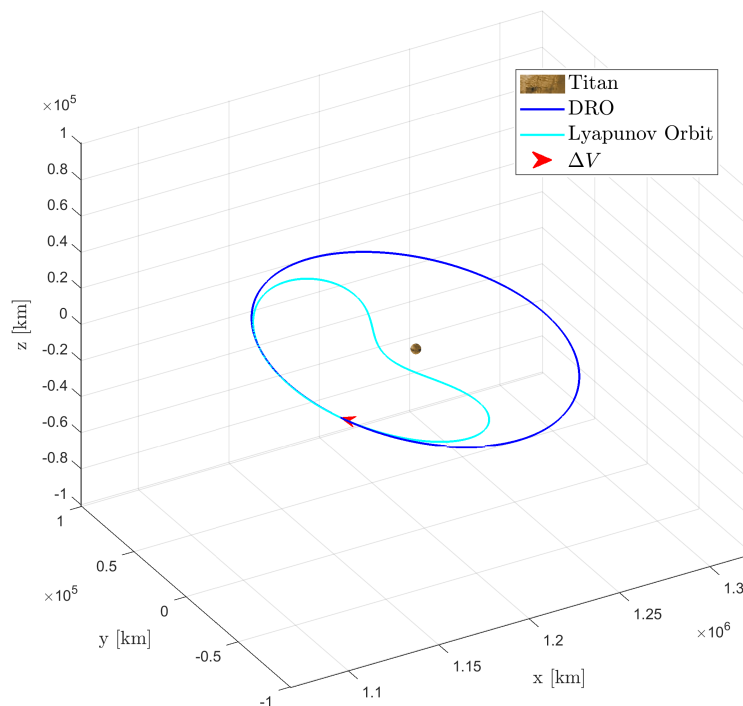


Figure 34: Intersection between the Lyapunov orbit and the DRO

Now that we have the  $\Delta V$  needed to move from the Lyapunov orbit to the DRO, we can move forward by exploring the evolution of the Lyapunov orbit's invariant manifolds.

Just as we did for the halo orbit in Section 4.4, in this instance, we compute the monodromy matrix for the orbit under consideration.

By assessing the eigenvalues of this orbit, the following results emerge:

$$\begin{aligned}
 \lambda_1 &= 3.32314047e + 02 \\
 \lambda_{2/3} &= 9.99999996e - 01 \pm 8.73339957e - 05i \\
 \lambda_4 &= 3.00920171e - 03 \\
 \lambda_{5/6} &= 9.59701284e - 01 \pm 2.81022143e - 01i
 \end{aligned}
 \tag{58}$$

Following algorithm 2, the eigenvector  $\mathbf{w}_1$  corresponding to the eigenvalue  $\lambda_1$  allows us to define the unstable invariant manifolds, while the eigenvector  $\mathbf{w}_4$  associated with the eigenvalue  $\lambda_4$  defines the stable invariant manifolds.

We can, therefore, define the quantity  $\epsilon \approx 30 \text{ km}$  to perturb the initial conditions  $\mathbf{X}_0$  of the orbit.

Let's consider the case of stable invariant manifolds:

$$\mathbf{X}_{pert} = \mathbf{X}_0 \pm \epsilon \mathbf{w}_4
 \tag{59}$$

By introducing a perturbation of approximately 30 kilometers to the initial conditions  $\mathbf{X}_0$  and integrating the CR3BP EOMs in Eq.(18) backward, we are exploring the stable invariant manifolds.

We can do the same by considering the eigenvector  $\mathbf{w}_1$  and integrating forward in time. This way, we obtain the unstable invariant manifolds.

The outcomes of these steps are presented in Figures 35, 36 and 37.

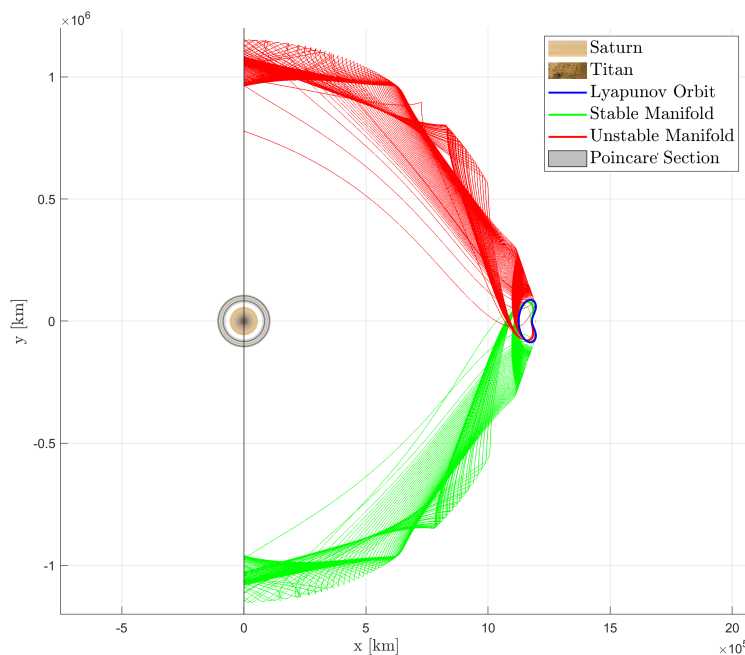


Figure 35: Stable and Unstable Manifolds of the Lyapunov orbit ( $xy$  plane)

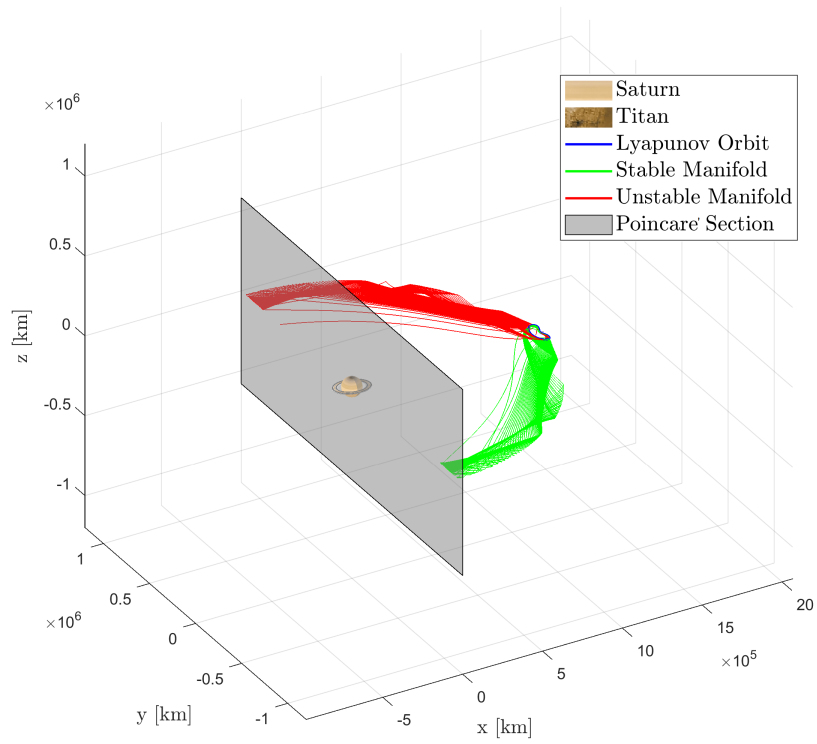


Figure 36: Stable and Unstable Manifolds of the Lyapunov orbit

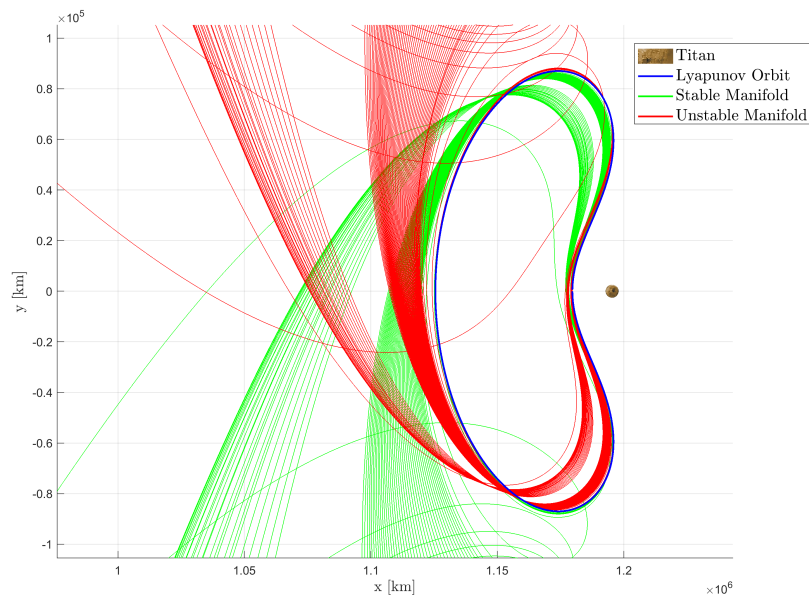


Figure 37: Stable and Unstable Manifolds of the Lyapunov orbit. Focus on Titan

The invariant manifolds encompass a range of trajectories, each with its stability characteristics. This diversity implies that transitioning between these trajectories will demand different  $\Delta V$  values, contingent not only on the chosen trajectory but also on the specific point within it. To address this variability, the Particle Swarm Optimization (PSO) algorithm emerges as a valuable tool. It facilitates the identification of parameter combinations that minimize  $\Delta V$ .

PSO's strength lies in efficiently navigating multidimensional parameter spaces. Its ability to explore and exploit the search space assists in pinpointing the optimal parameter set that minimizes  $\Delta V$  across various trajectories and their entry points. This optimization process becomes invaluable in celestial navigation, particularly in scenarios involving multiple trajectories. Minimizing  $\Delta V$  becomes pivotal here, significantly impacting mission efficiency and success.

## 5 Particle Swarm Optimization

Particle Swarm Optimization (PSO) is a computational technique that emulates the behavior of a swarm, such as a flock of birds searching for food, where each potential solution to a problem is represented as a particle. The swarm collectively explores the solution space by adjusting the positions of these particles based on their individual experiences and the shared knowledge of the entire swarm. Over iterations, the swarm is expected to gradually converge towards the optimal solution.

One notable advantage of PSO is its ability to function effectively without requiring a ‘good’ initial guess, which is typically unknown a priori and highly problem-dependent. PSO’s ability to operate effectively without prior knowledge makes it particularly valuable in interplanetary trajectory design and especially the CR3BP model, where precise initial estimations may be challenging to obtain. The swarm of particles in PSO collectively explores the solution space, utilizing their own experiences and the information shared within the swarm to guide their search. This cooperative exploration and exploitation of the solution space allow PSO to adapt and find optimal solutions even when the initial estimations are unknown.

PSO has proven to be a powerful and efficient technique in the interplanetary trajectory design. It provides a computational approach for exploring vast solution spaces and optimizing trajectories, as proven by Pontari and Conway [39] and Baraldi and Conte [28]. PSO allows mission planners to identify optimal paths and maneuver sequences for interplanetary orbit insertion into Saturn-Titan three-body orbits by iteratively adjusting candidate solutions based on their fitness.

The PSO algorithm has been effectively combined with other optimization algorithms, such as Differential Evolution (DE) or Genetic Algorithms (GA), to improve the overall performance of optimization processes [40] [41] [42]. By merging PSO with DE or GA, researchers seek to create hybrid algorithms that harness the benefits of both methods. PSO is known for its ability to efficiently explore the solution space and quickly converge towards promising solutions. On the other hand, DE and GA possess characteristics such as global search capability and robustness in handling complex and multi-modal optimization problems.

### 5.1 Description of the Method

The idea of applying PSO is to minimize a certain objective function related to a dynamic system during its temporal evolution.

In the case of constrained optimization problems, there are constraints expressed through inequalities that must be satisfied. The presence of inequalities reduces the search space of feasible solutions without reducing the degrees of freedom in the problem.

Let’s consider the objective function  $J$  that must be minimized. This function depends on the variables of the dynamic system, denoted as  $x_1, \dots, x_n$ , which are constrained within their respective ranges:

$$a_k \leq x_k \leq b_k \quad (k = 1, \dots, n) \quad (60)$$

In this context, the objective is to find values of  $x_1, \dots, x_n$  that minimize the objective function  $J$  while adhering to the constraints imposed by the system's dynamics. These constraints, expressed as inequalities, limit the feasible solutions within certain bounds. PSO can be used to explore and optimize within this constrained search space, searching for solutions that satisfy both the objective function and the imposed constraints.

PSO is a population-based method where the population is represented by a swarm of  $N_{par}$  particles. Each particle  $i$  ( $i = 1, \dots, N_{par}$ ) consists of  $k = 1, \dots, n$  components  $\chi_k$ , each of which is associated with a position  $x_k(i)$  and a velocity  $w_k(i)$ . It's important to note that the terms "position" and "velocity" are used in the context of the algorithm and do not have physical meanings. They are abstract representations that help govern the movement and interaction of particles within the PSO algorithm. For a particle  $i$ , the position vector  $\mathbf{x}(i)$  and the velocity vector  $\mathbf{w}(i)$  together represent the component  $\chi(i)$ .

The values of the problem's  $n$  variables are contained in the position vector:

$$x(i) \triangleq [x_1(i), \dots, x_n(i)]^T \quad (61)$$

whereas the position update is determined by the velocity vector. Given that the position is bounded, the corresponding velocity must also be restricted within suitable ranges:

$$-(b_k - a_k) \leq w_k \leq (b_k - a_k) \Rightarrow -d_k \leq w_k \leq d_k \quad (62)$$

with

$$d_k \triangleq b_k - a_k \quad (k = 1, \dots, n) \quad (63)$$

In the PSO algorithm, the position vector encodes the values of the variables, thus every particle's position vector serves as a representation of a potential solution while the velocity vector controls the rate and direction of change for these values.

To initiate the PSO algorithm, an initial population is generated randomly.  $N_{par}$  particles are introduced, and their positions and velocities are distributed randomly within the search space. This random distribution provides the initial conditions from which the particles will start exploring and optimizing the problem space. The iterative updates of positions and velocities allow the particles to collectively seek optimal solutions through their interactions and shared knowledge. In Figure 38 there is a scheme for the structure of the PSO algorithm.

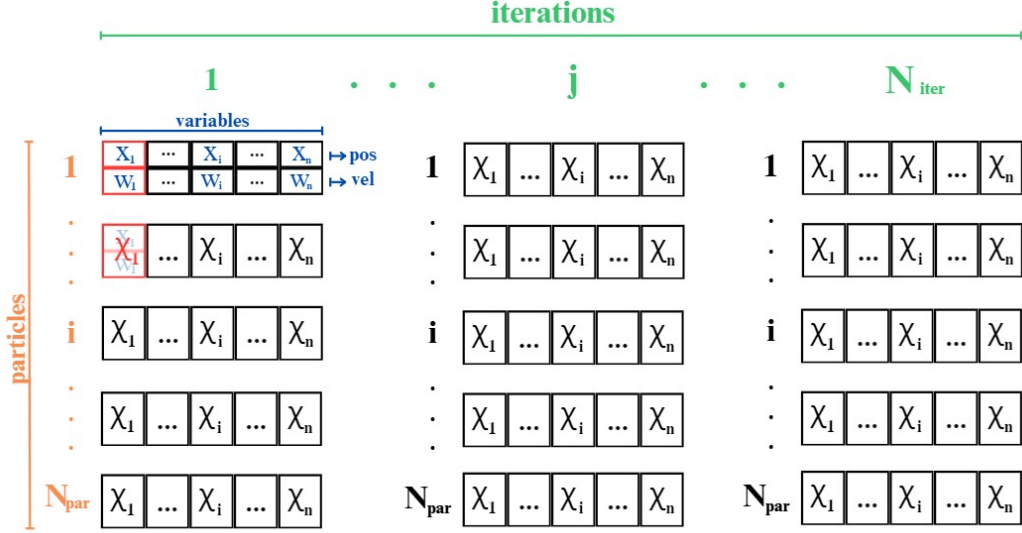


Figure 38: Structure of the PSO algorithm

For a generic  $j$  iteration:

1. For  $i=1, \dots, N_{par}$ 
  - (a) Evaluate the objective function for the  $i$ -th particle:  $J^j(i)$
  - (b) Define the best position visited by the  $i$ -th particle up to the current  $j$ -th iteration:

$$\Psi^j(i) = [x_1, \dots, x_k, \dots, x_n] \Big|_{\min\{J^p(i)\}} \quad (p = 1, \dots, j) \quad (64)$$

2. Define the global best position ever visited by the entire swarm up to the current  $j$ -th iteration:

$$\mathbf{Y}^j = [x_1, \dots, x_k, \dots, x_n] \Big|_{\min\{J_m^p\}} \quad (m = 1, \dots, N_{par}) \quad (65)$$

3. Update the velocity  $w$  for each particle  $i$  and each component  $\chi_k$ :

$$w_k^{j+1}(i) = C_I w_k^j(i) + C_C [\Psi_k^j(i) - x_k^j(i)] + C_S [Y_k^j - x_k^j(i)] \quad (66)$$

The *inertial*, *cognitive* and *social* weights have the following expressions [39]:

$$\begin{aligned} C_I &= (1 + r_1)/2 \\ C_C &= 1.49445r_2 \\ C_S &= 1.49445r_3 \end{aligned} \quad (67)$$

where  $r_1, r_2$  and  $r_3$  represent three independent random numbers between 0 and 1.

- (a) If  $w_k^{j+1}(i) < -d_k \Rightarrow w_k^{j+1}(i) = -d_k$
- (b) If  $w_k^{j+1}(i) > d_k \Rightarrow w_k^{j+1}(i) = d_k$

4. Update the position  $x$  for each particle  $i$  and each component  $\chi_k$ :

$$x_k^{j+1}(i) = x_k^j(i) + w_k^j(i) \quad (68)$$

- (a) If  $x_k^{j+1}(i) < a_k \Rightarrow x_k^{j+1}(i) = a_k$  and  $w_k^{j+1}(i) = 0$
- (b) If  $x_k^{j+1}(i) > b_k \Rightarrow x_k^{j+1}(i) = b_k$  and  $w_k^{j+1}(i) = 0$

The algorithm terminates when the objective function  $J$  reaches a certain tolerance or when the maximum number of iterations, denoted as  $N_{\text{iter}}$ , is reached. At the end, the vector  $\mathbf{Y}^{N_{\text{iter}}}$  will contain the optimal values of the unknown parameters that correspond to the minimum of the objective function  $J$ , denoted as  $J_{\text{opt}}^{N_{\text{iter}}}$ .

Whenever at least one inequality constraint is violated, the objective function of the  $i$ -th particle at the  $j$ -th iteration is set to  $\infty$ , and the velocity of the  $i$ -th particle for the  $(j+1)$ -th iteration is set to 0.

The distinctive feature of the algorithm can be found in the formula to update the velocity, as shown in Eq.66, which incorporates three stochastic terms:

- The first term,  $C_I$ , is referred to as the inertial term, and for each particle it is proportional to the particle's velocity in the previous iteration.
- The second term,  $C_C$ , represents the cognitive term and is proportionate to the distance between the current position of the particle and the best position the particle has achieved up to the  $j$ -th iteration.
- The third term,  $C_S$ , is the social term, and in this case, it is proportional to the difference between the current position of the particle and the best position encountered among all particles up to the  $j$ -th iteration.

Algorithm 3 illustrates a pseudo code for the PSO.

---

**Algorithm 3** Particle Swarm Optimization (PSO)

---

**Ensure:**  $J \leq \text{tolerance}$   
Initialize the particles  
 $j \leftarrow 0$   
**while**  $J \geq \text{tolerance}$  and  $j \leq N_{\text{iter}}$  **do**  
  **for**  $i = 1, \dots, N_{\text{par}}$  **do**  
    Evaluate  $J^j(i)$  ▷ Evaluate the objective function  
    Define  $\Psi^j(i)$  ▷ Best position visited by the particle  
  **end for**  
  Define  $\mathbf{Y}^j$  ▷ Global best position ever visited by the entire swarm  
  **for**  $i = 1, \dots, N_{\text{par}}$  **do**  
    **for**  $i = 1, \dots, n$  **do**  
      Update the velocity  $w_k^{j+1}(i)$  ▷ Update velocity  
      **if**  $w_k^{j+1}(i) > d_k$  **then**  
         $w_k^{j+1}(i) \leftarrow d_k$  ▷ Velocity bound check  
      **else if**  $w_k^{j+1}(i) < -d_k$  **then**  
         $w_k^{j+1}(i) \leftarrow -d_k$  ▷ Velocity bound check  
      **end if**  
      Update the position  $x_k^{j+1}(i)$  ▷ Update position  
      **if**  $x_k^{j+1}(i) < a_k$  **then**  
         $x_k^{j+1}(i) \leftarrow a_k$  ▷ Position bound check  
         $w_k^{j+1}(i) \leftarrow 0$  ▷ Velocity reset  
      **else if**  $x_k^{j+1}(i) > b_k$  **then**  
         $x_k^{j+1}(i) \leftarrow b_k$  ▷ Position bound check  
         $w_k^{j+1}(i) \leftarrow 0$  ▷ Velocity reset  
      **end if**  
    **end for**  
  **end for**  
   $j \leftarrow j + 1$   
**end while**

---

## 5.2 Application of PSO Algorithm for DRO's Initial Conditions

Algorithm 3 was utilized to compute the initial conditions for a DRO within the CR3BP in the Saturn-Titan system.

DROs are characterized by their initial conditions of the form:

$$\mathbf{X}_0 = [x_0 \ 0 \ 0 \ 0 \ \dot{y}_0 \ 0] \quad (69)$$

Our goal was to find initial conditions that would result in a DRO with a period of approximately 7 days.

By fixing the value of the period,  $T$ , we employed the PSO algorithm to determine two key parameters, namely,  $x_0$  and  $\dot{y}_0$ , such that:

$$\mathbf{X}_0 = \mathbf{X}_f = \mathbf{X}(T) \quad (70)$$

The structure of each particle  $P$  in the PSO was defined as follows:

$$P = [x_0 \ \dot{y}_0 \ \text{velocity} \ J \ J_{Best} \ P_{Best}] \quad (71)$$

We initialized a total of  $N_{par} = 6$  particles within the following bounds (in non-dimensional units):

$$\begin{cases} 1.0323 \leq x_0 \leq 1.0588 \\ -0.145 \leq \dot{y}_0 \leq -0.125 \end{cases} \quad (72)$$

The definition of these limits was based on the JPL Three-Body Periodic Orbit Catalog [31]. Two DROs in the Saturn-Titan system were considered, with periods of 5 and 9 days, with the aim of finding an intermediate one with a period of 7 days.

To control parameter variations, we also set limits on the velocity of the particles:

$$-1 \times 10^{-3} \leq \text{velocity} \leq +1 \times 10^{-3} \quad (73)$$

In this case, the objective function  $J$ , which needed to be minimized, was defined as:

$$J = \sqrt{x_0^2 + y_0^2} - \sqrt{x(T)^2 + y(T)^2} \quad (74)$$

Minimizing the function  $J$ , in this case, means ensuring that the initial point  $[x_0, y_0]$  and the final point  $[x(T), y(T)]$ , evaluated by integrating the EOMs over the period  $T$ , coincide.

We set a tolerance value of  $tol = 1e - 9$  and a maximum number of iterations as  $N_{iter} = 160$ . Additionally, an optimal combination of inertial, cognitive, and social coefficients was determined through a trial-and-error approach:

$$\begin{cases} CI = 0.7; \\ CC = 1.2 * rand(0, 1); \\ CS = 1.4995 * rand(0, 1); \end{cases} \quad (75)$$

To speed up convergence, an extra  $J_{Best}$  control mechanism was implemented: if the  $J_{Best}$  function remained constant for at least five iterations, the "worse" (farthest from the  $J_{Best}$  positions) half of the particles was randomly reinitialized close to the global best positions. The results of the PSO algorithm are depicted in Figure 39. For more detailed visual insights into the PSO algorithm's performance, you can watch the accompanying video, available at [this link](#)<sup>2</sup>.

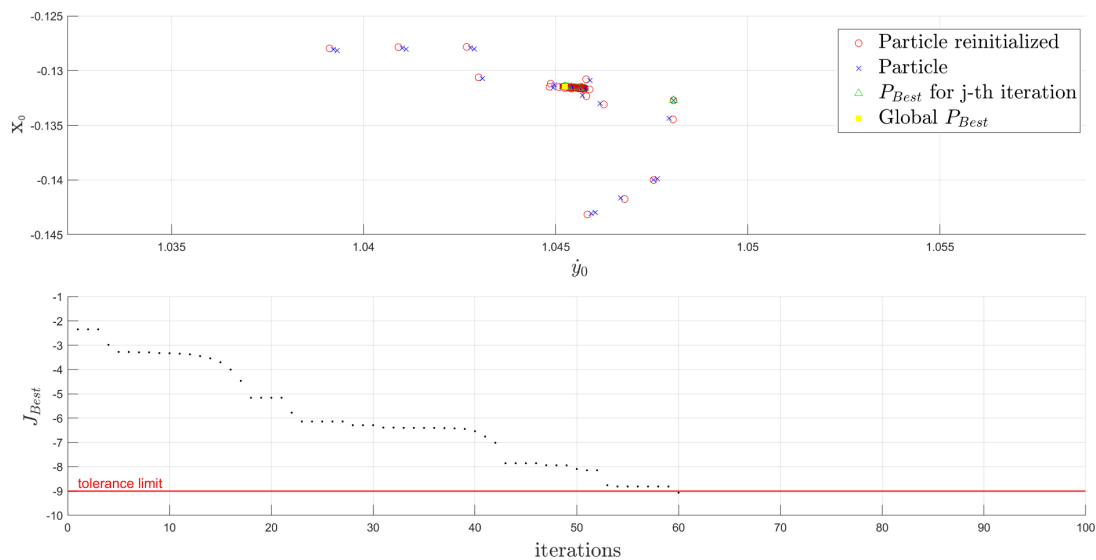


Figure 39: Particles variations and convergence. Video available [here](#)<sup>2</sup>

This figure showcases the trajectories of the particles at each iteration as they converge toward the solution. The lower part of the figure illustrates the variation in  $J_{Best}$  at each iteration. The algorithm reaches convergence after 60 iterations, at which point it achieves a  $J_{Best}$  value of  $6.2364e-10$ . The yellow square represents the optimal positions for both the variables  $x_0$  and  $\dot{y}_0$ . Finally, Figure 40 presents the DRO obtained through the application of the PSO algorithm. The initial conditions found are as follows:

$$\mathbf{X}_0 = [1.0452400216 \ 0 \ 0 \ 0 \ -0.1314618083 \ 0] \quad (76)$$

<sup>2</sup><https://youtu.be/qvHt4nfxZEc>

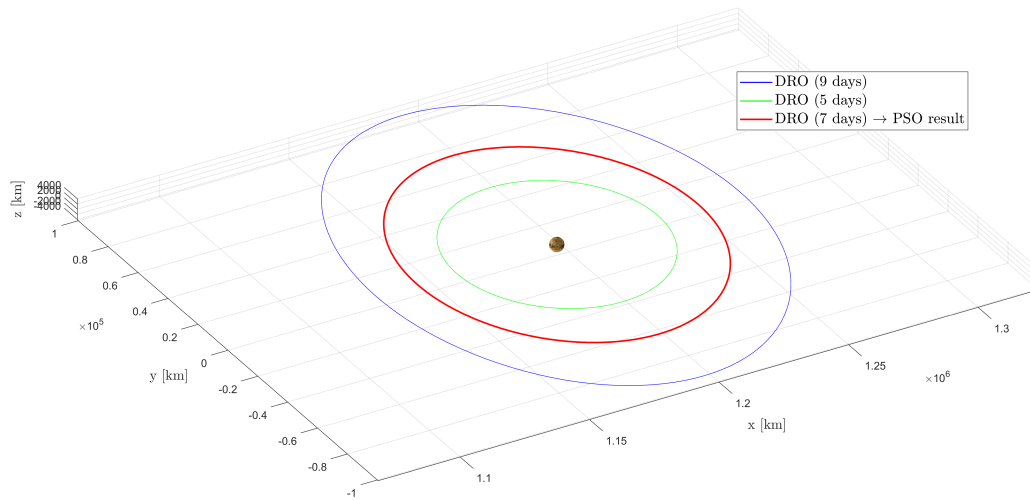


Figure 40: DRO obtained using the PSO algorithm

## 6 Trajectory Optimization

In previous chapters, fundamental concepts related to Dynamical Systems Theory and the Particle Swarm Optimization algorithm were introduced. These will play a crucial role in the development of this chapter.

This chapter focuses on optimizing trajectories to achieve insertion into the Distant Retrograde Orbit chosen in Chapter 3, while minimizing  $\Delta V$ .

As highlighted when discussing invariant manifolds (Section 4.4), the trajectories, whether stable or unstable, are numerous. Consequently, the  $\Delta V$  required to transition into these varies.

Hence, the objective here is to fine-tune trajectory optimization methods to precisely insert into the specified DRO while minimizing the energy expenditure associated with  $\Delta V$ . The diverse nature of trajectories, both stable and unstable, underscores the importance of a meticulous optimization process to identify the most efficient path. This involves considering various parameters and characteristics of the system to ascertain the optimal trajectory and entry point into the desired orbit.

### 6.1 Interplanetary Arrival

In this thesis, our central focus revolves around optimizing trajectories leading to Titan, utilizing Saturn's sphere of influence as our initial reference point for the optimization process.

Hajdik and Ramsey et al. [43] conducted a comprehensive study employing advanced software tools and custom scripts. Their work involved incorporating an aerogravity assist at Titan to enable a strategic exploration of Saturn's moon Enceladus from a meticulously chosen orbit. Additionally, Gajeri [44] contributed significantly to this field by analyzing trajectories for a robotic mission to Titan. His research emphasized the advantages of the Direct Fusion Drive (DFD) propulsion system, highlighting evolving technologies that can impact interplanetary missions.

Another noteworthy effort is the Dragonfly mission, meticulously designed by McQuaide et al. [45]. This mission aims to conduct a comprehensive scientific survey of Titan using a relocatable lander. Particularly intriguing is the high-energy  $\Delta V$  Earth Gravity Assist ( $\Delta V$ -EGA3+) trajectory involved, which includes intricate deep space maneuvers, an Earth gravity assist, and a series of trajectory correction maneuvers.

It's important to note that the findings of these esteemed researchers offer valuable insights and methodologies for achieving trajectory optimizations. These insights serve as a foundational starting point to reach Titan while minimizing  $\Delta V$  requirements.

We will consider the arrival at Saturn's sphere of influence (SOI) with a hyperbolic excess velocity of  $v_\infty = 5.9177$  km/s, as provided by [43]. Examples of the hyperbolic trajectory design in the inertial reference frame can be observed in Figures 41 and 42.

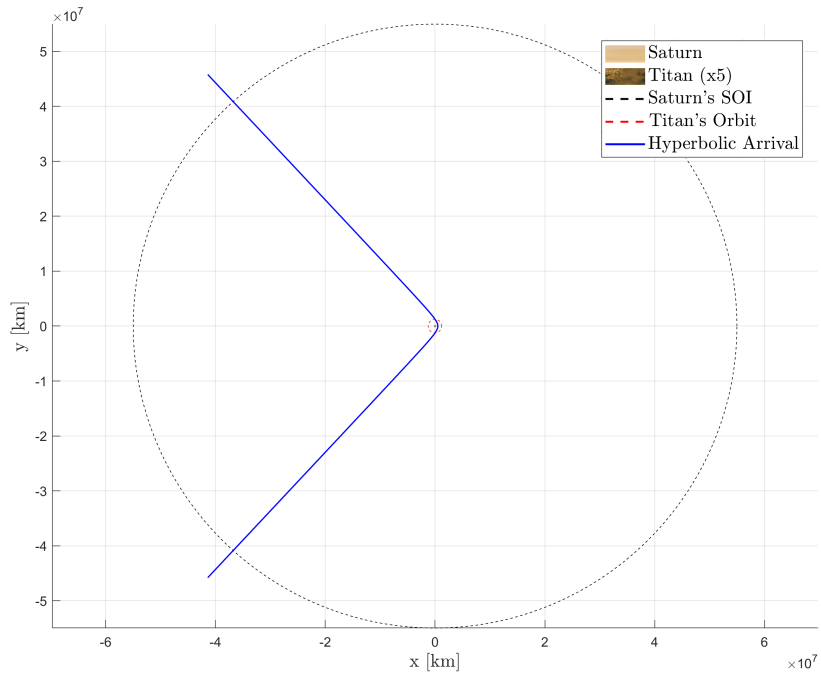


Figure 41: Hyperbolic Arrival

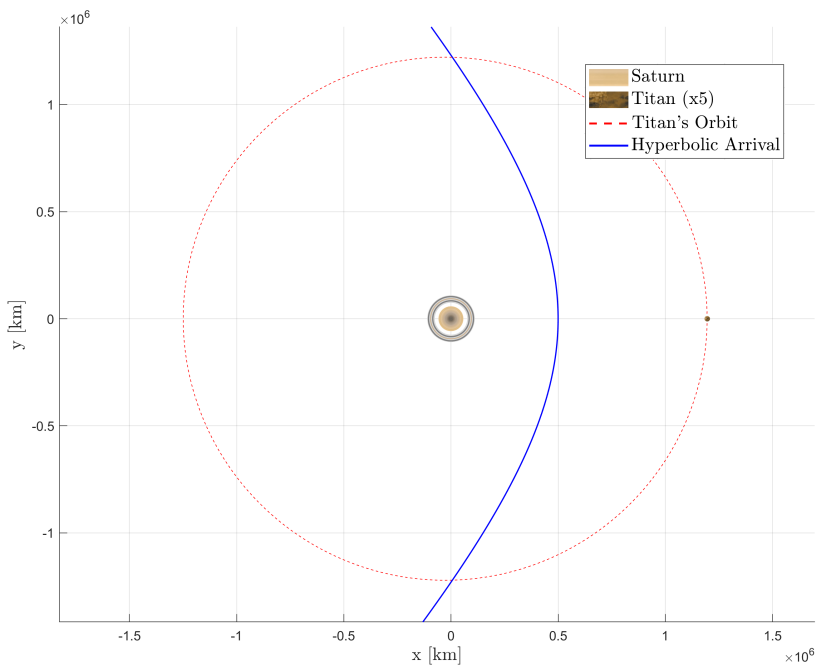


Figure 42: Hyperbolic Arrival. Focus on Saturn-Titan system

## 6.2 Direct Arrival to Titan

Arriving directly onto Titan through a hyperbolic trajectory involves complex calculations and considerations due to the dynamics of the Saturn-Titan system. This approach necessitates a spacecraft to enter Titan's orbit with a velocity exceeding its escape velocity, utilizing the moon's gravitational pull to decelerate effectively.

Synchronizing the spacecraft's trajectory with Titan's orbit is crucial for a successful encounter, considering Saturn's gravitational effects, Titan's elliptical orbit, and changes in its orbital speed.

However, the most crucial aspect is that this maneuver requires more  $\Delta V$  than any other. Achieving such a trajectory demands a significant amount of propulsion power, making it a challenging yet vital aspect of mission planning.

While challenging, the calculations and insights gained from planning such a mission will serve as valuable benchmarks for evaluating and contrasting alternative approaches for reaching Titan, providing invaluable data for future deep-space missions.

The plan involves leveraging the hyperbolic excess of velocity provided by [43] to set up our calculations. The concept is to construct the arrival hyperbola so that it has its periapsis at a point along Titan's trajectory. This would enable the spacecraft to reach Titan's sphere of influence. The Figure 43 depicts the scenario just described in the simplest possible case.

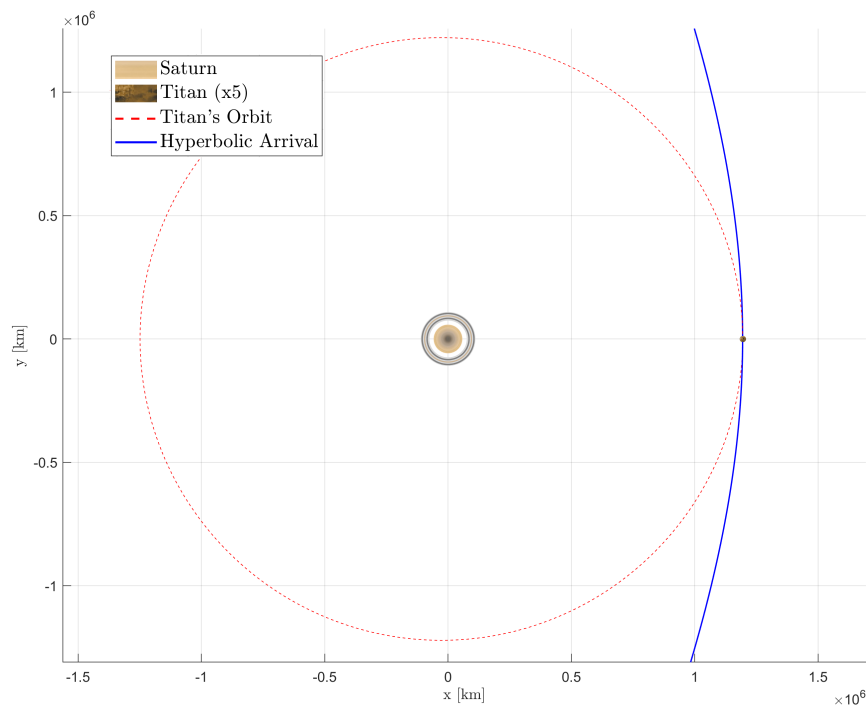


Figure 43: Direct Hyperbolic Arrival to Titan

Once the spacecraft reaches Titan’s SOI, the goal is to circularize the orbit: by slowing down the spacecraft, it becomes possible to establish a circular orbit around Titan. It’s essential to note that by transitioning from the three-body problem to this approach, we’re essentially simplifying it into a two-body problem. After reaching Titan’s sphere of influence, we no longer consider gravitational attraction and perturbations caused by Saturn in the system.

The circular orbit is designed to intersect the chosen Lyapunov orbit. This way, a  $\Delta V_1$  maneuver can place the spacecraft into the circular orbit and subsequently, with a  $\Delta V_2$  maneuver, into the Lyapunov orbit. The further transition from Lyapunov to the DRO chosen is described in Section 4.5. The scenario is shown in Figure 44. In this figure, depicted within the Inertial Reference Frame (IRF), the orbits in the Rotational Reference Frame (RRF) have also been plotted.

The use of the RRF simplifies the visualization, providing a clearer understanding of the dynamics involved in these orbits in relation to Titan. Additionally, the distinct methodologies used in calculating these orbits - one involving the complex gravitational interactions in the CR3BP and the other simplifying it to the 2BP - highlight different modeling approaches for orbital analysis in celestial mechanics.

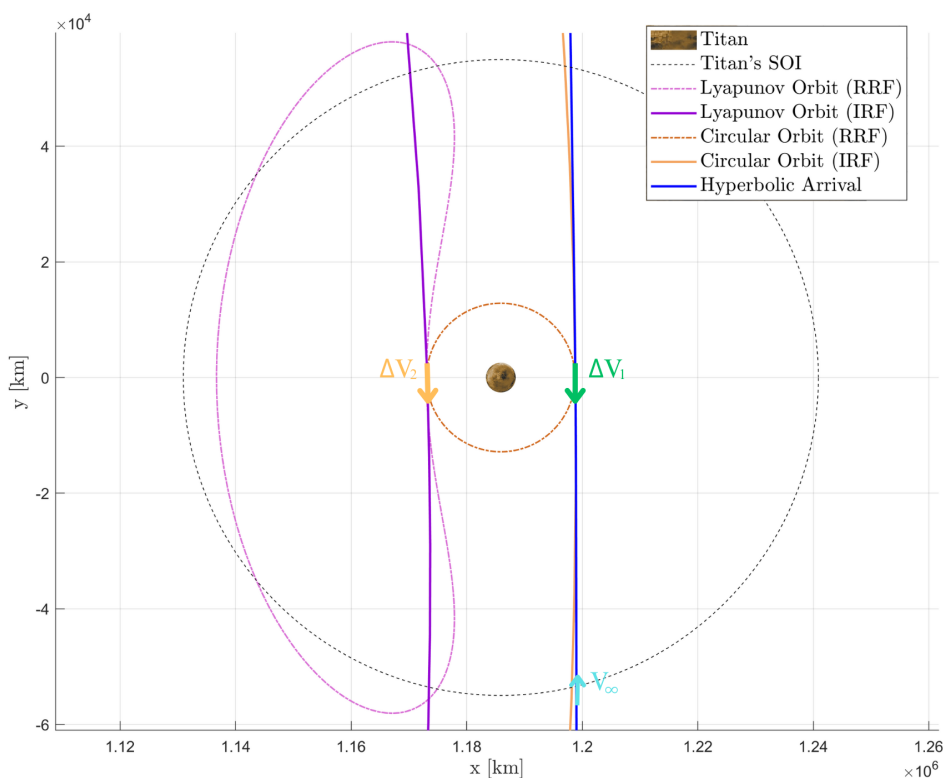


Figure 44: Direct Hyperbolic Arrival to Titan: Titan’s SOI

At the hyperbolic periapsis, a  $\Delta V_1 = 9.2296$  km/s is needed to circularize the orbit at an altitude of  $h = 13,217$  km from Titan's surface. Once in the circular orbit, only half of the orbital path is traversed before reaching the intersection with the Lyapunov orbit. At this intersection, an additional  $\Delta V_2 = 0.2557$  km/s maneuver facilitates the transition to the Lyapunov orbit. The spacecraft doesn't spend much time in the circular orbit as it serves as a stepping stone for the subsequent intersection with the Lyapunov orbit. This scenario proves useful when we seek comparative terms for the following scenarios.

Consequently, a total  $\Delta V_{TOT} = \Delta V_1 + \Delta V_2 = 9.4853$  km/s would be needed for a direct arrival at Titan.

### 6.3 Direct Arrival to the Lyapunov Orbit

Looking at Figure 44, one might consider bypassing the orbital circularization and entering the Lyapunov orbit by arranging the hyperbolic arrival to intersect the Lyapunov orbit directly.

However, it's crucial to consider that Lyapunov orbits, much like DROs, are indeed retrograde orbits. This implies that if the hyperbola were to intersect the Lyapunov orbit at the point closest to Titan (point 2), a significant  $\Delta V$  would be required to transition to the Lyapunov orbit. This is because not only the spacecraft would need to decelerate, but its velocity would need a complete reversal. The challenge arises because retrograde orbits move in the opposite direction of the body's rotation. Essentially, the spacecraft needs to negate its initial velocity and then establish a new velocity vector in the opposite direction, aligning with the retrograde orbit.

To reduce the required  $\Delta V$  for such a maneuver, considering an intersection between the hyperbolic periapsis and the Lyapunov orbit at the point farthest from Titan within the Lyapunov orbit (point 1) could indeed minimize the necessary change in velocity. In this scenario, the velocities of the hyperbola and the Lyapunov orbit align, allowing for a reduction in the  $\Delta V$  required. This particular scenario is depicted in Figure 45.

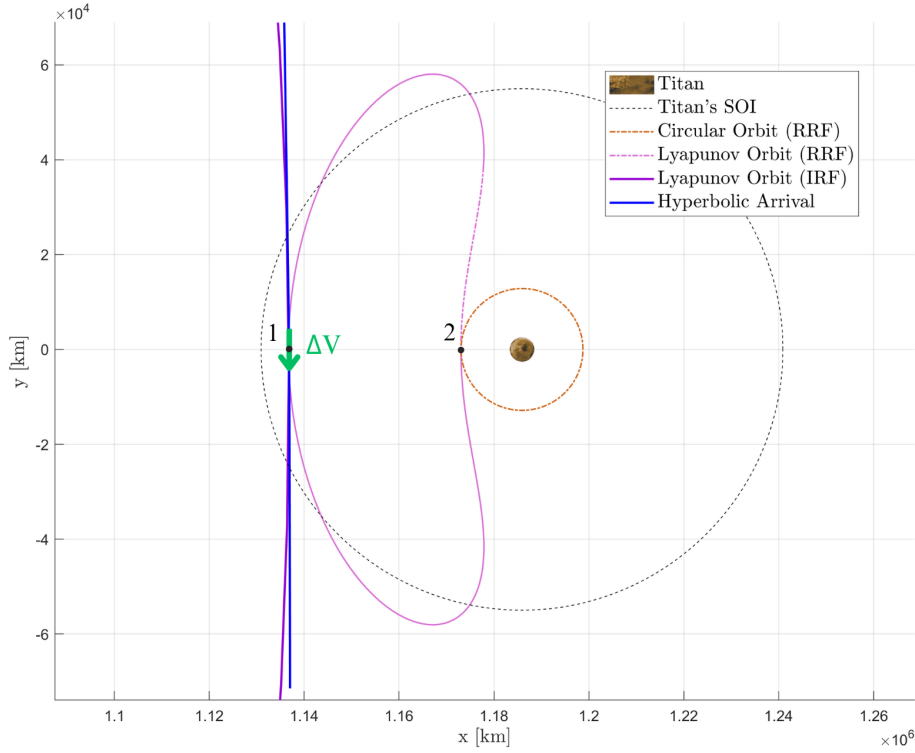


Figure 45: Direct Hyperbolic Arrival to Lyapunov Orbit

The  $\Delta V$  required in this case amounts to  $\Delta V = 9.6413 \text{ km/s}$ .

This strategy aims to take advantage of the alignment of velocities, reducing the overall energy needed to transition from the hyperbolic trajectory to the retrograde Lyapunov orbit. By choosing an intersection point farther from Titan within the Lyapunov orbit, the spacecraft can benefit from a velocity match, requiring a lesser change in velocity to synchronize with the retrograde orbit.

However, it's crucial to note that even though this approach appears to reduce the required  $\Delta V$  for this scenario, executing such a precise maneuver in space demands accurate calculations, precise timing, and fine control of the spacecraft's propulsion systems. Furthermore, other factors like gravitational influences from nearby celestial bodies and potential perturbations need consideration to ensure a successful and efficient trajectory adjustment.

If we consider the scenario of a direct arrival at Titan, as described in Section 6.2, the circularization of the orbit and subsequent insertion into the Lyapunov orbit allow for a savings of approximately  $\Delta V = 0.156 \text{ km/s}$  compared to the case just described. This is because the intersection point between the Lyapunov orbit and the hyperbola lies farther away from Titan. Essentially, at that point, the spacecraft moves more slowly compared to the point discussed in the Section 6.2. This implies a greater need to decelerate the spacecraft significantly.

## 6.4 Hyperbolic Arrival in Invariant Manifolds

A new approach introduced in this section involves leveraging invariant manifolds. It has been observed that these manifolds represent a set of trajectories obtained by perturbing the periodic orbit of the CR3BP. The concept is to utilize stable invariant manifolds: once the spacecraft reaches such a manifold, it follows the trajectory to its destination without the need for propellant consumption, eliminating the necessity of implementing maneuvers.

The strategy involves entering Saturn’s sphere of influence via the hyperbolic arrival trajectory and then providing a  $\Delta V$  to transition to the invariant manifold that will asymptotically carry the spacecraft toward the Lyapunov orbit and from there to the DRO.

The spacecraft reaches Saturn’s sphere of influence with a  $v_\infty$  of 5.9177 km/s, as calculated by [43]. It continues along the hyperbolic trajectory, intersecting the invariant manifolds, enabling the transition to the subsequent trajectory.

It’s important to note that when referring to stable invariant manifolds, we’re discussing a set of trajectories stemming from points on the Lyapunov orbit which were propagated backwards in time until they intersected the arrival hyperbolic trajectory. This leads to different trajectories that will require different  $\Delta V$ s.

For a more precise estimation of the required  $\Delta V$  for this maneuver, the relative positions of Titan and Saturn were determined using the JPL Horizons System<sup>3</sup>, a JPL-provided software for celestial bodies’ ephemerides. This became feasible because the work by Hajdik et al. [43] not only provides the hyperbolic excess velocity but also the dates.

A simulated mission was planned for launch on December 11<sup>th</sup>, 2036, aiming to reach the Saturn system by July 2<sup>nd</sup>, 2043. The notation  $\Delta V$ -EGA3 denotes the use of a Deep Space Maneuver (DSM) during the initial phase of the mission. This maneuver alters the spacecraft’s energy, shifting the Earth re-encounter time to a post-perihelion position. Additionally, the ‘EGA3’ indicator signifies an Earth Gravity Assist performed slightly over 3 years after launch, strategically executed following the cruise stage’s passage beyond perihelion [43].

Utilizing the arrival date allowed consideration of the relative position of the two celestial bodies. Particularly, the time of flight along the hyperbolic trajectory to the periapsis was calculated solving the Kepler’s equation: it amounts to a journey of approximately 100 days, enabling us to define the relative position between Saturn and Titan on October 10<sup>th</sup>, 2043. The scenario is shown in Figure 46 in the rotating reference frame.

---

<sup>3</sup>JPL Horizons: <https://ssd.jpl.nasa.gov/horizons>

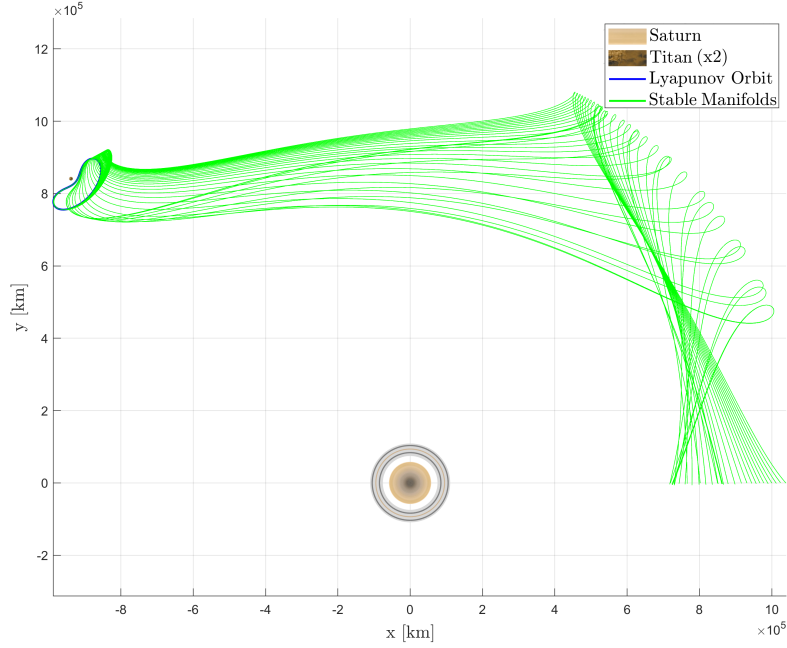


Figure 46: Invariant Manifolds in the Saturn-Titan system on October 10th, 2043

At this point, constructing the arrival hyperbola involves considering Saturn as the focus and utilizing the known  $v_\infty$  to derive specific orbital parameters of the hyperbola. It's important to note that to completely define the hyperbola, specifying a periapsis is essential. From several analyses conducted aiming to intersect the hyperbolic trajectory and the invariant manifolds, we obtained a periapsis positioned at  $r_p = 4 \times 10^6$  km from Saturn's surface.

The major semi-axis  $a$  can be defined as:

$$a = -\frac{\mu_{\tilde{h}}}{v_\infty^2} = -1.0834 \times 10^6 \text{ km} \quad (77)$$

where  $\mu_{\tilde{h}} = 37940584.842 \text{ km}^3/\text{s}^2$  represents Saturn's gravitational parameter<sup>4</sup>.

Furthermore, calculating the eccentricity of the hyperbola yields:

$$e = 1 + \frac{r_p v_\infty^2}{\mu_{\tilde{h}}} = 4.6920 \quad (78)$$

As mentioned earlier, the hyperbola intersects several invariant manifolds. However, the required  $\Delta V$  for a maneuver is in the range of  $\Delta V \approx 8 \text{ km/s}$ . This arises because the intersection between a generic trajectory of the invariant manifold and the hyperbola occurs in the vicinity of periapsis.

<sup>4</sup> $\tilde{h}$  denotes Saturn's astronomical symbol

Applying the vis-viva equation:

$$E = \frac{v_{\infty}^2}{2} = \frac{v^2}{2} - \frac{\mu_h}{r_p} \quad (79)$$

It's evident that as we approach periapsis, the velocity along the hyperbolic trajectory increases. Therefore, generally, a substantial  $\Delta V$  will be required to decelerate and align the spacecraft's velocity with the invariant manifold.

To address this challenge, a new approach divides the maneuver into two  $\Delta V$  maneuvers. As the spacecraft approaches Saturn along the hyperbolic trajectory, a  $\Delta V_1$  will be applied to divert it from the hyperbolic path, followed by a subsequent  $\Delta V_2$  for insertion into the invariant manifold.

By applying the initial  $\Delta V_1$ , a portion of the spacecraft's kinetic energy along the hyperbola is decreased. This allows for reducing the spacecraft's velocity, enabling interception of the invariant manifold with a lower velocity. Consequently, a lower  $\Delta V_2$  is required compared to direct intersection from the hyperbola.

### PSO Structure

The application of the PSO Algorithm 3 aims to evaluate the combination of maneuvers that minimize  $\Delta V_{TOT} = \Delta V_1 + \Delta V_2$ , where  $\Delta V_1$  represents the initial maneuver to depart from the arrival hyperbola, and  $\Delta V_2$  represents the insertion maneuver into one of the trajectories enclosed in the stable invariant manifold.

Three specific parameters are used to compute the propellant-optimal trajectory:

1. The position on the arrival hyperbolic trajectory where the first maneuver described by  $\Delta V_1$  will occur. This parameter will be evaluated based on the angle  $\delta$  between Saturn and the considered point of the hyperbola;
2. The  $\Delta V_1$ , indicating the retrograde change of velocity required;
3. The  $i$ -th trajectory of the invariant manifold, hence the velocity required for the spacecraft to enter that trajectory. Indirectly, this parameter provides  $\Delta V_2$ .

By combining these three parameters with the PSO framework, the algorithm aims to converge towards the solution that minimizes  $\Delta V_{TOT}$ .

Figure 47 depicts the structure of the PSO, emphasizing the three randomly chosen parameters that impact the spacecraft trajectory. One parameter that could have been considered is the time of flight (TOF). However, in this instance, we opted not to include it due to the inherently lengthy duration of the robotic mission already taking several years to reach the SOI of Saturn.

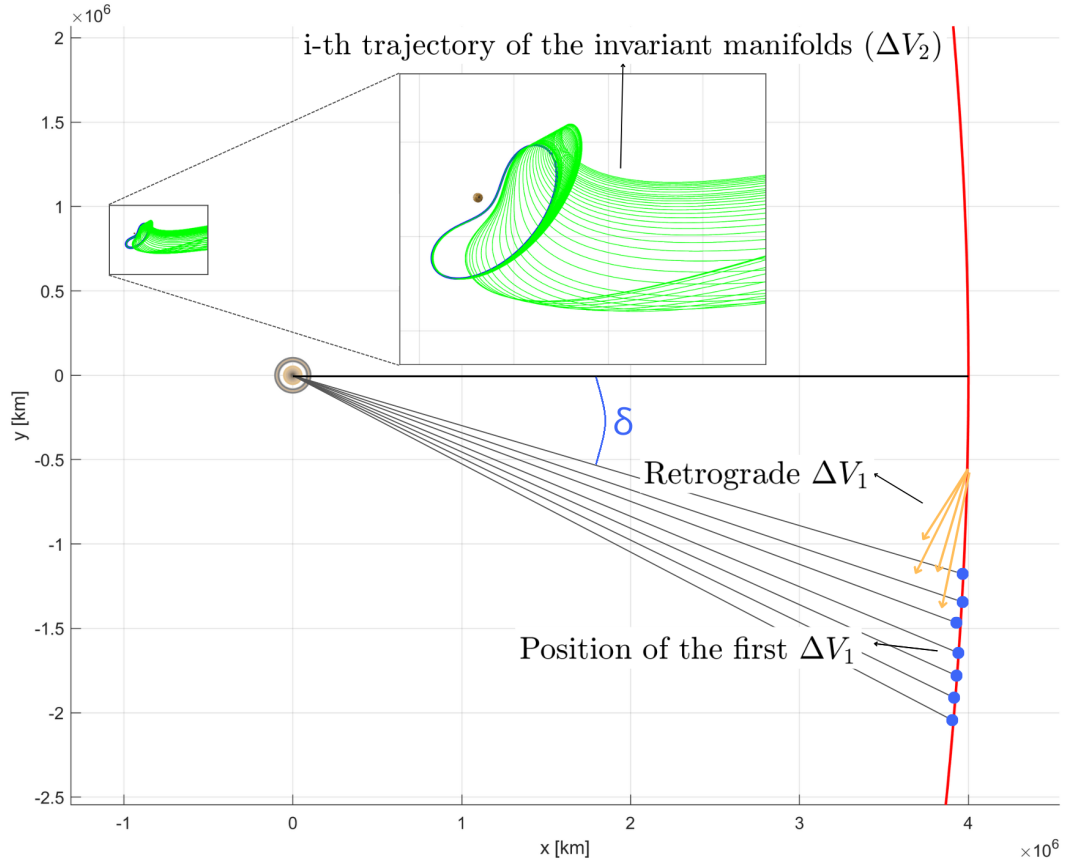


Figure 47: Variables of the PSO Algorithm

The algorithm involves creating  $N_{par} = 5$  particles, each containing a randomly generated value for the point where the first maneuver, described by  $\Delta V_1$ , takes place, the magnitude of  $\Delta V_1$ , and a generic  $i$ -th trajectory of the invariant manifolds. Specific limits are defined for generating these values:

- For the position where the first retrograde  $\Delta V_1$  occurs, all points on the arrival hyperbola between  $\delta = 45^\circ$  and  $\delta = 90^\circ$  from the  $x$ -axis are considered. In terms of distance from Saturn, the boundaries are defined as  $9.6436 \times 10^6 \leq R_p \leq 1.8443 \times 10^7$ .
- The retrograde  $\Delta V_1$  values are considered within the range of 0.1 km/s to 5 km/s.
- For the  $i$ -th trajectory of the invariant manifold, values of  $i$  between 1 and 320 are considered, encompassing all points in which the Lyapunov orbit has been discretized.

The maximum number of iterations,  $N_{iter}$ , has been set at 30 iterations, as the algorithm typically converges within this limit.

The application of the PSO along with its outcomes is depicted in Figure 48. A video is available at [this link](#)<sup>5</sup>.

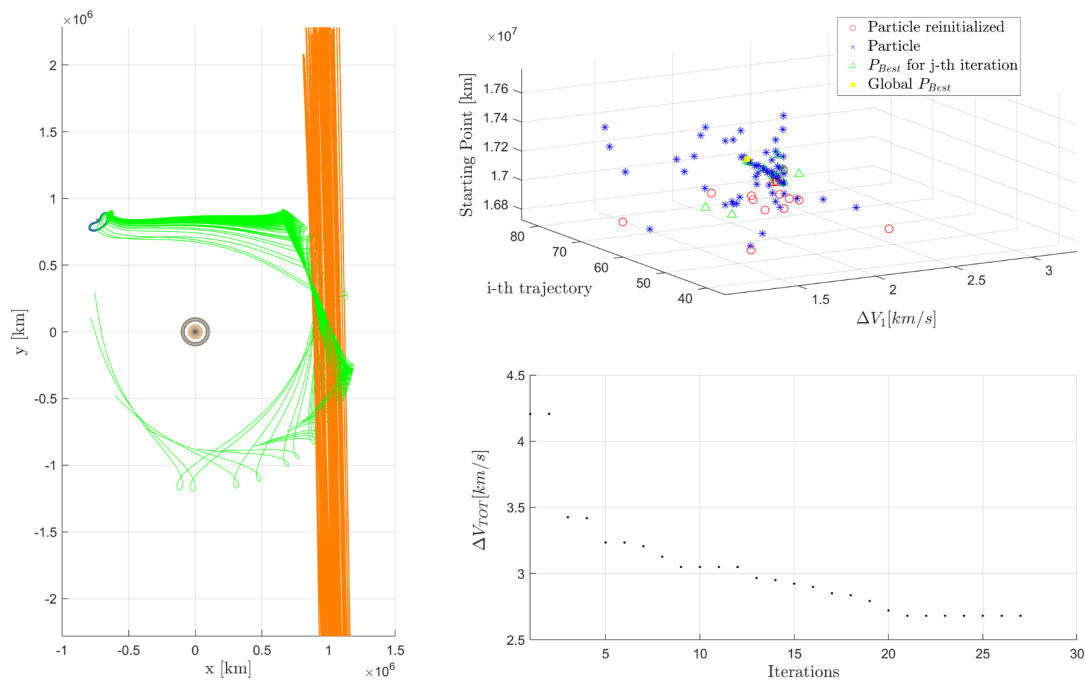


Figure 48: PSO algorithm results. Video available [here](#)<sup>5</sup>

In Figure 48, three graphs are presented:

1. The left graph displays all trajectories—both hyperbolic and invariant manifolds—that the PSO analyzed to seek the one minimizing the  $\Delta V_{TOT}$ .
2. The top-right graph illustrates the evaluated particles: red circles (o) denote initialized or reinitialized particles when they are significantly distant from the global minimum of  $\Delta V_{TOT}$  at a given iteration, blue asterisks (\*) represent particles that evolve during iterations, and the green triangle ( $\Delta$ ) represents, for each iteration, the combination resulting in the minimum  $\Delta V_{TOT}$ . The yellow square ( $\square$ ) represents the solution sought.
3. The bottom-left graph represents the minimum value of  $\Delta V_{TOT}$  achieved at the end of each iteration.

<sup>5</sup><https://youtu.be/KGaobWR8v1w>

The algorithm converges after 27 iterations. At the 27th iteration, all particles become identical, halting further progression of the algorithm. The provided solution is characterized by:

$$\begin{cases} \Delta V_1 = 2.456530 \text{ km/s} \\ \text{i-th trajectory} = 97 \\ \delta = 85.91^\circ \Rightarrow R_p = 1.7065 \times 10^7 \text{ km from Saturn} \end{cases} \quad (80)$$

The total  $\Delta V_{TOT}$  amounts to:

$$\Delta V_{TOT} = \Delta V_1 + \Delta V_2 = 2.681346 \text{ km/s} \quad (81)$$

Thus,  $\Delta V_2$  can be calculated as:

$$\Delta V_2 = \Delta V_{TOT} - \Delta V_1 = 0.224816 \text{ km/s} \quad (82)$$

It's a result we expected: the most costly maneuver is the one enabling the spacecraft to deviate from the hyperbolic arrival trajectory, while the subsequent maneuver to enter the invariant manifold trajectory is far less demanding. Both maneuvers are executed with a retrograde  $\Delta V$ : the spacecraft decelerates. Compared to the direct arrival on Titan, as described in Section 6.2, we achieved a reduction of over 70.9% in terms of  $\Delta V$ .

In Figures 49, 50, and 51, the complete trajectory of the spacecraft, optimized via PSO, is depicted.

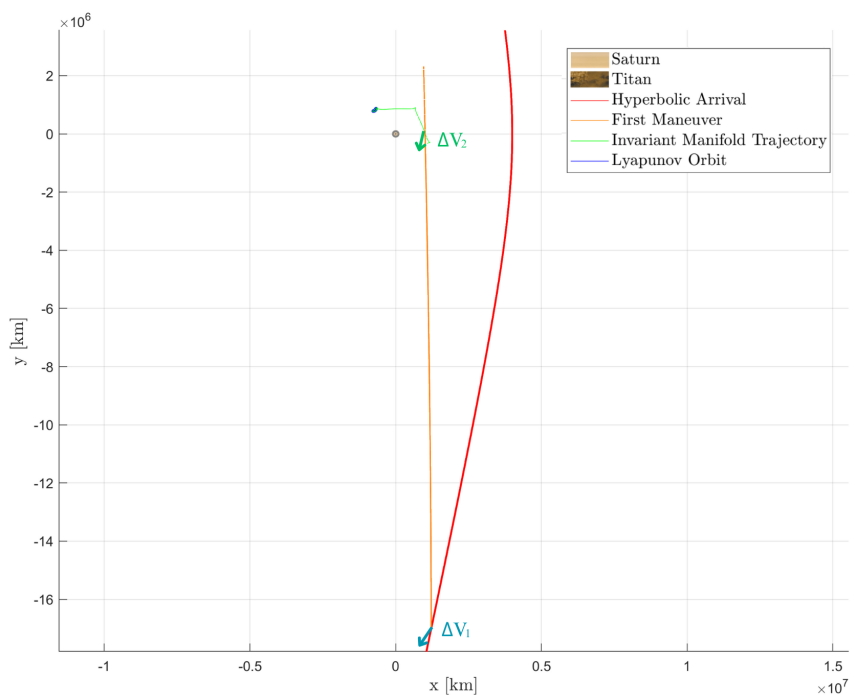


Figure 49: Spacecraft's final trajectory (PSO results)

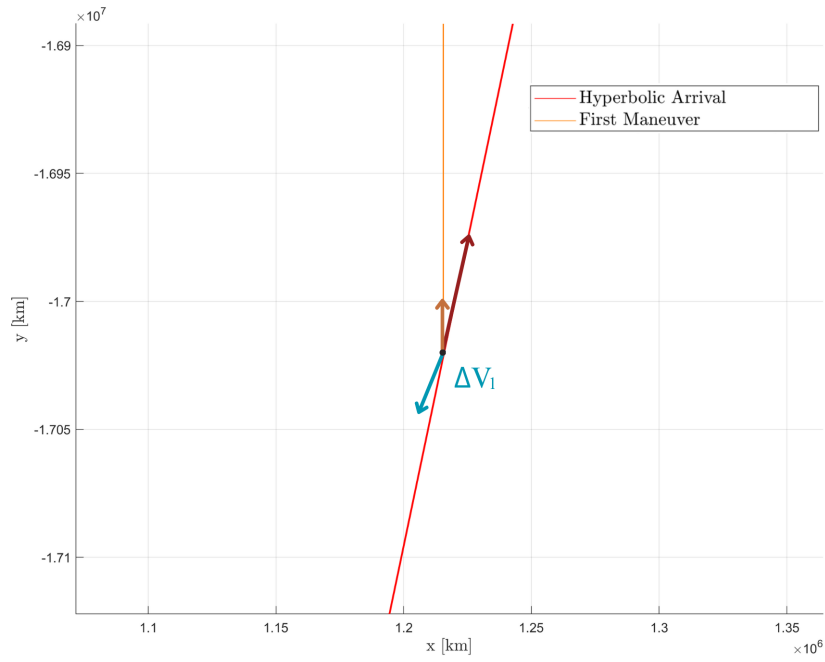


Figure 50: Spacecraft's final trajectory (PSO results). Zoom-in on the first maneuver

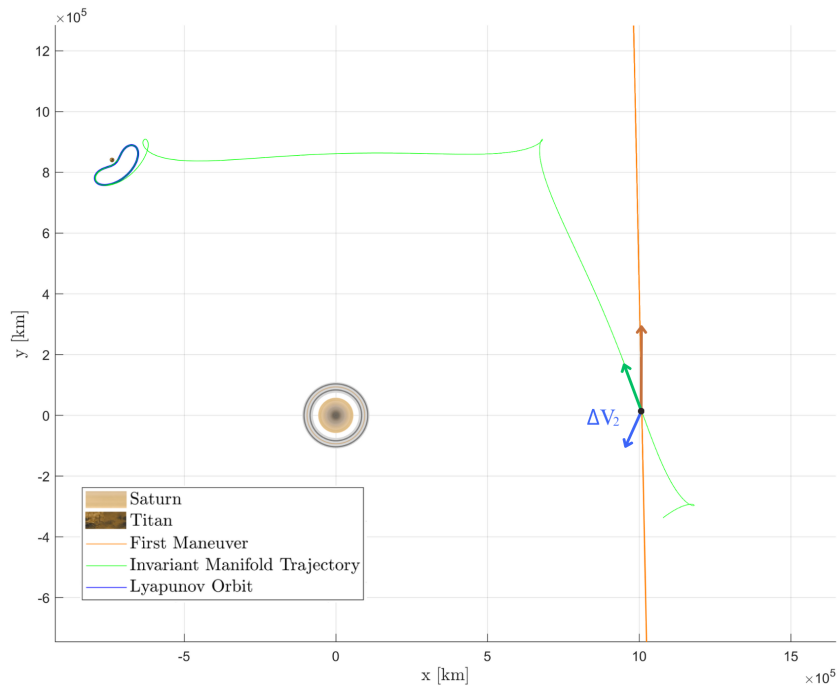


Figure 51: Spacecraft's final trajectory (PSO results). Zoom-in on the second maneuver

## 6.5 Trajectory Overview and Final Results

In this chapter, our initial focus was on assessing the  $\Delta V$  required for a direct arrival at Titan. Even though this approach wasn't executed, it served as a benchmark for comparisons, allowing us to draw conclusions regarding the optimization proposed using invariant manifolds and the application of PSO. The latter strategy, extensively discussed in the preceding section, resulted in a  $\Delta V_{TOT} = 2.681346$  km/s, marking a reduction of over 70.9% compared to the direct arrival discussed in Section 43.

The optimized trajectory originates from Saturn's SOI. Leveraging Hajdik et al.'s work [43], we considered the hyperbolic excess velocity  $v_\infty$  provided by their research along with precise dates. This enabled us to make precise considerations regarding the relative position between Saturn and Titan and implement the optimization more accurately.

This section summarizes the key findings, tracing the complete trajectory of the spacecraft from Saturn's SOI to the DRO orbit, chosen after a meticulous analysis discussed in Chapter 3.

The spacecraft's journey starts as it enters Saturn's SOI with a hyperbolic excess velocity of  $v_\infty = 5.9177$  km/s, following a hyperbolic trajectory. (See Figure 52)

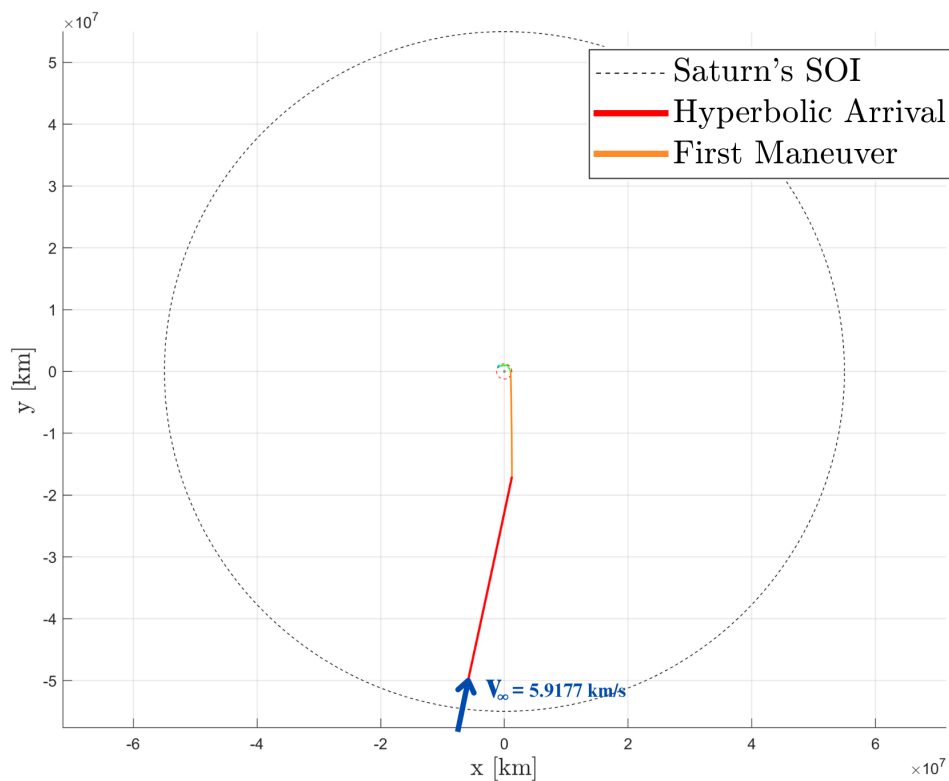


Figure 52: Final trajectory overview

At a distance of approximately  $1.7065 \times 10^7$  km from Saturn, the first critical maneuver occurs. This retrograde maneuver, characterized by a  $\Delta V_1 = 2.4565$  km/s, facilitates a deviation from the initial hyperbolic trajectory, enabling a transition to a lower-velocity one. (Refer to Figure 53)

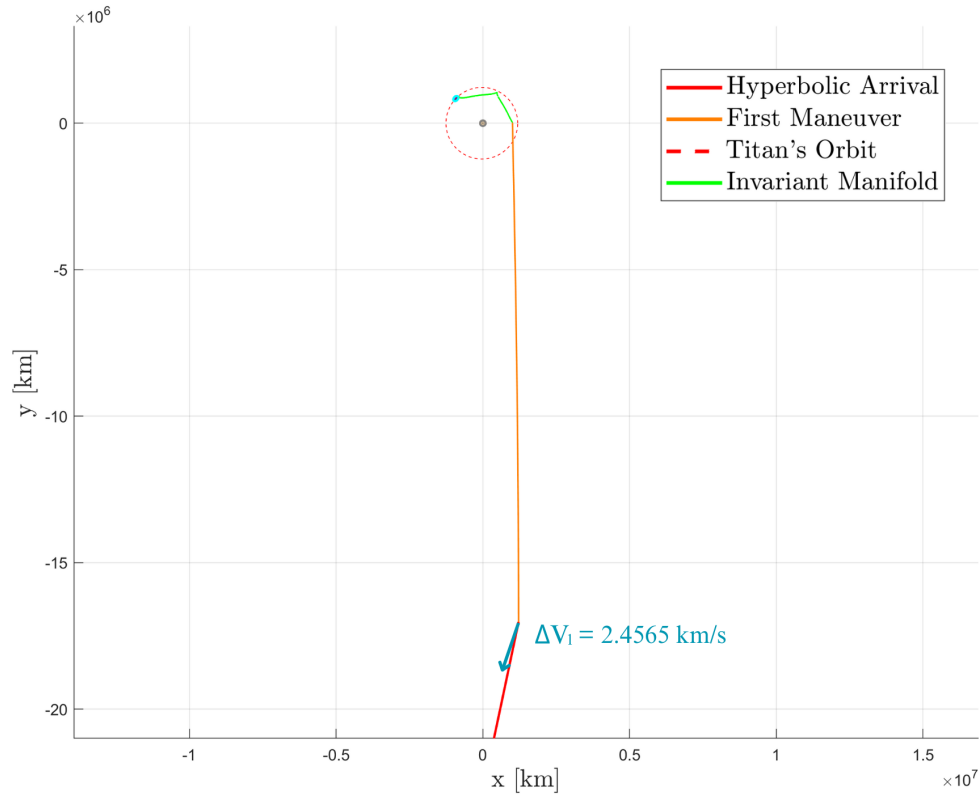


Figure 53: Final trajectory overview. First maneuver ( $\Delta V_1$ )

Continuing along this new, lower-velocity hyperbolic trajectory, the spacecraft approaches the invariant manifold, prompting the second maneuver. Characterized by a retrograde  $\Delta V_2 = 0.2248$  km/s, this maneuver optimizes the spacecraft's velocity by further slowing it down, aiding its precise alignment with the invariant manifold and ensuring a smoother intersection. (Figure 54).

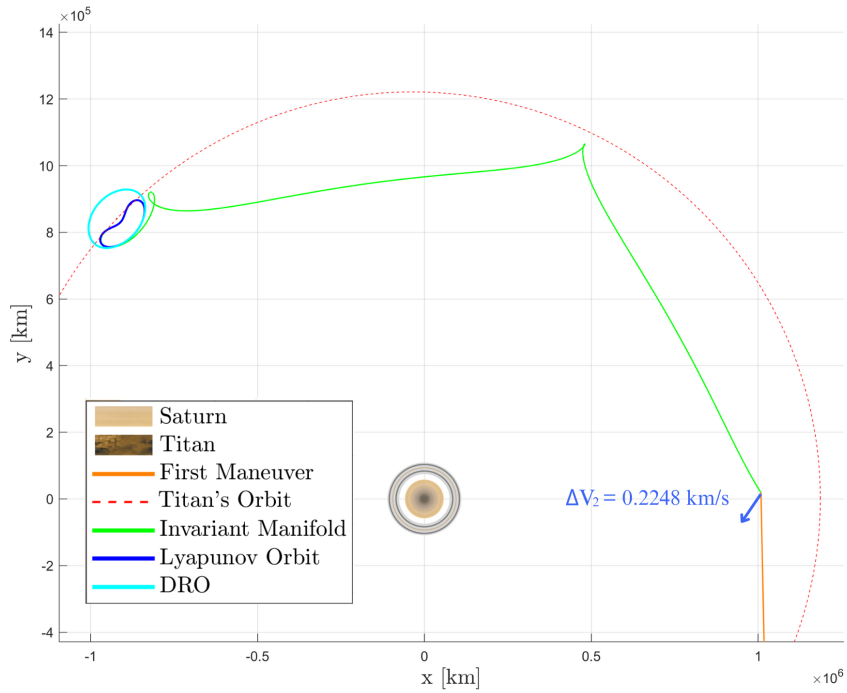


Figure 54: Final trajectory overview. Second maneuver ( $\Delta V_2$ )

The spacecraft is propelled through the invariant manifold, asymptotically reaching the Lyapunov orbit. The asymptotic approach occurs because the invariant manifold was obtained by perturbing the Lyapunov orbit along the stable eigenvector direction of the monodromy matrix (as described in Section 4.4). Hence, a negligible  $\Delta V$  adjustment on the order of a few m/s, is necessary for precise alignment within the orbit. (Figure 55)

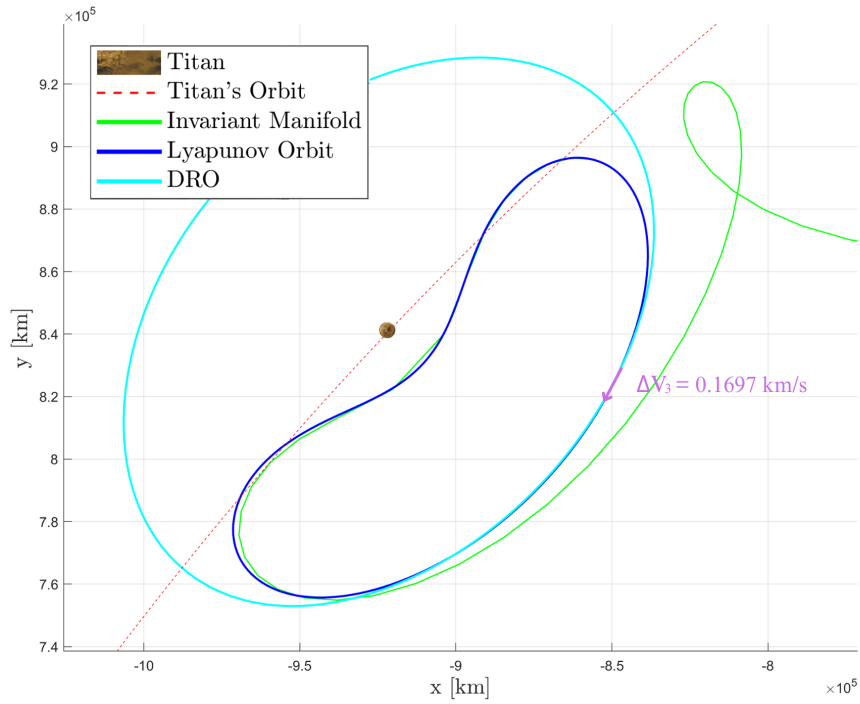


Figure 55: Final trajectory overview. Third maneuver ( $\Delta V_3$ )

Upon attaining the Lyapunov orbit, transitioning to the DRO mandates a  $\Delta V_3 = 0.1697$  km/s. In this case, the maneuver accelerates the spacecraft, facilitating its transfer to the DRO orbit, which is more stable than the Lyapunov orbit.

Ultimately, as the spacecraft enters Saturn's SOI, the cumulative  $\Delta V_{TOT}$  required is:

$$\Delta V_{TOT} = \Delta V_1 + \Delta V_2 + \Delta V_3 = 2.851 \text{ km/s} \quad (83)$$

## 7 Conclusions & Future Work

This thesis showcases the successful fusion of Dynamical Systems Theory (DST) and Particle Swarm Optimization (PSO) in optimizing spacecraft trajectories for interplanetary orbit insertion into Saturn-Titan three-body orbits. The exploration journey begins with a thorough examination of Titan's significance within the Saturnian system, highlighting its orbital characteristics and scientific relevance. Titan, with its unique atmosphere, methane lakes, and potential for prebiotic chemistry, stands as a pivotal destination, holding immense scientific value in understanding planetary evolution and the potential for extraterrestrial life. Yet, reaching Titan poses significant challenges due to its thick atmosphere, demanding innovative trajectory optimization to ensure successful orbit insertion and exploration.

Following this analysis, the study delves into the Circular Restricted Three-Body Problem (CR3BP), identifying Distant Retrograde Orbits (DROs) as optimal trajectories for conducting comprehensive observations of Titan while considering orbital stability.

The combined application of Dynamical System Theory (DST) and the Particle Swarm Optimization (PSO) algorithm emerges as pivotal in optimizing the insertion trajectory into a Distant Retrograde Orbit (DRO). The results obtained demonstrate significant promise, revealing a  $\Delta V$  requirement of 2.6813 km/s, marking a remarkable reduction of approximately 70.9% compared to a direct insertion onto Titan.

This achievement underscores the importance of advanced computational techniques in optimizing interplanetary trajectories within the Saturn-Titan system, paving the way for accurate and efficient future explorations.

Moving forward, several avenues for future research and development emerge from this thesis:

- **Refinement of optimization techniques:** Continual refinement and enhancement of optimization algorithms beyond PSO could be explored, incorporating machine learning or evolutionary algorithms such as Differential Evolution (DE) or Genetic Algorithms (GA) to either supplement or replace PSO, potentially yielding even more optimized trajectories.
- **Enhanced Mission Flexibility:** Investigating trajectories that enable increased maneuverability across various regions of Titan, notably the polar areas, while maintaining orbital stability. This may involve evaluating diverse trajectories with multiple Delta V maneuvers aimed at reducing the total Delta V requirement for the mission.
- **Real-time Trajectory Adaptation:** Develop methodologies for real-time trajectory adaptation based on evolving mission parameters or unexpected celestial events encountered during space travel. This capability became crucial in missions akin to the Cassini spacecraft's exploration of Saturn. Throughout its mission, Cassini encountered potential collisions with small moonlets within Saturn's rings [46]. These encounters necessitated immediate and unplanned trajectory adjustments to

ensure the spacecraft's safety and the mission's success. Moreover, planned scientific observations, notably around moons like Titan and Enceladus, often required on-the-fly trajectory adaptations to optimize data collection based on real-time information received during the mission. These instances underscored the critical need for adaptable trajectories, capable of accommodating both anticipated encounters and unforeseen events, thereby ensuring mission safety and maximizing scientific returns.

- **Multi-Objective Optimization:** Extend optimization strategies to consider multiple objectives, such as reducing travel time, maximizing scientific data collection, and minimizing propellant consumption simultaneously.
- **Optimization of Alternative Trajectory Selection:** Investigate the possibility of evaluating alternative Lyapunov orbits or orbits from other families that facilitate insertion into Distant Retrograde Orbits (DROs), potentially improving efficiency or accommodating specific mission requirements while ensuring stable and efficient trajectories.

In conclusion, the successful fusion of advanced computational techniques with Dynamical Systems Theory in optimizing interplanetary trajectories for Saturn-Titan missions sets the stage for continued innovation and refinement in space exploration, promising more efficient and accurate mission planning in the future.

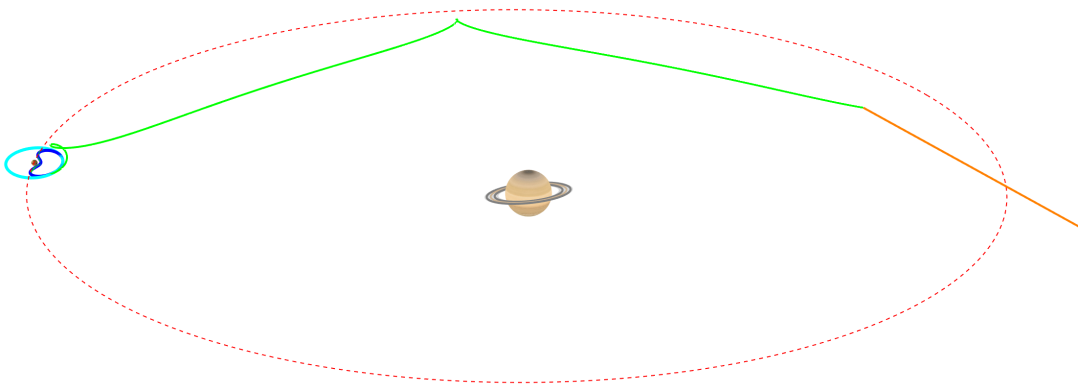


Figure 56: Optimized trajectory to Titan



## References

- [1] NASA/JPL-Caltech/Space Science Institute. *A Last Look at Titan*. <https://solarsystem.nasa.gov/resources/17787/a-last-look-at-titan/>. Accessed: May 9, 2023. 2019.
- [2] NASA/JPL. *In Depth - Titan*. <https://solarsystem.nasa.gov/moons/saturn-moons/titan/in-depth/>. Accessed: May 9, 2023. 2021.
- [3] R.H. Brown, JP. Lebreton, and J.H. Waite. *Titan from Cassini-Huygens*. Springer, 2009. ISBN: 978-1402092145.
- [4] NASA/JPL-Caltech. *Cassini - Mission Overview*. <https://saturn.jpl.nasa.gov/mission/flybys/titan20100621/>. Accessed: May 12, 2023. 2021.
- [5] C.P. McKay, J.B. Pollack, and R. Courtin. “The Greenhouse and Antigrreenhouse Effects on Titan”. In: 253.5024 (1991), pp. 1118–1121. DOI: 10.1126/science.11538492.
- [6] Baldwin E. (ESA). *The Mysterious ‘Lakes’ on Saturn’s Moon Titan*. <https://solarsystem.nasa.gov/missions/cassini/mission/spacecraft/huygens-probe/>. Accessed: May 16, 2023. 2015.
- [7] Griffith C.A. “Possible tropical lakes on Titan from observations of dark terrain”. In: *Nature* 486.7402 (2012), pp. 237–239. DOI: 10.1038/nature11165.
- [8] NASA/JPL-Caltech/ASU. *First Global Geologic Map of Titan*. [www.jpl.nasa.gov/images/pia23174-first-global-geologic-map-of-titan](http://www.jpl.nasa.gov/images/pia23174-first-global-geologic-map-of-titan). Accessed: May 12, 2023. 2019.
- [9] NASA. *First Global Geologic Map of Titan*. [www.nasa.gov/centers/ames/missions/archive/pioneer.html](http://www.nasa.gov/centers/ames/missions/archive/pioneer.html). Accessed: May 13, 2023. 2007.
- [10] NASA. *In Depth - Voyager 1*. <https://solarsystem.nasa.gov/missions/voyager-1/in-depth/>. Accessed: May 14, 2023. 2021.
- [11] NASA. *Titan - Voyager 2*. [https://nssdc.gsfc.nasa.gov/imgcat/html/object\\_page/vg2\\_p23929.html](https://nssdc.gsfc.nasa.gov/imgcat/html/object_page/vg2_p23929.html). Accessed: May 14, 2023. 2015.
- [12] C. Martinez and D. Brown. *Cassini Spacecraft Images Seas on Saturn’s Moon Titan*. NASA/JPL. <https://solarsystem.nasa.gov/news/12381/cassini-spacecraft-images-seas-on-saturns-moon-titan/>. Accessed: May 16, 2023. 2007.
- [13] NASA/JPL-Caltech/ASI. *PIA08630: Lakes on Titan*. <https://photojournal.jpl.nasa.gov/catalog/PIA08630>. Accessed: May 14, 2023. 2006.
- [14] ESA/NASA/JPL/University of Arizona. *Spacecraft - Huygens Probe*. <https://solarsystem.nasa.gov/missions/cassini/mission/spacecraft/huygens-probe/>. Accessed: May 16, 2023. 2022.
- [15] ESA/NASA/JPL/University of Arizona. *Descent to Titan*. [https://www.esa.int/ESA\\_Multimedia/Images/2017/09/Descent\\_to\\_Titan](https://www.esa.int/ESA_Multimedia/Images/2017/09/Descent_to_Titan). Accessed: May 16, 2023. 2017.

- [16] National Academies of Sciences Engineering and Medicine. *Origins, Worlds, and Life: A Decadal Strategy for Planetary Science and Astrobiology 2023-2032*. 2022. ISBN: 9780309475785.
- [17] NASA/JHU-APL. *NASA's Dragonfly Will Fly Around Titan Looking for Origins, Signs of Life*. <https://www.nasa.gov/press-release/nasas-dragonfly-will-fly-around-titan-looking-for-origins-signs-of-life/>. Accessed: May 17, 2023. 2019.
- [18] M. Talevi and D. Brown. *NASA and ESA prioritize outer planet missions*. <https://sci.esa.int/web/cosmic-vision/-/44249-nasa-and-esa-prioritize-outer-planet-missions>. Accessed: May 18, 2023. 2009.
- [19] Stofan E. "Titan Mare Explorer (TiME): First Exploration of an Extraterrestrial Sea". In: URL: [https://www.nasa.gov/pdf/580675main\\_02\\_Ellen\\_Stofan\\_TiME\\_.pdf](https://www.nasa.gov/pdf/580675main_02_Ellen_Stofan_TiME_.pdf).
- [20] J. W. Barnes, L. Lemke, R. Foch, C. P. McKay, R. A. Beyer, J. Radebaugh, D. H. Atkinson, R. D. Lorenz, Stéphane Le Mouélic, Sebastien Rodriguez, Jay Gundlach, Francesco Giannini, Sean Bain, F. Michael Flasar, Terry Hurford, Carrie M. Anderson, Jon Merrison, Máté Ádámkóvics, Simon A. Kattenhorn, Jonathan Mitchell, Devon M. Burr, Anthony Colaprete, Emily Schaller, A. James Friedson, Kenneth S. Edgett, Angioletta Coradini, Alberto Adriani, Kunio M. Sayanagi, Michael J. Malaska, David Morabito, and Kim Reh. "AVIATR—Aerial Vehicle for In-situ and Airborne Titan Reconnaissance. A Titan airplane mission concept". In: *Experimental Astronomy* 33.1 (Mar. 2012), pp. 55–127. DOI: 10.1007/s10686-011-9275-9.
- [21] I. Urdampilleta and O. Prieto-Ballesteros. "TALISE: Titan Lake In-situ Sampling Propelled Explorer". In: *European Planetary Science Congress (2012)*. DOI: 10.1007/s10686-011-9275-9.
- [22] Jacobi C.G. "Sur le mouvement d'un point et sur un cas particulier du problème des trois corps". In: *Comptes Rendus de l'Académie des Sciences de Paris* 3 (1836), pp. 59–61.
- [23] Poincaré H. "Les Méthodes Nouvelles de la Mécanique Céleste". In: (1892).
- [24] Vallado D.A. *Fundamentals of Astrodynamics and Applications*. 2007. ISBN: 978-1-881883-14-2.
- [25] Grebow D.J. "Generating periodic orbits in the circular restricted three-body problem with applications to lunar south pole coverage". In: *Purdue University* (2006).
- [26] Farquhar R.W. *The control and use of libration point satellites*. California: Stanford University, 1968.
- [27] R. Whitley and R. Martinez. "Options for staging orbits in cislunar space". In: Mar. 2016, pp. 1–9. DOI: 10.1109/AERO.2016.7500635.
- [28] V. Baraldi and D. Conte. "Trajectory Optimization and Control Applied to Landing Maneuvers on Phobos from Mars-Phobos Distant Retrograde Orbits". In: *Universe* (2023). DOI: 10.3390/universe9080348.

- [29] J. Roa and C.J. Handmer. “Quantifying hazards: asteroid disruption in lunar distant retrograde orbits”. In: *arXiv Prepr. arXiv* 1505 (May 2015). DOI: 10.48550/arXiv.1505.03800.
- [30] D. Conte and B.D. Spencer. “Mission analysis for Earth to Mars-Phobos distant retrograde orbits”. In: *Acta Astronautica* 151 (2018), pp. 761–771. DOI: 10.1016/j.actaastro.2018.06.049.
- [31] NASA. *Three-Body Periodic Orbits*. [https://ssd.jpl.nasa.gov/tools/periodic\\_orbits.html](https://ssd.jpl.nasa.gov/tools/periodic_orbits.html). Accessed: Oct 6th, 2023.
- [32] M. Paluszczek, A. Price, Z. Koniaris, C. Galea, S. Thomas, S. Cohen, and R. Stutz. “Nuclear fusion powered Titan aircraft”. In: *Acta Astronautica* 210 (Apr. 2023). DOI: 10.1016/j.actaastro.2023.04.029.
- [33] C. Martinez and R. Prucey. *Titan’s Volcanoes Give NASA Spacecraft Chilly Reception*. [https://www.nasa.gov/mission\\_pages/cassini/media/cassini-20081215b.html](https://www.nasa.gov/mission_pages/cassini/media/cassini-20081215b.html). Accessed: May 20, 2023. 2008.
- [34] K.C. Howell, B.T. Barden, and M.W. Lo. “Application of Dynamical Systems Theory to Trajectory Design for a Libration Point Mission”. In: *Journal of the Astronautical Sciences* 45.2 (June 1997), pp. 161–178. DOI: 10.1007/BF03546374.
- [35] D. S. Burnett, B. L. Barraclough, R. Bennett, M. Neugebauer, L. P. Oldham, C. N. Sasaki, D. Sevilla, N. Smith, E. Stansbery, D. Sweetnam, and R. C. Wiens. “The Genesis Discovery Mission: Return of Solar Matter to Earth”. In: *Space Science Reviews* 105.3 (Jan. 2003), pp. 509–534. DOI: 10.1023/A:1024425810605.
- [36] A. Johns, B. Seaton, J. Gal-Edd, R. Jones, C. Fatig, and F. Wasiak. “James Webb Space Telescope: L2 communications for science data processing”. In: *Observatory Operations: Strategies, Processes, and Systems II*. Ed. by Roger J. Brissenden and David R. Silva. Vol. 7016. Society of Photo-Optical Instrumentation Engineers (SPIE) Conference Series. July 2008, 70161D, p. 70161D. DOI: 10.1117/12.777377.
- [37] W.S. Koon, M. Lo, J.E. Marsden, and S. Ross. *Dynamical Systems, the Three-Body Problem, and Space Mission Design*. Oct. 2022. ISBN: 978-0-615-24095-4.
- [38] D.B. Spencer and D. Conte. *Interplanetary Astrodynamics*. 2023. ISBN: 978-0-367-75970-4.
- [39] M. Pontani and B.A. Conway. “Particle Swarm Optimization Applied to Space Trajectories”. In: *Journal of Guidance Control Dynamics* 33.5 (Sept. 2010), pp. 1429–1441. DOI: 10.2514/1.48475.
- [40] G.H. Lin, J. Zhang, and L. Zhao-Hua. “Hybrid Particle Swarm Optimization with Differential Evolution for Numerical and Engineering Optimization”. In: *International Journal of Automation and Computing, Vol. 15, No. 1, pp. 103-114* (2018). DOI: 10.1007/s11633-016-0990-6.
- [41] M.R. Sentinella and L. Casalino. “Cooperative evolutionary algorithm for space trajectory optimization”. In: *Celestial Mechanics and Dynamical Astronomy* 105.1-3 (Nov. 2009), pp. 211–227. DOI: 10.1007/s10569-009-9223-4.

- [42] K. Zhu, F. Jiang, J. Li, and H. Baoyin. “Trajectory Optimization of Multi-Asteroids Exploration with Low Thrust”. In: *Japan Society of Aeronautical Space Sciences Transactions* 52.175 (Jan. 2009), pp. 47–54. DOI: 10.2322/tjsass.52.47.
- [43] H. Hajdik, S. Ramsey, and R.A. Wright. “Titan Aerogravity Assist for Saturn Orbital Insertion and Study of Enceladus”. In: Chancellor’s Honors Program Projects (May 2020).
- [44] Gajeri M. “Trajectory design for a Titan mission using the Direct Fusion Drive”. In: July 2020.
- [45] M. McQuaide, D. Ellison, J. Englander, M. Jesick, M. Ozimek, and D. Roth. “Dragonfly Phase B Mission Design”. In: Aug. 2023.
- [46] NASA. *Cassini Finds Saturn’s Rings Coat Tiny Moons*. <https://science.nasa.gov/missions/cassini/cassini-finds-saturns-rings-coat-tiny-moons/>. Accessed: November 12th, 2023.